# Páramos under stress: A multidisciplinary approach to mitigate future hazards

# Páramos under stress: A multidisciplinary approach to mitigate future hazards

by

| | **ID / Affiliation** |
|---|---|
| **Students** | |
| Loes Vogelaar | 5016649 |
| Elke van Thiel | 5168945 |
| Jelle Gortemaker | 5115051 |
| Mathias Ruhe | 5400880 |
| Fleur Heeremans | 4718186 |
| Arend-Jan Timmermans | 4776305 |
| **Supervisors** | |
| Dr. K.B.J. Dunne | TU Delft |
| Dr. S. Toby | TU Delft |
| Dr. Miguel Cabrera | TU Delft |
| Prof.dr.ir. L.C. Rietveld | TU Delft |
| Dr. M. Córdova Mora | UCuenca |
| Dr. J. Pésantez | UCuenca |

**Project duration**
September 1, 2025 – November 7, 2025

# Preface

Multidisciplinary approaches in environmental research offer a way to build a shared, more complete problem definition, link it to the mechanisms that drive change, and point to actionable solutions (Schoot Uiterkamp and Vlek, 2007). Where a traditional disciplinary approach may lead to a hard focus on one component of the problem a multidisciplinary team combines knowledge and different scientific approaches (concepts, methods, models and findings) in the hope to create a more coherent picture.

This report, titled *Páramos under stress: A multidisciplinary approach to mitigate future hazards*, integrates hydrology, geoscience, remote sensing, environmental water quality, and social science to characterise risk in the South-Ecuadorian Páramo. We combine in-situ observations from the Zhurucay and Quinuas ecohydrological observatories with satellite products, trend analysis, landslide modelling, water-quality assessment, and stakeholder analysis to examine how changing climate drivers and mining plans may affect water resources, slope stability, and communities in Azuay. Our goal is to identify multi-year meteorological, hydrological, and social trends in the Páramo system and to clarify their implications for society. We hope this synthesis helps guide future research, and supports policymakers in anticipating hazards, weighing trade-offs, and prioritising mitigation that keeps Páramo ecosystems—and the people who depend on them—resilient.

We are grateful to our supervisors from UCuenca and TU Delft for data access and guidance, and are especially grateful to Dr. M. Córdova Mora and Dr. J. Pésantez for hosting us on their campus for 2 months.

# Contents

# 1

# Introduction

In March 2022, heavy rainfall triggered devastating landslides in the Azuay Province near Cuenca, resulting in the loss of four lives and the destruction of homes (Tapia, 2022; Davies, 2022). The main road between Cuenca and Guayaquil, two of the largest and most important cities from Ecuador, was blocked off for weeks. Such extreme weather events and its consequences such as landslides have become more frequent, raising concerns about the resilience of the páramo ecosystems.

Further complicating these environmental challenges is the proposed Loma Larga gold mining project by Canada's Dundee Precious Metals mining company. Located near the Quimsacocha water reserve, the project has faced significant opposition from local communities and environmental groups. Even though this project has for now been stalled, in the future it might be decided to continue exploitation of the area (Hidayat, 2025). A 2024 technical report by Cuenca's public water utility, ETAPA, highlighted potential risks of mine waste and water contamination, emphasizing the importance of protecting the páramo ecosystems that supply water to tons of people and are crucial for irrigation water purposes (The Guardian, 2025).

These developments underscore the urgent need to address the complicated and multifaceted challenges facing the Páramo ecosystems. Much of the existing research tends to focus on isolated issues, such as changing weather patterns, water quality, or land use, rather than adopting a multidisciplinary approach that integrates these factors. This knowledge gap limits our ability to fully understand and address the complex interactions within the Páramo. Multidisciplinary approaches in environmental research enable a more comprehensive understanding of such complex problems by combining diverse scientific perspectives and methods (e.g. Schoot Uiterkamp and Vlek, 2007; Mosquera et al., 2023).

This report aims to investigate the changing meteorological and hydrological patterns in the Páramo and assess their potential impacts on local communities. By integrating data analysis, hydrology, subsurface studies, water quality, and social impact, the report explores multi-year trends and variability in the Páramo system and their societal effects.

## 1.1. Research area

### 1.1.1. The Páramo system

The Páramo ecosystem is a cold and humid tropical ecosystem located between the tree line and the permanent snow region (Hofstede et al., 2014). Countries in which this unique system can be found include Perú, Ecuador, Colombia, Venezuela, Costa Rica and Panama. The ecosystem is characterised by its humid environment with continuous moisture in the form of rain, clouds, and fog, caused by orographic uplift due to the Andes mountain range. As a result, yearly precipitation often reaches over 2000 mm with ranges of 500 - 3000 mm (Renvoize et al., 2000). The temperature lies between freezing and 30 degrees caused by diurnal fluctuations. Due to its high elevation frost, snow and ice are a common occurrence in this region and changes in weather may be abrupt (Renvoize et al., 2000, Hofstede et al., 2014). (**Paramo_rainfall)**) found that only approximately 12% of the days are dry.

Moreover, they concluded that when taking into account mist, the total amount of precipitation was ~ 15% higher. This shows that precipitation in the form of mist is a crucial factor to the water supply.

The páramo contains a unique collection of flora and fauna. It counts over 4,000 different plants - of which 60% is endemic (Ropero, 2020) - which is the highest number among all alpine landscapes worldwide (Madrinán et al., 2013). The flora is dominated by grasses, small shrubs and the iconic rosette plants which are unique to these ecosystems (Fiallos et al., 2015). In the following research, these landscapes are characterised as "Tussock Grasses" or "Grassland" (see Figure 1.2). More information regarding Land Cover (LC) classification can be found in Figure 1.2 and Chapter 2. For fauna, there is no exact figure of the amount of species. However, there are more than 460 species, of which many are also considered endemic.

Besides being a unique and lush ecosystem, the Páramo is widely recognised to be a fundamental water source for surrounding population and major cities like Lima: it provides high quality fresh water, lands that can be used for cultivation of crops and cattle, and it represents and important part in indigenous culture (Hofstede et al., 2014; García et al., 2020). Some sources claim that the Páramo, while only covering 2% of Ecuador's land, supply up to 80% of the land's drinking water (Adventures, 2025).

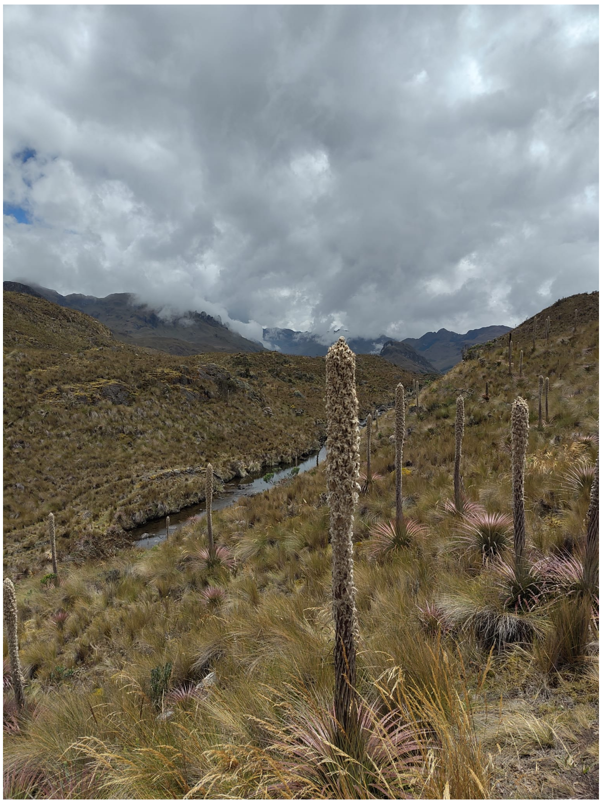

Figure 1.1: Picture of the Quinuas Páramo, with typical endemic rosette plants. Picture is authors owned.

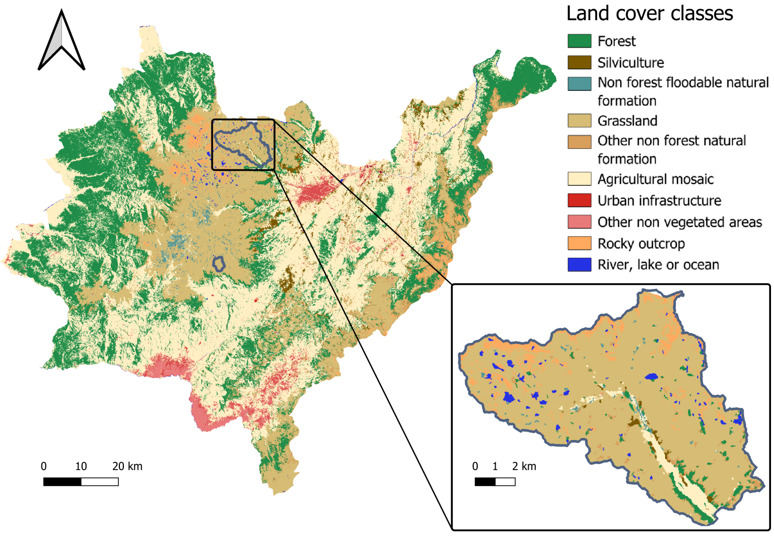

Figure 1.2: Land cover classification map of the Azuay province and Quinuas observatory.

### 1.1.2. Geological description

In Ecuador, the Andes, which transverses the full length of the country and the Azuay province, are divided into two ranges, the Cordillera Occidental (Western Chain) and the Cordillera Oriental (Eastern Chain), with a central valley running between them (Carrión-Mero et al., 2022). The Northern and central part of the Andes are additionally characterised by a number of active volcanoes, most of them located around the capital Quito and the city of Ambato. Towards the south, where our research area is located, less volcanic activity is present. Nevertheless, there is plenty of evidence for volcanic activity as most rocks in the region are of volcanic origin, depicted in Figure 1.3. The top of the Western and Eastern Andes chain in this region are covered with our ecosystem of interest: the Páramo.

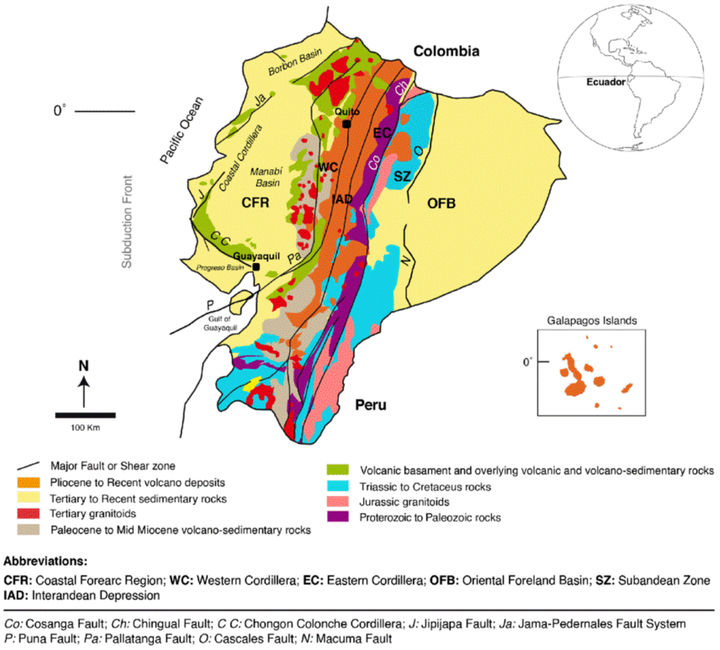

Figure 1.3: Geological map of Ecuador with a classification of the rocks at the surface. The orange, green and beige colour reveal the locations of (possible) volcanic rocks. (Carrión-Mero et al., 2022

Zooming in to the Quinuas catchment, which is located within the Cajas National Park, the dominant formations are Unidad Chulo, Unidad Tomebamba and Formacion Chanlud, combined with intrusions of Rhyolite and Diorite, as can be seen in figure 1.4. Unidad Chulo is dated to the late Eocene (Verdezoto Villacis, 2006) and is composed of rhyolitic to dacitic tuffs, breccias and lacustrine sediments (Navarrete et al., 2022). Unidad Tomebamba originates from the early Oligocene and contains large andesitic and basic dacitic tuffs with lapilli (Navarrete et al., 2022). Finally, the Tomebamba unit is followed by Formacion Chanlud, also during the early Oligocene. This formation is composed of andesitic lavas with breccias and intercalations of volcanic sediments (Navarrete et al., 2022).

### 1.1.3. Measurement stations

The Zhurucay Ecohydrological Observatory and Quinuas Ecohydrological Observatory, established by the University of Cuenca, provide a unique data registry (see figure 1.5). A total of three ecohydrological observation stations are located in the Quinuas basin: The Toreadora, Virgen and Chirimachay ecohydrological observatories. In the Zhurucay basin one ecohydrological observatory is located, bearing the same name as the basin. Moreover, there are 10 specific locations within this basin where discharge data is gathered. Besides the observatories in the basin mentioned, there are two more meteorological stations: one located at the Balzay campus, and the other one located within the Quinuas basin called OPNC, where it only measures rainfall.

Over the past decade, these observation stations have accumulated extensive datasets on hydrological processes, hydro-geochemistry, micro-meteorology, and soil-water interactions. These records form a valuable basis for analysing correlations between climate and hydrology and for understanding

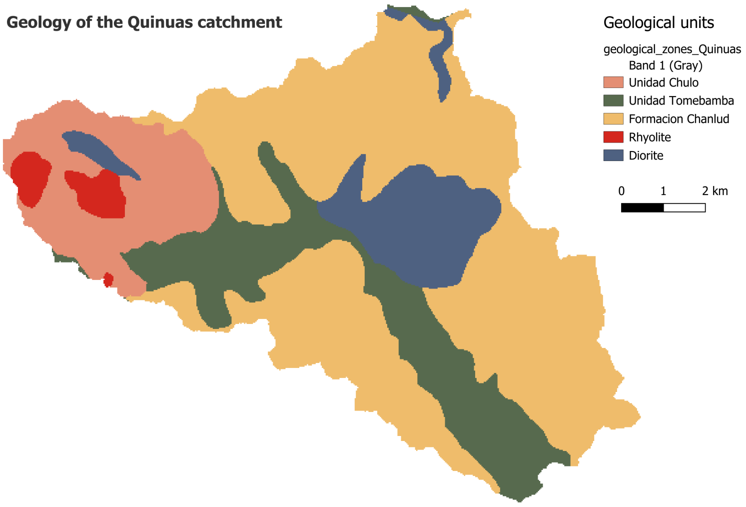

Figure 1.4: Geological map of the Quinuas catchment, after data from (Dunkley and Gaibor, 1997)

how these catchments respond to changes in weather patterns.

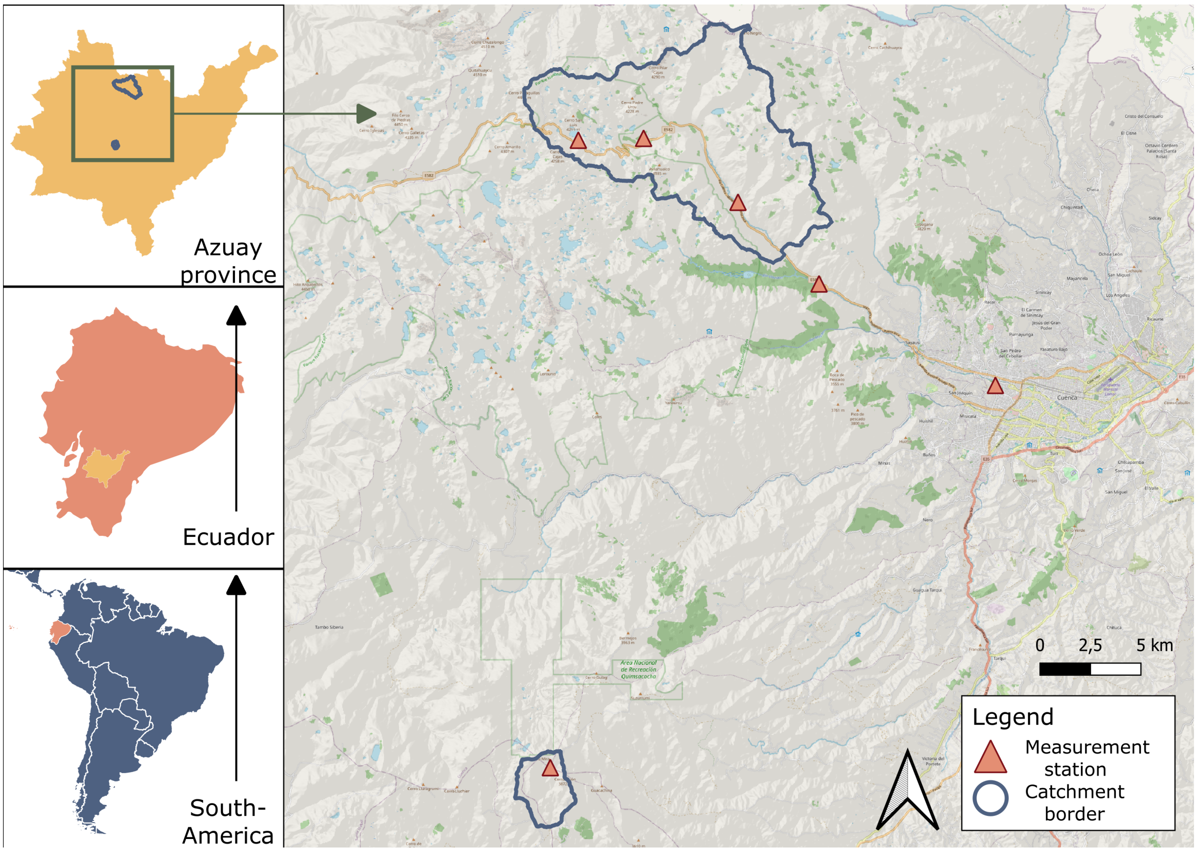

Figure 1.5: Location overview of Quinuas and Zhurucay observatories and their measurement stations.

### 1.1.4. Recent changes: Lomo Larga project

In recent years, the Cuenca region has witnessed significant changes in response to the planned development of the Loma Larga underground mine. Located approximately 30 km southwest of Cuenca, the mine covers an area of nearly 7,960 hectares in the Azuay province (see 1.6). Owned by Dundee Precious Metals, the project aims to extract gold, silver and copper, and is expected to operate for 12 years (Frost et al., 2021). The project is expected to bring major economic benefits, with hundreds of millions of dollars in revenue for the Ecuadorian government and the creation of around 1,200 jobs. However, at the same time, the project poses serious environmental and social challenges (The Guardian, 2025).

The mine is situated next to the Quimsacocha reserve in the high-altitude Páramo ecosystem. The Quimsacocha wetlands are part of the Macizo del Cajas Biosphere Reserve and supply drinking and irrigation water to hundreds of thousands of people (Barros et al., 2024). Studies have shown that these ecosystems are ecologically fragile; even minor alterations to water chemistry or soil structure can disrupt the distinctive microalgal and fungal biodiversity that maintains water quality and nutrient cycling (Delgado-Fernández et al., 2025, 2024). ETAPA, Cuenca's municipal water company, has repeatedly warned that mining could reduce water availability and contaminate the Quimsacocha watershed with heavy metals and acidic drainage. This watershed supplies drinking and irrigation water to hundreds of thousands of people (Barros et al., 2024).

In October 2025, the Ecuadorian government revoked the environmental permit for the Loma Larga project following widespread protests and criticism of Dundee Precious Metals' environmental report. The report had failed to consider the broader environmental effects beyond the immediate mining area (Schertow, 2025; Valencia, 2025). Barros, the lead author of the ETAPA study, emphasized that contamination would not be contained within the boundaries of the mine, explaining that pollutants could reach rivers further downstream (Barros et al., 2024; The Guardian, 2025).

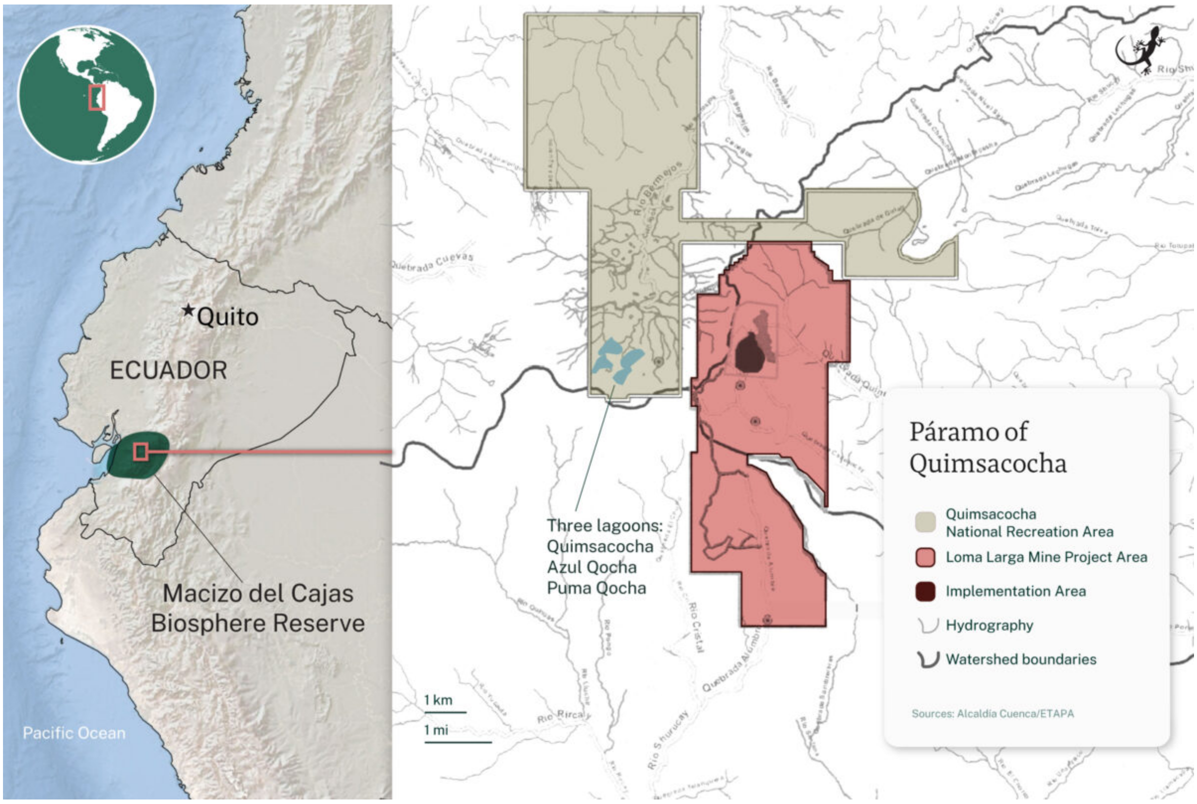

Figure 1.6: Map of the mining- and Quimsacocha area (Abulu et al., 2025)

This conflict reflects a broader national debate over the future of extractive industries in Ecuador. Indigenous and rural communities across the Andes have expressed resistance to large-scale mining, citing threats to sacred landscapes and water security (Abulu et al., 2025; Morin, 2025). These tensions highlight the current challenges facing the region, including potential water contamination, loss of biodiversity, and social division between pro- and anti-mining groups.

Although the permit has been revoked, it could be reinstated if the company revises its environmental impact assessment to address broader ecological effects. This ongoing uncertainty highlights the urgent need to study not only the environmental risks, but also the complex network of stakeholders involved, in order to better understand how decisions about the mine affect both the ecosystem and the local communities that depend on it.

## 1.2. Hazard identification

2024 saw an unprecedented increase in global temperature. It was the first year to have an average temperature 1.5 degrees higher than the pre-industrial level (Copernicus Climate Change Service, 2025). As a developing nation, Ecuador is socially and economically more vulnerable to natural hazards, in particular floods, landslides, and extreme weather events (ThinkHazard!, 2025). According to a report from the United Nations Office for Disaster Risk Reduction (UNDRR), a person is six times more likely to die in a developing country compared to a developed country from natural disasters (Disaster.Shiksha, 2025).

In this retrospect, the Andean Páramo ecosystems surrounding the city of Cuenca in Ecuador are particularly vulnerable. Currently, Cuenca has some of the highest quality in drinking water in Ecuador (Larriva Vásquez, 2023). The Páramo both regulates and filters the water that ends up in the rivers running through Cuenca. Moreover does the Páramo act as a water buffer during dry periods, providing a constant flow of fresh water (Farfán Durán, 2016). However, these high-altitude grassland ecosystems are increasingly affected by climate change, land use pressures, and degradation (Beltrán, 2018).

These altered dynamics significantly affect the hydrological chain and could threaten for example the stability of freshwater supply.

The water balance is a fundamental equation that describes the flow of water through a region of interest based on the principle of mass conversation (Wikipedia contributors, 2023). Figure 1.7 contains a very simple, basal version of the water balance. More detailed models of the water balance exist as well, but are based on the same principles. Building on equation 1.1, where a balance between precipitation $P$, runoff $Q$, evapotranspiration $ET$ and storage $\Delta S$ is depicted, it can be understood how changing weather patterns can significantly affect parameters in the water balance. Increased evaporation $ET$ due to higher temperatures, decreased precipitation $P$, or decreased storage in the form of soil moisture may therefore lead to significant changes in water runoff.

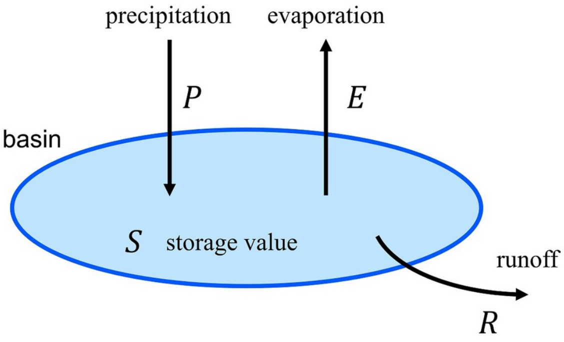

Figure 1.7: Simple water balance model. Derived from (Wikipedia contributors, 2023).

$$P = Q + ET + \Delta S \tag{1.1}$$

To gain insight into how exactly these alterations affect the Páramo, a thorough analysis of hydrometeorological patterns over time is required. Other hazards can be identified as well. For example, changes in precipitation are one of the three main causes of landslides (Highland and Bobrowsky, 2008). By analysing patterns and using soil conditions and slope, estimations can be made regarding the risk of slope failure. Furthermore, changes in hydrological trends and mining in the Páramo can result in different run-offs and sediments in the water, thereby changing its quality. This change in water quality can have devastating effects on urban areas that are dependent on this source of water. Among deterioration of water quality, mining activities can create socio-economic tensions in the form of conflicts between local communities, government institutions and mining companies over land use and water rights (Abulu et al., 2025; Morin, 2025).

## 1.3. Research aim and questions

This report aims to integrate time-series analysis of meteorological and hydrological data with landslide prediction and water quality assessment to provide an integrated understanding of future hazards in the Ecuadorian Andes near Cuenca. The potential social hazards associated with the introduction of the Lomo Larga mine are also included in this assessment. The guiding research question is:

*What are the effects of meteo/hydrological trends and mining projects in the south Ecuadorian Páramo system with respect to water quality, slope stability and local stakeholders?*

In order to answer this main research question, the following subquestions are formulated:

- Can satellite data be used in the Páramo to create reliable models that predict parameters from the water balance?
- Do temperature, precipitation and soil moisture data, collected in the catchment basins, show any sign of a multi-year trend and can we develop a model that is able to accurately forecast at least one year into the future?
- What are the slope stability scenarios in the Páramo region of Cuenca, considering long-term hydrological trends?

- What further research and information would be needed for increasing the accuracy of a landslide hazard assessment system in the Azuay province?
- What are the regional water-related environmental impacts of the Loma Larga mine on surface and groundwater quality and water availability?
- How will the Cuenca water supply system be influenced by the Loma Larga mine?
- How do differences in power, interest and commitment among involved stakeholders explain the main conflicts surrounding the Loma Larga mining project in Azuay?

The research is built up conform the structure presented in Figure 1.8.

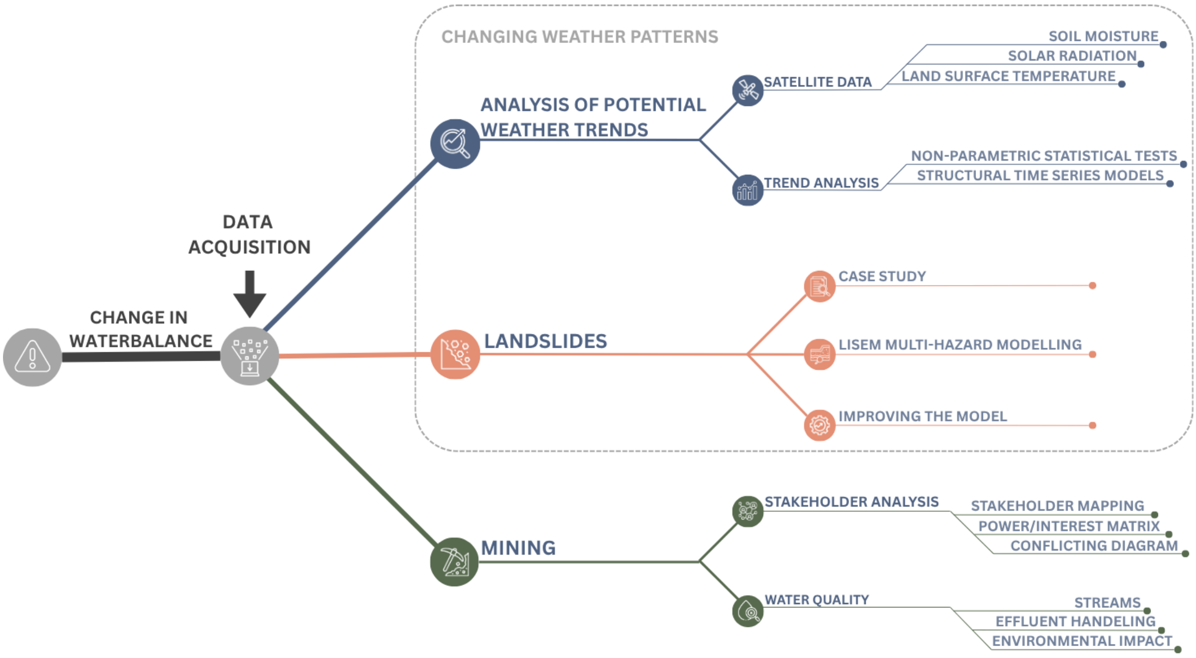

Figure 1.8: Structure of the multidisciplinary research(Author’s work, 2025)

# 2

# Data acquisition

In this Chapter, the different sources of data and data extraction methods are described.

## 2.1. Measurement stations

In Chapter 1, the locations and characteristics of the measurements are described. Table 2.1 contains the exact variables which are used in this report. The start and end date and frequency are given to give an overview of the data availability per variable. It should be noted that the OPNC measurement station only captures precipitation data.

| **Variables used** | **Parameter** | **Zhurucay** | **Toreadora** | **Virgen** | **Chirimachay** | **OPNC** | **Balzay** |
|---|---|---|---|---|---|---|---|
| **Air temperature** | Sample frequency | *5 min* | *5 min* | *5 min* | *5 min* | - | *5 min* |
| | Record start | *Dec-2010* | *Dec-2010* | *Dec-2010* | *Dec-2010* | - | *Dec-2010* |
| | End of record | *Ongoing* | *Ongoing* | *Ongoing* | *Ongoing* | - | *Ongoing* |
| **Precipitation** | Sample frequency | *5 min* | *5 min* | *5 min* | *5 min* | *5 min* | *5 min* |
| | Record start | *Dec-2010* | *Dec-2010* | *Dec-2010* | *Dec-2010* | *Dec-2010* | *Dec-2010* |
| | End of record | *Ongoing* | *Ongoing* | *Ongoing* | *Ongoing* | *Ongoing* | *Ongoing* |
| **Wind speed** | Sample frequency | *5 min* | *5 min* | *5 min* | *5 min* | - | *5 min* |
| | Record start | *Dec-2010* | *Dec-2010* | *Dec-2010* | *Dec-2010* | - | *Dec-2010* |
| | End of record | *Ongoing* | *Ongoing* | *Ongoing* | *Ongoing* | - | *Ongoing* |
| **(Net) Solar radiation** | Sample frequency | *5 min* | *5 min* | *5 min* | *5 min* | - | *5 min* |
| | Record start | *Dec-2010* | *Dec-2010* | *Dec-2010* | *Dec-2010* | - | *Dec-2010* |
| | End of record | *Ongoing* | *Ongoing* | *Ongoing* | *Ongoing* | - | *Ongoing* |
| **Land surface temperature** | Sample frequency | *5 min* | *5 min* | *5 min* | *5 min* | - | *5 min* |
| | Record start | *Dec-2010* | *Dec-2010* | *Dec-2010* | *Dec-2010* | - | *Dec-2010* |
| | End of record | *Ongoing* | *Ongoing* | *Ongoing* | *Ongoing* | - | *Ongoing* |
| **Soil Moisture** | Sample frequency | *5 min* | *5 min* | *5 min* | *5 min* | - | *5 min* |
| | Record start | *Dec-2016* | *Dec-2016* | *Dec-2016* | *Dec-2016* | - | *Dec-2016* |
| | End of record | *Ongoing* | *Ongoing* | *Ongoing* | *Ongoing* | - | *Ongoing* |

Table 2.1: Overview of the available variables, sampling frequency, and measurement periods at each observatory. Each variable is listed with its sampling frequency, record start, and end of record. A dash (–) indicates that data are not available for that station.

## 2.2. Complementary Páramo watersheds

Depending on definition and source, estimates are that around 5-7% of Ecuador's total land surface consists of Páramo (Hofstede et al., 2014). The Páramo form a crucial part of the Ecuador and exists at multiple locations. Therefore, other Páramo watersheds throughout Ecuador are identified to see how these compare to Zhurucay and Quinuas. To identify these watersheds, a publicly available dataset called HydroBASINS was used that contains watershed boundaries at different levels with corresponding characteristics (Lehner et al., 2008; Lehner and Grill, 2013). HydroSHEDS Basins Level

12, the most detailed version, was imported into Google Earth Engine to extract the hydrosheds and characteristics. Figure 2.1 shows the location, numbering, and land cover of the identified watersheds, based on the Mapbiomas classification (MapBiomas Ecuador Project, 2023). The selection of these watersheds aimed to capture a range of diverse locations throughout Ecuador.

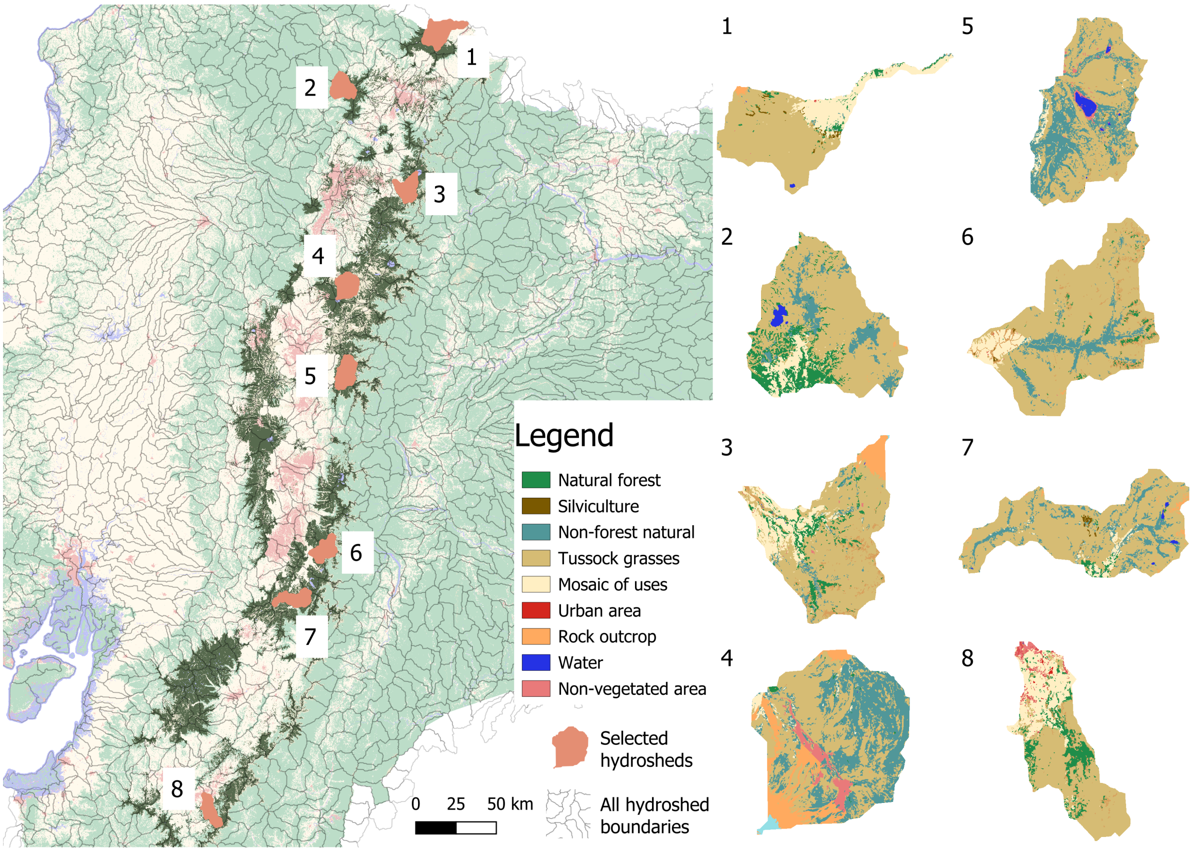

Figure 2.1: All hydrosheds in the Azuay region and landcover classification of selected hydrosheds.

Table 2.2 contains additional information about the watersheds. The latitudinal and longitudinal location with respect to the watershed centroids are calculated in Google Earth Engine and also shown to approximate its location.

| Basin nr. | HYBAS ID | Basin area [km$^2$] | Elevation max [m] | Elevation mean [m] | Elevation min [m] | Lat, Lon |
|---|---|---|---|---|---|---|
| 1 | 6120191830 | 241 | 4713 | 3478 | 2837 | 0.803794, -77.860799 |
| 2 | 6121039290 | 163 | 4478 | 3373 | 2192 | 0.498215, -78.405455 |
| 3 | 6120208780 | 151 | 5785 | 3806 | 2916 | -0.067530, -78.042056 |
| 4 | 6121047290 | 166 | 5869 | 4057 | 3610 | -0.609376, -78.378899 |
| 5 | 6121051790 | 177 | 4288 | 3823 | 3441 | -1.096158, -78.385278 |
| 6 | 6120254390 | 147 | 4302 | 3732 | 3254 | -2.082392, -78.504446 |
| 7 | 6121064220 | 145 | 4405 | 3912 | 3128 | -2.355904, -78.671555 |
| 8 | 6120288400 | 119 | 3366 | 2876 | 1759 | -3.539087, -79.142299 |

Table 2.2: Identified hydroBASINS and characteristics.

## 2.3. Satellite data

One of the challenges of the Páramo system is the lack of widely available, high-quality data. Even though high-quality data is available from observatories in Zhurucay and Quinuas, the diverse environment complicates creating accurate, high-resolution overviews of the region. Such data could be very useful to supplement in-situ data when this is not available, or to validate existing in-situ data.

Remote sensing is an emerging technique which can produce observations over large areas at fixed temporal resolution (e.g. Kalisa, 2025; Frontiers in Environmental Science, 2023). Satellites come in various types, each suited to different applications and in different environments. The choice of satellite depends on the specific parameters being measured, as well as the required resolution, temporal frequency, and environmental conditions. Some common satellite types used for environmental monitoring are the following:

- **Active / passive:** Active satellites emit signals and measure the return signal to gather information about the Earth's surface, such as vegetation or topography changes. Passive satellites detect radiation that the Earth naturally emits, such as thermal infrared. Most active products can penetrate through clouds, on the contrary to most passive products, while active products often have lower spatial resolution. (Earth Science Data Systems, 2021)

- **Microwave:** These satellites use microwave radiation to measure various surface properties. Radiation from these satellites penetrate clouds and can provide data in all weather conditions, but typically have lower spatial resolution. (Earth Science Data Systems, 2021)

- **Reanalysis:** These satellites provide data by assimilating various data sources, such as remote sensing and weather stations, to provide model-based output. This way, gaps due to weather conditions can be filled to ensure continuous data. (Earth Science Data Systems, 2021)

- **Optical and Infrared Satellites:** These satellites measure reflected sunlight and thermal radiation from the Earth's surface. These satellites, especially optical, can produce high-resolution images, but are limited by weather conditions. (Earth Science Data Systems, 2021)

Different types of satellites were deployed to extract parameters that significantly impact the water balance in the Páramo. This study focuses on Soil Moisture (SM), Land Surface Temperature (LST), solar net radiation (Rn) and Land Cover (LC) (see section 2.4.1). The satellites were chosen based on availability in GEE and accuracy according to literature.

### 2.3.1. Soil Moisture

Numerous missions are publicly available that provide estimates of SM. Most remote sensing SM data is based on reanalysis models. In this study, the following satellite missions are used:

- **Soil Moisture Active Passive L4 (SMAP L4):** A data reanalysis product driven by SMAP microwave radiometer observations (Google Earth Engine, n.d.-e);

- **Global Land Data Assimilation System (GLDAS):** A land data assimilation system providing model-based soil moisture (Google Earth Engine, n.d.-b);

- **ERA5-Land:** A European land data assimilation system providing model-based soil moisture (Google Earth Engine, n.d.-a).

These sources differ in spatial and temporal resolution, retrieval methodology and accuracy, but together they offer complementary strengths for characterizing SM trends in the Páramo. Table 2.3 provides an overview of the missions that were used to accumulate data. For all satellites, pixel sizes are approximates at the equator and cadence is shown before further processing. As the pixels sizes are relatively larger compared to other satellite parameters, any data derived from these satellites should solely be used for trend analysis on larger scales, and not to extract distinct soil moisture values on specific locations.

| Mission | Band used | Temporal resolution | Pixel size | Notes |
|---|---|---|---|---|
| **SMAP L4** | `sm_surface` | 3-hourly | ~9 km | Top 0–5 cm volumetric soil moisture. |
| **GLDAS v2.1** | `SoilMoi0_10cm_inst` | 3-hourly | ~0.25° (~27.8 km) | Top 0–10 cm volumetric soil moisture. |
| **ERA5-Land** | `volumetric_soil_water_layer_1` | Hourly | ~0.1° (~9 km) | Layer 1 (0–7 cm) volumetric soil water content. |

Table 2.3: Missions used for satellite/model-based SM (accessed via Google Earth Engine).

### 2.3.2. Solar radiation

Solar radiation is an important parameter for estimating reference evapotranspiration, together with i.e. relative humidity, temperature and wind speed (Valipour, 2015). Accurate measurements of solar radiation are essential for understanding the water cycle, as it directly influences processes like evapotranspiration. Some satellites offer ready-to-use evaporation products, but these products can't be verified, since there is no in-situ evapotranspiration measurements. Therefore, solar net radiation is used as an approximate to estimate $ET$ and validated using available in-situ data.

In this study, the following satellites are deployed for solar radiation:

- **ERA-5 Land:** A European land data assimilation system providing model-based solar radiation (Google Earth Engine, n.d.-a);
- **GLDAS v2.1 NOAH** A land data assimilation system providing downwelling shortwave radiation and net radiation (Google Earth Engine, n.d.-b);
- **MERRA-2:** This NASA product produces hourly solar radiation estimates, including longwave and shortwave radiation (Google Earth Engine, 2025).

The specifications of these satellites can be found in table 2.4. To better approximate evapotranspiration, only daytime radiation was taken by filtering `SWdown` $> 0$ before summation.

| Mission | Band(s) used | Temporal resolution | Pixel size | Notes |
|---|---|---|---|---|
| **ERA5-Land** | `surface_net_solar_radiation`<br>`surface_net_thermal_radiation`<br>`surface_solar_radiation_downwards` | Hourly | ~0.1° (~9 km) | Daytime net radiation $R_n = SW_{net} + LW_{net}$; summed to daily and converted to MJ m$^{-2}$ day$^{-1}$. |
| **MERRA-2** | `SWGNT`, `LWGNT`, `SWGDN` | Hourly time-averaged | ~0.5 (~50 km) | Daytime $R_n = SWGNT + LWGNT$; per-hour to MJ m$^{-2}$ day$^{-1}$ via $\times 3600/10^6$. |
| **GLDAS v2.1 NOAH** | `Swnet_tavg`, `Lwnet_tavg`<br>`SWdown_f_tavg` | 3-hourly | ~0.25° (~27.8 km) | Daytime net radiation: $(SW_{net} + LW_{net}) \times (3\times3600)/10^6$, then summed to daily MJ m$^{-2}$ day$^{-1}$. |

Table 2.4: Missions used for satellite/model-based solar net radiation (accessed via Google Earth Engine).

### 2.3.3. Land Surface Temperature

Another critical parameter for estimating evapotranspiration is Land Surface Temperature (LST). LST is derived from the thermal infrared radiation emitted by the Earth's surface and is sensitive to changes in land cover, vegetation type, and soil moisture. For this study, LST data was obtained from the following three satellite missions:

- **Landsat 8 (LC08):** Atmospherically corrected surface reflectance and land surface temperature derived from Landsat sensors (Google Earth Engine, n.d.-c);
- **MODIS:** Daily direct land surface temperature (LST) and emissivity values (Google Earth Engine, n.d.-d);
- **NASA Visible Infrared Imaging Radiometer Suite (VIIRS):** Daily land surface temperature (LST) and surface reflectance values derived from thermal infrared sensors (Google Earth Engine, n.d.-f).

These missions provide different spatial and temporal resolutions, allowing for comprehensive monitoring of temperature variations across the study area. Additional specifications can be found in table 2.5.

| Mission | Band used | Temporal resolution | Pixel size | Notes |
|---|---|---|---|---|
| **Landsat 8 (LC08)** | `ST_B10` | 16-daily | 30 meters | LST derived using the brightness temperature from the thermal infrared band. |
| **MODIS LST MOD11A1.061** | `LST_Day_1km` | Daily | ~1 km | LST derived from the thermal infrared band. |
| **NASA VIIRS - VNP21A1D** | `LST_1KM` | Daily | ~1 km | Uses Visible Infrared Imaging Radiometer Suite to estimate LST. |

Table 2.5: Missions used for satellite-based LST (accessed via Google Earth Engine).

## 2.4. Maps of the research area

To get a better understanding of the area of interest and specifically to develop a landslide warning system (see chapter 5), various spatial information is required. Based on the publicly available Digital Elevation Model (DEM) and Land Cover Classification (LCC), other maps can be extrapolated or developed. Figure 2.2 shows the DEM and LCC map specifically for the Quinuas catchment.

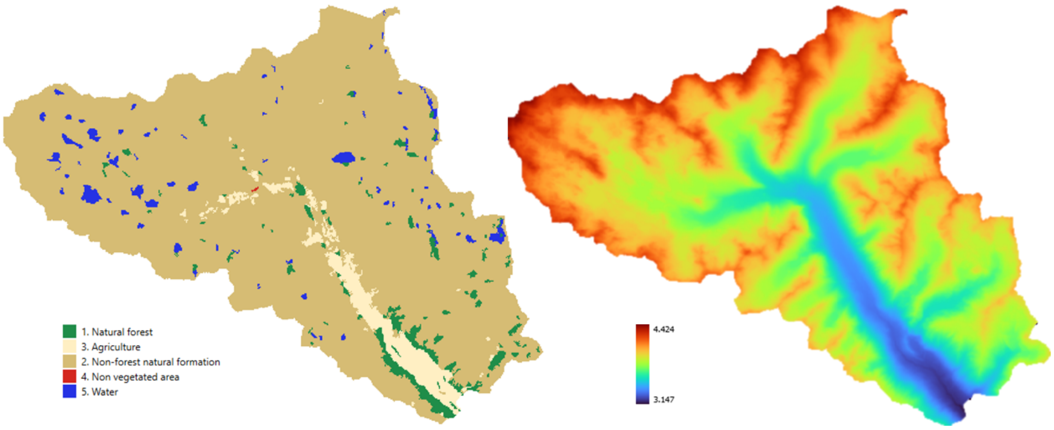

Figure 2.2: Land cover classification (left) and digital elevation model (right) of the Quinuas catchment

### 2.4.1. Land Cover Classification

For the generation of land cover maps, the MapBiomas Ecuador dataset was used (MapBiomas Ecuador Project, 2023). MapBiomas is a project where a series of land cover maps were created through pixel-by-pixel classification of Landsat satellite images using machine learning algorithms, leading to annual mapping of land cover from 1985 to 2023 at a spatial resolution of 30 meters. The pixel-based classification was performed using a Random Forest algorithm, known for it high accuracy for classification algorithms (MapBiomas Ecuador Project, 2023). The classification utilized spectral bands, terrain features, and other environmental variables such as elevation and slope as machine learning features to categorize land cover types.

## 2.5. Synthetic rainfall data

To assess landslide susceptibility, rainfall intensity (mm $h^{-1}$) is required as time input. This way the model can mimic the occurrence of storms with their corresponding duration and rainfall. Although continuous high resolution rainfall data is available for the three different measuring stations in the Quinuas catchment (recorded at 5-minute intervals), the time available for this study did not allow a full selection and analysis of individual extreme storm events. Instead, a rainfall intensity value for each station was determined based on a 24 hour interval for the different return periods: 1 year, 2 years, 5 years and 10 years. This value makes the determination of an intensity duration frequency (IDF) relationship and synthetic storm possible.

### 2.5.1. Derivation of IDF relationships

The relationship between rainfall intensity $I$, duration $D$, and return period $T$ is expressed using the empirical *Sherman–Chow equation* (Chow et al., 1988; Sherman, 1931):

$$I(D,T) = \frac{a(T)}{(D+b)^c} \tag{2.1}$$

Where $a(T)$ is a scale factor specific to the return period, $b$ (min) is a duration offset preventing unrealistically high intensities for very short durations, and $c$ (–) is a decay exponent describing how intensity decreases with increasing duration. Because only 24-hour rainfall depths $H_{24}(T)$ (mm) were available from the extreme value analysis, each curve was anchored at the 24-hour duration (1440 min). The intensity is measured in mm/h, so the 24 hour depth is divided by 24 to get the corresponding value.

$$I(1440, T) = \frac{H_{24}(T)}{24} \tag{2.2}$$

Solving 2.1 for $a(T)$ gives:

$$a(T) = I(1440, T)\,(1440 + b)^{c} \tag{2.3}$$

This ensures that each return period curve passes through the observed 24-hour intensity point. The parameters $b = 5$ min and $c = 0.67$ were adopted, which are within the range typically reported for convective rainfall events ($b = 5$–30 min, $c = 0.6$–0.8; e.g. (*Hydrologic and Hydraulic Design Manual*, 2014; Koutsoyiannis, 1998; *Oregon Department of Transportation: Hydraulics Manual*, 2014). The chosen $b$ value also corresponds to the 5-minute resolution of the available rainfall records. These values are adopted and can therefore be researched in further work. The results of the IDF curves for the different measurement stations and the average of the three are shown in Figure 2.3 below. The corresponding code can be found in the landslide analysis folder **Github** (https://github.com/Matglassaa/Trend_analysis_Paramo).

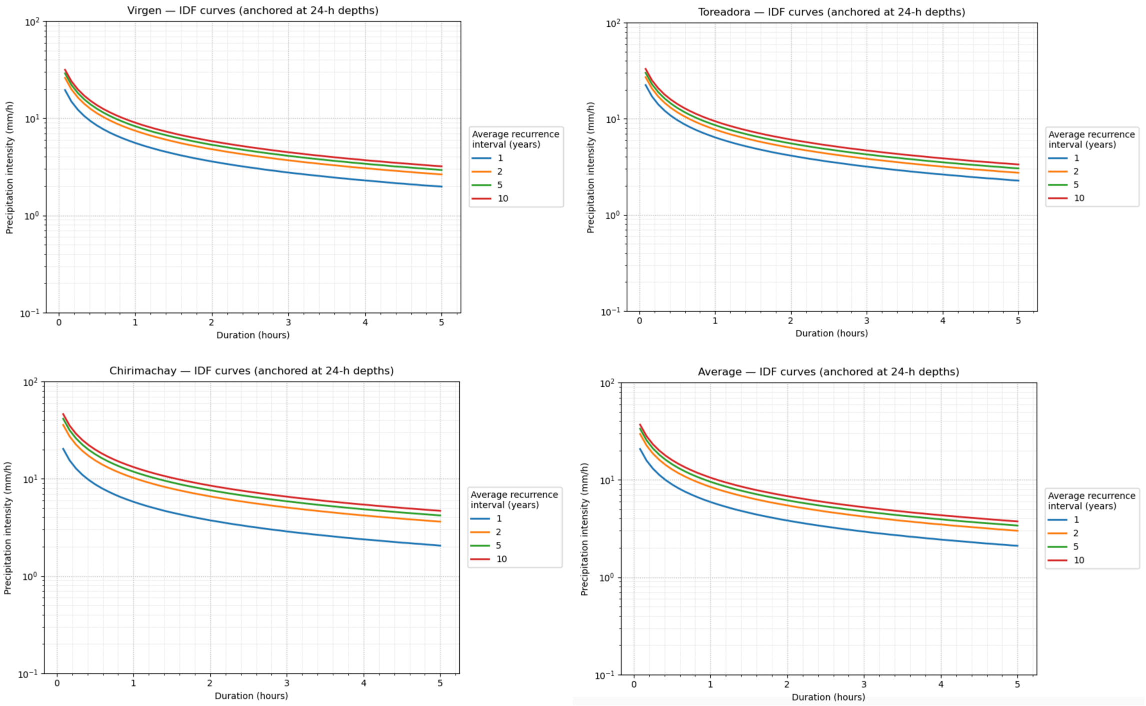

Figure 2.3: Intensity–Duration–Frequency (IDF) of the three stations and the average

### 2.5.2. Generation of the synthetic storm

Using the derived IDF relationships, the synthetic storms were generated per measuring station using the Alternating Block Method (ABM) (Keifer and Chu, 1957) for durations ranging from 0 to 300 minutes at 5-minute intervals. A total storm duration of 300 minutes (5 hours) was chosen to approximate the catchment run off time (the period required for a drop of water to travel from the uppermost to the outlet point of the basin). This duration represents a reasonable hydrological assumption, as there was no data available, and should be refined in future work once such data become available.

The ABM preserves the total rainfall depth derived from the IDF curves while providing a realistic temporal distribution of rainfall suitable for hydrological modelling. The average set of synthetic storms for all measuring stations is found in Appendix **??** and the code is presented in the landslide analysis folder **Github** (https://github.com/Matglassaa/Trend_analysis_Paramo).

Although the generated storms do not replicate specific observed events, they are based on the 24-hour precipitation statistics. Because the Quinuas dataset itself is based on reliable 5-minute measurements, the resulting intensities are consistent with the magnitude and temporal resolution of observed rainfall.

## 2.6. Stakeholder overview

The páramo ecosystems surrounding Cuenca in the Azuay province are crucial for supplying water to local communities and smaller, more remote villages (Buytaert et al., 2006; Mosquera et al., 2023). However, climate change has altered the weather patterns, significantly impacting these ecosystems (Brück et al., 2023). (Future) mining activities also pose a significant risk (Barros et al., 2024; Morin, 2025; The Guardian, 2025). These two threats affect the interests and positions of the stakeholders involved.

While all stakeholders in the area will be affected by the consequences of climate change, such as changed precipitation patterns and temperatures, an even more urgent threat has emerged in the form of the planned large-scale development of the Lomo Larga mining project (Abulu et al., 2025). Research by various parties (Barros et al., 2024; Valladares and Boelens, 2019) indicates unacceptable risks to water quality and ecological balance. Due to the urgent nature of the project, its significant social importance, and its potentially irreversible consequences, the scope of this study is limited to the impact of mining on surrounding stakeholders. A separate study will have to be conducted on the consequences of climate change for these stakeholders.

The construction of the mine creates a complex field of tension involving numerous interfaces (Baccarini, 1996) between stakeholders, whose interests are sometimes conflicting. This makes the issue not only technically complex (e.g. water quality and quantity), but also socially and politically complex. To analyse the connections between these stakeholders and identify areas of potential social conflict, an overview of all stakeholders has been made and divided into three categories: public, private and civil. Public stakeholders include national, regional and local government institutions that create, enforce or monitor policies relating to the Lomo Larga project. Private stakeholders are companies and business entities involved in or benefiting from mining activities. Civil stakeholders include local communities, indigenous groups, research institutions and other members of society who are affected, either directly or indirectly, by the project's social and environmental impacts. (see figure 2.4).

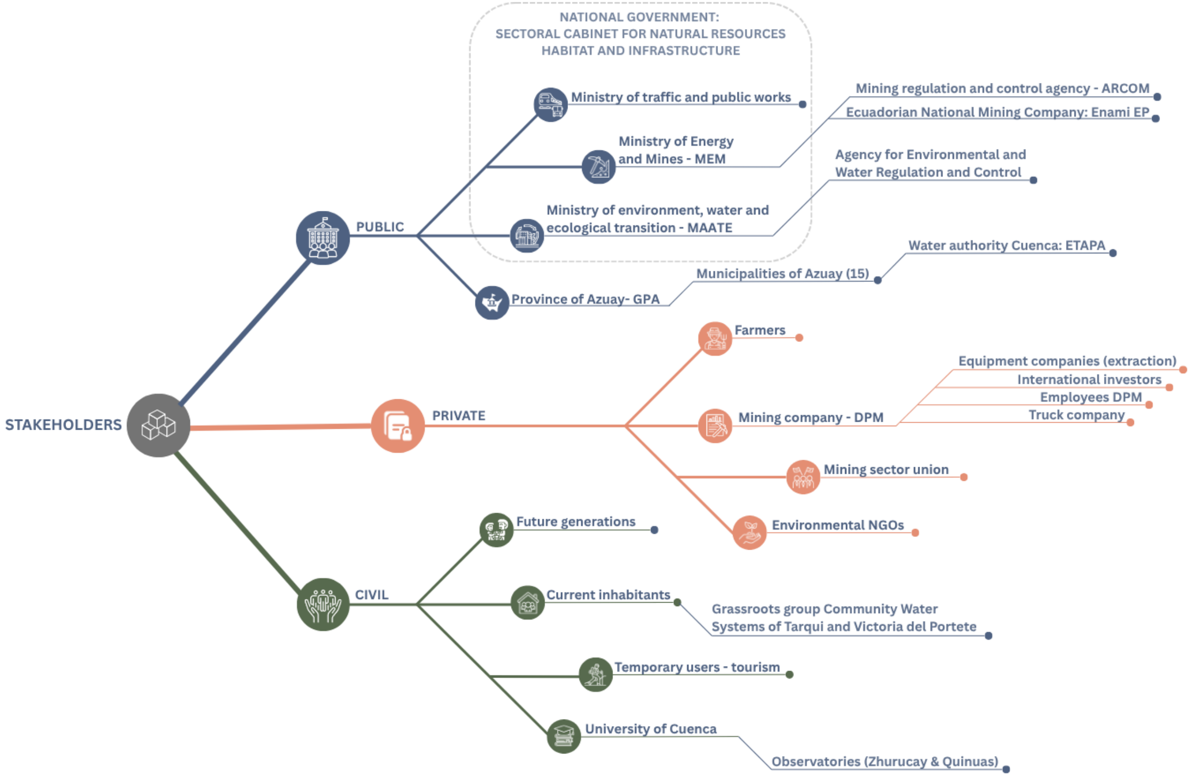

Figure 2.4: Overview of the most relevant stakeholders involved in the Lomo Larga project

Chapter 6 will provide a more detailed overview of these stakeholders and their roles. Furthermore, they will be analysed and evaluated according to the following criteria:

- Level of power
- Degree of interest
- Affectedness
- Attitude towards the Lomo Larga project

Finally, a power–interest matrix and a conflict diagram are developed to visualize stakeholder relationships and potential areas of tension.

# 3

# Satellite data

Even though more and more frequently used, remotely sensed and reanalysis data often still lack accuracy and may contain significant biases. Using in-situ measurements to validate and train the satellite data could therefore be a valuable source to increase the accuracy. This section further discusses the used methods, results and the obtained models that can be used for further analysis.

## 3.1. Methods

The satellite training process can be summarized following the flow chart in figure 3.1. After preprocessing the satellite data in Google Earth Engine, it is combined with the in-situ measurements. Units are harmonized, the data is temporally aligned and daily means are taken. Outliers (for SM: less than 0.55 and greater than 0.85) were filtered and NaN were masked.

To validate the remote sensing data, this untrained, aligned dataset was compared with the in–situ reference. After preprocessing the satellite and combined satellite and in-situ data, the monthly distributions of four standard metrics were computed: Mean Difference (MD), Root Mean Squared Difference (RMSD), unbiased Root Mean Squared Error (ubRMSE) and Pearson correlation $R$. These statistics provide valuable insight in the quality of the satellite data compared to the in-situ data. MD represents the bias, RMSD the accuracy, ubRMSE the accuracy with bias removal, and $R$ the strength and direction of the correlation Zhang et al., 2017. They are calculated as follows (with $s_t$ satellite/model value, $y_t$ in–situ, $N$ aligned daily mean values):

$$\mathrm{MD} = \frac{1}{N}\sum_{t=1}^{N}(s_t - y_t) \tag{3.1}$$

$$\mathrm{RMSD} = \sqrt{\frac{1}{N}\sum_{t=1}^{N}(s_t - y_t)^2} \tag{3.2}$$

$$\mathrm{ubRMSE} = \sqrt{\mathrm{RMSD}^2 - \mathrm{MD}^2} \tag{3.3}$$

$$R = \frac{\sum_{t=1}^{N}(s_t - \bar{s})(y_t - \bar{y})}{(N-1)\,\sigma_s\,\sigma_y} \tag{3.4}$$

where $\bar{s} = \frac{1}{N}\sum_{t=1}^{N} s_t$, $\bar{y} = \frac{1}{N}\sum_{t=1}^{N} y_t$ and $\sigma_s = \sqrt{\frac{1}{N-1}\sum_{t=1}^{N}(s_t - \bar{s})^2}$, $\sigma_y = \sqrt{\frac{1}{N-1}\sum_{t=1}^{N}(y_t - \bar{y})^2}$.

After validation of the satellite data, a conclusion can be drawn whether the untrained data is sufficiently accurate or that training is desirable. If training is necessary, first the systemic bias is removed.

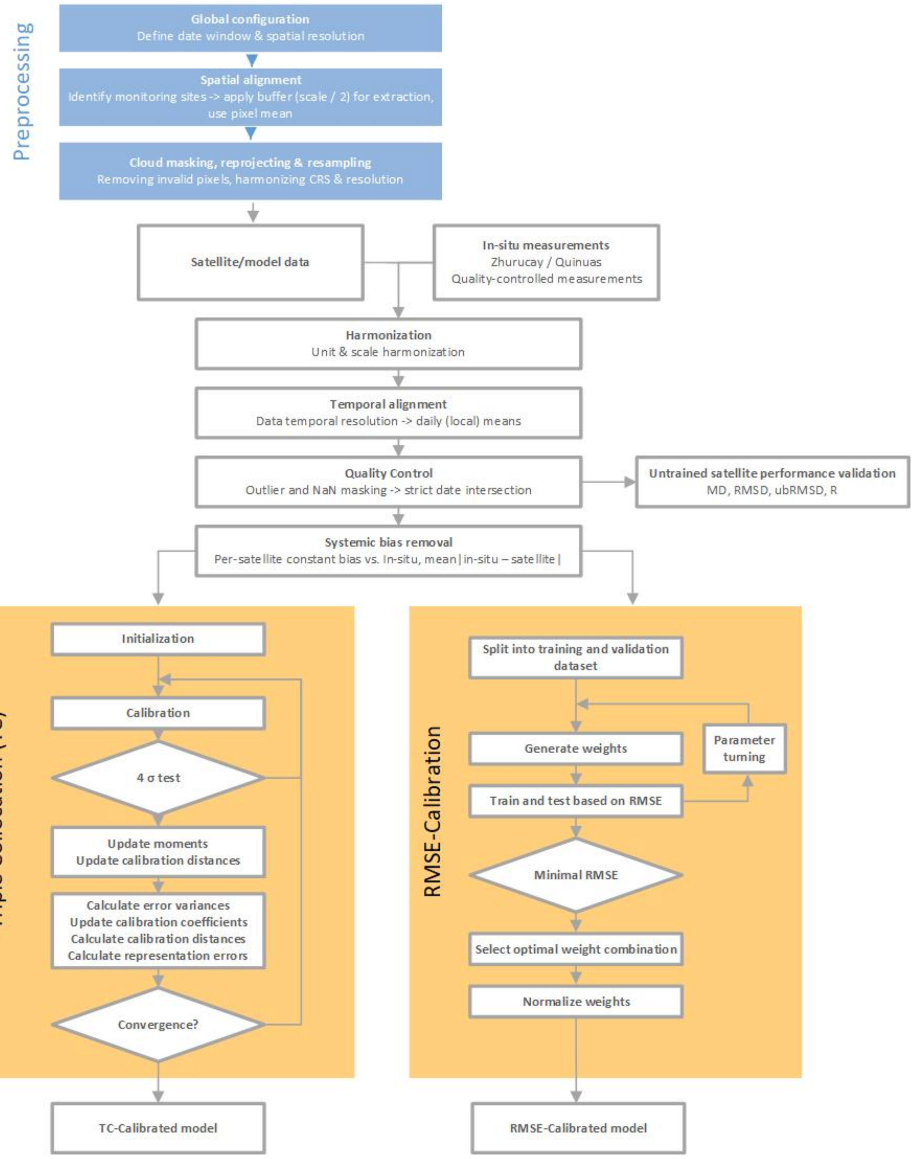

Figure 3.1: Overview of the process of obtaining and training satellite data using in-situ measurements.

For each satellite / model $s_i(t)$ and the in–situ series $y(t)$, a constant bias is estimated robustly on the training intersection, according to the following equation:

$$\tilde{s}_i(t) = s_i(t) + b_i, \qquad b_i = \mathrm{median}[\, y(t) - s_i(t) \,], \tag{3.5}$$

Hereby the accuracy is improved before further training and combining of the satellites. Subsequently, two relatively simple training methods are used, that both rely on similar principles. Let $\tilde{s}(t) = [\tilde{s}_1(t), \tilde{s}_2(t), \tilde{s}_3(t)]^\top$ be the bias corrected SMAP, GLDAS, and ERA5-Land values at day $t$. A convex combination can be formed through:

$$\hat{y}(t) = \sum_{i=1}^{3} w_i\, \tilde{s}_i(t) = w^\top \tilde{s}(t), \qquad \text{s.t.} \quad w \geq 0,\ \mathbf{1}^\top w = 1, \tag{3.6}$$

Subsequently, the weights are determined in 2 different ways:

**(a) Triple Collocation (TC).** TC estimates the random error and uncertainty of three independent measurement systems of the same variable, without declaring any single system “ground truth” (Al-Yaari et al., 2016). Different pairs of bias-corrected satellite data $\tilde{s}_1(t), \tilde{s}_2(t), \tilde{s}_3(t)$ were used in combination with the in-situ data. Once per–system error variances are inferred, a precision–weighted (inverse–variance) model can be constructed that reduces random error.

Assuming the three $i \in \{1,2,3\}$ independent datasets $y^*(t)$ exhibit the following linear error relationship, where for each system:

$$x_i(t) \;=\; \alpha_i \;+\; \beta_i \, y^*(t) \;+\; \varepsilon_i(t), \tag{3.7}$$

with zero–mean errors $\varepsilon_i(t)$ that are mutually uncorrelated and uncorrelated with $y^*(t)$, and (approximately) stationary over the training window. Let $x_i$ be the (bias-aligned) series and $\mathrm{cov}(\cdot,\cdot)$ sample covariances. The TC estimators are:

$$\sigma^2_{\varepsilon_1} = \mathrm{var}(x_1) - \frac{\mathrm{cov}(x_1,x_2)\,\mathrm{cov}(x_1,x_3)}{\mathrm{cov}(x_2,x_3)}, \tag{3.8}$$

$$\sigma^2_{\varepsilon_2} = \mathrm{var}(x_2) - \frac{\mathrm{cov}(x_1,x_2)\,\mathrm{cov}(x_2,x_3)}{\mathrm{cov}(x_1,x_3)}, \tag{3.9}$$

$$\sigma^2_{\varepsilon_3} = \mathrm{var}(x_3) - \frac{\mathrm{cov}(x_1,x_3)\,\mathrm{cov}(x_2,x_3)}{\mathrm{cov}(x_1,x_2)}. \tag{3.10}$$

Given these TC error-variance estimates $\{\sigma^2_{\varepsilon_i}\}_{i=1}^3$, inverse-variance weights were formed and normalized to obtain the following convex model:

$$\tilde{w}_i \;=\; \frac{1}{\sigma^2_{\varepsilon_i}}, \qquad w_i \;=\; \frac{\tilde{w}_i}{\tilde{w}_1 + \tilde{w}_2 + \tilde{w}_3}, \qquad w_i \geq 0, \; \sum_{i=1}^{3} w_i = 1. \tag{3.11}$$

The original data is then multiplied by these weights, leading to a trained estimation of the parameter of interest:

$$\hat{y}(t) \;=\; \sum_{i=1}^{3} w_i \, \tilde{s}_i(t). \tag{3.12}$$

An upside of this method is that none of the datasets are regarded as "ground truth". As the region of interest is highly variable and measurements from discrete locations don't capture this diversity well, models that are overly fitted to these in-situ measurements don't necessarily lead to better results.

However, many of the regions of interest do not at all contain in-situ data. In these cases, comparing models without in-situ data to TC-Calibrated models with in-situ is still useful since it improves understanding of which satellite pairings and weights overall lead to lower TC variances and more complementary skill.

**(b) Minimal RMSE.** In scenarios where in-situ data is unavailable or sparse, it is crucial to develop a model that can be deployed in such regions without relying on ground-based measurements. To achieve this, a second training strategy is implemented, which contrasts with the TC-method by assuming that the available in-situ data represents the reference "ground truth". The goal is to find a convex combination of the bias–corrected inputs $\tilde{s}(t) = [\tilde{s}_1(t), \tilde{s}_2(t), \tilde{s}_3(t)]^\top$ that best matches $y(t)$ on aligned days. This results in a model that minimizes the total error when compared to the reference. The key steps of the calibration process are outlined below:

1. Split into training and validation datasets. To prevent overfitting of the "ground truth" in-situ measurements, the dataset is arbitrarily split in 80% training and 20% validation. The training set is used to fit the model, while the validation set is used to evaluate its performance and ensure generalization.

2. Generate weights. The model aims to find non-negative weights that sum to 1, representing a weighted average of the satellite data inputs (see formula 3.13).

3. Train and test based on RMSE. The training set is used to loop over and train the model by adjusting the weights, with the aim of minimizing the RMSE. The model is then tested using the validation set, where the RMSE is calculated using "new" data (see formula 3.13).
4. Select optimal weights and normalize. The optimal weight combination is chosen based on the combination that leads to the lowest total RMSE. Normalized outputs can be used to deploy on new sites, without in-situ measurements.

The weights are normalized by constraining formula 3.13.

$$\hat{y}(t) \;=\; w^{\top}\tilde{s}(t), \qquad w \in \mathbb{R}^3, \quad w \geq \mathbf{0}, \quad \mathbf{1}^{\top}w = 1. \tag{3.13}$$

$w$ is estimated by constrained least squares (Lawson and Hanson, 1995):

$$\min_{w} \; \sum_{t=1}^{N} \left(w^{\top}\tilde{s}(t) - y(t)\right)^2 \quad \text{s.t.} \quad w \geq \mathbf{0},\; \mathbf{1}^{\top}w = 1. \tag{3.14}$$

## 3.2. Results and interpretation

This section discusses the results obtained by following the methods as described previously.

### 3.2.1. Soil Moisture

| **Mission** | **Bias** | **Weight (RMSE-calibration)** |
|---|---|---|
| **SMAP L4** | +0.4062 | 0.52 |
| **GLDAS v2.1** | +0.4104 | 0.48 |
| **ERA5-Land** | +0.2929 | 0 |

Table 3.1: Results of SM-satellite models using RMSE-calibration.

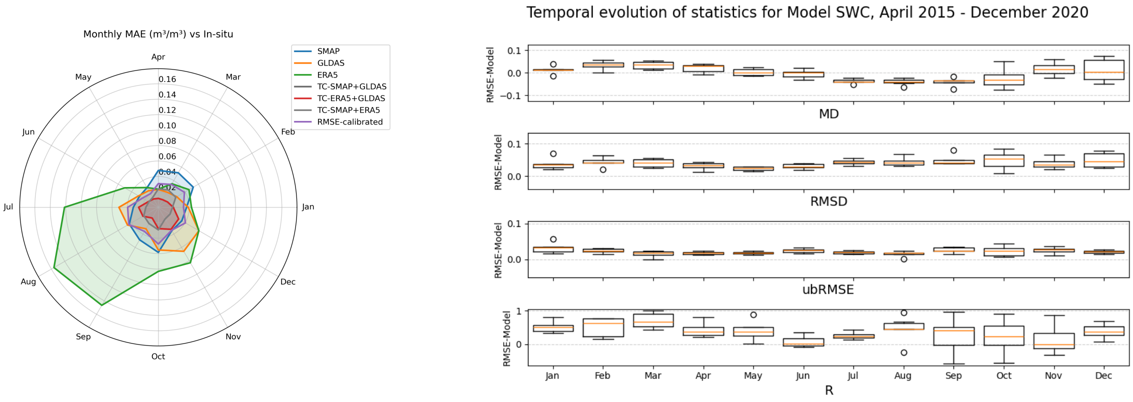

(a) (b)

Figure 3.2: (a) MAE of different SM-models compared to in-situ. (b) Monthly boxplots of $MD$, $RMSD$, $ubRMSE$, and $R$ for deployable RMSE-trained satellite model.

Results from the training of Soil Moisture data can be found in table 3.13. In figure 3.4, the untrained SM data is evaluated against the in-situ data. Some clear patterns are noteworthy. Firstly, all satellites contain a significant, consistent monthly bias (MD). Also, both $R$ and RMSD / ubRMSE vary significantly throughout the year. A cause might be seasonally changing forcing conditions, such as precipitation patterns (i.e. "dry" and "wet" season) (e.g. Colliander et al., 2019; Muñoz-Sabater et al., 2021; Spennemann et al., 2015; Zhang et al., 2017). Especially the traditionally more changeable weather months of September, October and November (World Bank, n.d.) produce significantly worse results than the other years, with median R around 0 and significant biases. Concluded can be that the individual satellites need training to allow generation of reliable results in other areas.

The results of both training strategies are shown in figure 3.2. The figure displays the Mean Absolute Error (MAE) of the model using different training strategies compared to in-situ data. Again, it is observable that the changeable months of S̃eptember and October overall produce worse results than the other months, also after training. Interpretation of this figure must be done very cautiously, since for all TC-methods, the in-situ data itself was directly incorporated in the model instead of only training (determining 'weights'), and will therefore generally result in lower MAE-values. Some noteworthy observations are the general significant improvement of both TC and RMSE-models compared to non-trained models, with the exception for the month June.

In figure 3.3, the temporal evolution during 2020 of the in-situ data is shown against the 3 satellites, the TC (SMAP-ERA5-in-situ) model (which performed the best, see figure 3.2) and the RMSE-calibrated model. Clear seasonal variability can be observed, which is captured well by both models. Individual peaks are also captured, although in some cases with a delay and diffused compared to the in-situ measurements. Timeseries of data used for model training can be found in Appendix A. Chapter 9 contains more information about how these results should be interpreted.

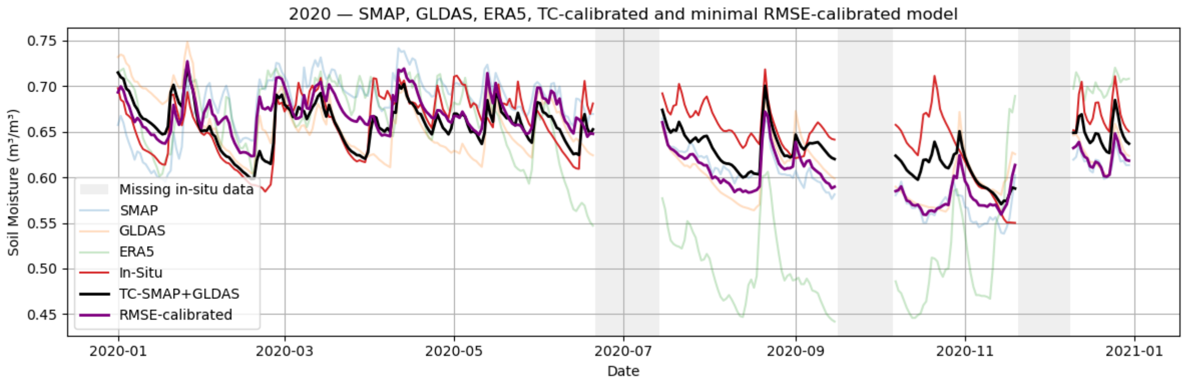

Figure 3.3: Validation of model results for the year 2020.

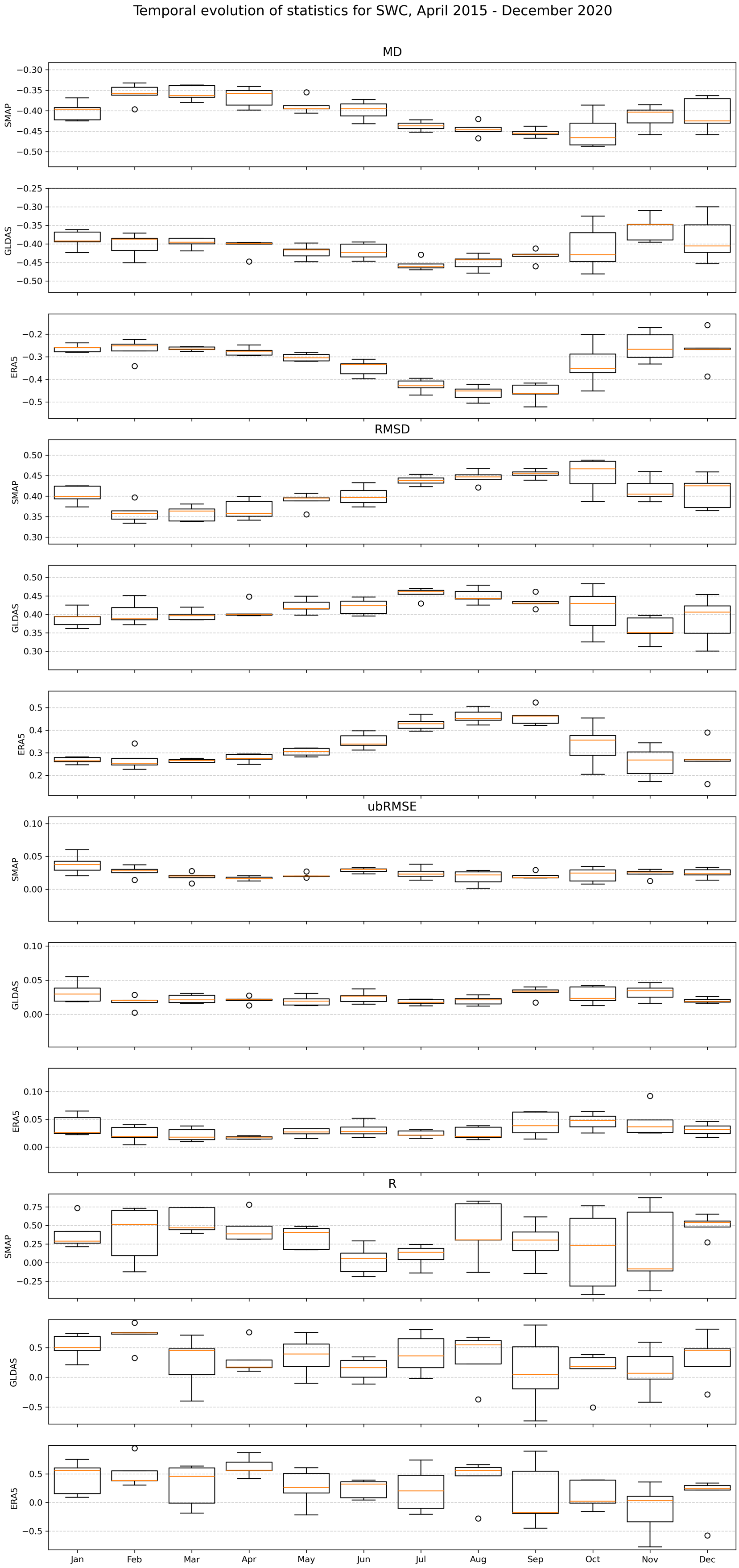

Figure 3.4: Monthly boxplots of $MD$, $RMSD$, $ubRMSE$, and $R$ for SMAP L4, GLDAS, and ERA5-Land against in–situ observations, pre-training. Boxes show IQR with medians; whiskers use the 1.5 IQR rule.

### 3.2.2. Solar Radiation

Untrained satellite data on Solar Net Radiation had a significant bias for all used satellite products. From figure 3.5, it can be observed that the average monthly absolute error is significant when compared to the total radiation. The error is mainly caused by the fact that the satellites are not able to capture local radiation peaks very well, thereby contributing significantly to the total residuals. This may be caused by the temporal resolution of the satellite observations, which may not well capture radiation conditions in cloudy and highly variable weather conditions such as around Cuenca. The fact that 3-hourly observations from GLDAS display similar residuals compared to hourly (model) observations from ERA5 or MERRA2 confirm this.

Due to this significant bias, remote sensing obtained Solar Net Radiation is not further considered, as no reliable SNR estimations can be made.

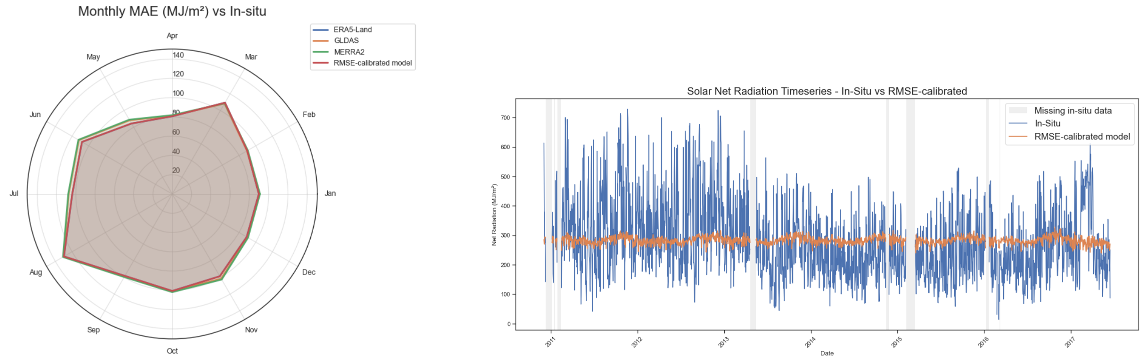

(a) (b)

Figure 3.5: (a) MAE of different Solar Net Radiation models compared to in-situ. (b) Timeseries of in-situ measurements vs. satellite model approximations.

### 3.2.3. Land Surface Temperature

After preprocessing the Land Surface Temperature observations in GEE, including explicitly built-in cloud masking algorithms that automatically detect and remove cloudy pixels, very few observations remained. On average, every 6 days an observation was made by *either* of the utilized satellites, with significant differences in different times of the year (almost no observations in October and November of the years of interest). Even though both MODIS and Landsat contain gap-filling algorithms, the clouds where too persistent to produce sufficient data points for further processing. Therefore, it may be concluded that remote sensing LST observations in heavily clouded regions such as the Páramo are not feasible.

# 4

# Trend Analysis and Forecasting

The second step in this report is to take a look at the data collected at the observatories and identify trends, create a model to understand the components within the natural process and evaluate the forecasting ability of this model. The different measured variables available are detailed in Table 2.1 of section 2.1. A full trend analysis and forecasting procedure of all variables is out of scope for this report, thus the focus will lie on three specific variables.

1. Temperature: daily mean air temperature is primary driver for many meteorological and hydrological variables (Arrieta-Pastrana et al., 2022). Additionally it influences vegetation, which in their are important to the water balance and slope stability.
2. Precipitation: monthly cumulative precipitation gives insight into the hydrological cycle of a ecosystem. Changes in precipitation affect water quality and slope stability.
3. Soil moisture: daily mean soil moisture content is an important factor for slope stability as it is related to the cohesion of individual grains.

The chapter is structured by first applying a simple, non-parametric statistical test to the variables: the Seasonal-Mann Kendall (Hirsch and Slack, 1984) test. This method is often employed with meteorological data to determine the presence of a statistically significant trend. This is followed by the implementation of a more complex dynamic time series model, which is used to accurately capture the true behaviour of the time series and predict how future patterns might evolve. The chapter concludes with the presentation of the results and a note by the author on the findings.

## 4.1. Seasonal Mann-Kendall test

For a multi-year trend analysis, the seasonal Mann-Kendall (SMK) and the hamed rao modification test (RMK) were selected as described by Hirsch and Slack, 1984 and Hamed and Rao, 1998. These non-parametric tests, which mean they are distribution free thus are not required to have normalized input data (Helsel and Hirsch, 2002), are an adaptation of the original Mann-Kendall test by Mann, 1945. The SMK test is designed to deal with seasonal cycles, which are often present in climate data, by looking separately at each defined season. This test is specifically employed because the temperature time series from the observatories contains a distinct yearly cycle. Given a time series $x = \{x_1, x_2, \ldots, x_n\}$, the seasonal Mann-Kendall test statistic $S_i$ is defined as:

$$S_i = \sum_{i=1}^{n_i - 1} \sum_{j=i+1}^{n} \operatorname{sgn}(x_j - x_i), \quad \operatorname{sgn}(x_j - x_i) = \begin{cases} +1, & \text{if } x_j - x_i > 0, \\ 0, & \text{if } x_j - x_i = 0, \\ -1, & \text{if } x_j - x_i < 0. \end{cases}$$

$$\mathrm{S}_{\mathrm{total}} = \sum_i S_i, \quad \mathrm{Var}(S_i) = \sum_i Var(S_i)$$

where $t_t$ is the number of tied values in the $t$-th group of ties, and $q$ is the number of tied groups. The standardised test statistic $Z$ is given by:

$$Z = \begin{cases} \dfrac{S-1}{\sqrt{\mathrm{Var}(S_{tot})}}, & \text{if } S > 0, \\ 0, & \text{if } S = 0, \\ \dfrac{S+1}{\sqrt{\mathrm{Var}(S_{tot})}}, & \text{if } S < 0. \end{cases}$$

$$p = 2(1 - \Phi(Z))$$

where $S_{tot}$ is a summation of all seasonal test statistics $S_{tot} = \sum_{i-1}^{n} S_i$. A positive $Z$ indicates an increasing trend, while a negative $Z$ indicates a decreasing trend. The null hypothesis $H_0$ (no monotonic trend) is rejected at significance level $\alpha$ if $|Z| > Z_{1-\alpha/2}$, where $Z_{1-\alpha/2}$ is the critical value of the standard normal distribution (Hirsch and Slack, 1984). The trend is also considered statistically significant when the corresponding p-value is smaller than $\alpha$, whihc often is set to 0.05. A small p-value therefore indicates that the observed trend is unlikely to have occurred by chance, leading to rejection of the null hypothesis.

The RMK is used when autocorrelation plays a significant role in the time series, which often is the case in climate and weather variables. The RMK test accounts for autocorrelation by computing a correlation factor for the autocorrelation between ranks (Hamed and Rao, 1998). The downside of this test is that it does not account for seasonality; the test statistic ($S$) and test statistic variance ($Var(S)$) are computed over the whole series and not per season. Therefore, the data has to be de-sectionalized before the test can be applied.

Alongside the SMK and RMK, Theil-Sen's slope as described in Sen, 1968, was used to determine the trend. Theil-Sen's method is robust against outliers and non-normal residuals, making it highly suitable for environmental and hydrological time series (National Center for Atmospheric Research, 2014, Sen, 1968). The slope is calculated on a seasonal (monthly) basis for the SMK and over the whole dataset for the RMK test. This results in $n$ individual slopes, where $n$ is the number of defined periods within the year. The overall slope is computed as the median of these $n$ slopes, a method chosen because the non-detrended data is assumed to have no particular distribution. Given a time series $\{(t_i, x_i) : i = 1, 2, \ldots, n\}$, where $t_i$ denotes time and $x_i$ the observed value, the slope between all possible pairs of observations $(i, j)$ with $j > i$ is computed as:

$$Q_{ij} = \frac{x_j - x_i}{t_j - t_i}, \qquad 1 \le i < j \le n$$

This produces $N = \frac{n(n-1)}{2}$ slope estimates. The Theil-Sen's slope estimator $\hat{Q}$ is defined as the median of these $Q_{ij}$ values and the intercept $\hat{B}_i$ can be computed as:

$$\hat{Q} = \mathrm{median}\{Q_{ij} : 1 \le i < j \le n\} \qquad \hat{B}_i = x_i - \hat{Q}\, t_i, \quad i = 1, 2, \ldots, n.$$

Then, taking $\hat{B} = \mathrm{median}\{\hat{B}_i\}$ The estimated regression line is therefore: $\hat{x}(t) = \hat{Q}\, t + \hat{B}$.

### 4.1.1. Methodology

In order to implement the SMK and RMK tests combined with Theil's-Sen slope, the python package `pymannkendall`, developed by Hussain and Mahmud, 2019 was used. This package provides all the different Mann-Kendall tests and implements the Theil-Sens's slope automatically. Thus, the only manual thing which had to be done was the de-seasonalization of the data before using the RMK test. Using the 'statsmodels.STL' function (Balladares Varela et al., 2018) the time-series was de-seaseasonalized with a stochastic trend, allowing for a better fit.

Interpreting the results was done by combining the outcome of the SMK and RMK test for each station. Given that both of the p-values fell within the range of 0.05-0.00, a possible trend was detected. If the two p-values gave different results the result was classified as uncertain.

## 4.2. Implementing a dynamic time series modes for meteorological and satellite data

A dynamic time series model was selected for the trend analysis on the meteorological data. This choice is motivated by the property of dynamic time series models to allow past values or states to influence the present; this contrasts with static models, which only account for the current state (Maitra, 2025). The exact model implemented in this report is a Unobserved Components Model (UCM). The UCM belongs to a special class of dynamic models, namely 'Structural time series models' whereby the model is formulated in terms of unobserved components (Harvey, 2006). Examples of components are trends, seasonal cycles and autocorrelation. In meteorological applications, UCM's are particularly advantageous because they allow decomposition of the observed series into interpretable components such as long-term trends, seasonal cycles, and irregular variations. This decomposition helps understanding the underlying climatic processes rather than merely fitting statistical patterns. Additionally, using the model a projection of future expected values can be made. A dynamic model can be represented as:

$$y_t = f(y_{t-1}, y_{t-2}, \dots, x_t, x_{t-1}) + \epsilon_t$$

In this equation $y_t$ is the dependent variable at time t, $x_t$ represents exogenous (input) variable(s), $f()$ is the function describing how past and current values affect $y_t$ and $\epsilon_t$ represents white noise. The shape of a structural model, which is used in this report, can be represented as a combination of several equations relevant to each component. A simple structural model which contains a level and trend component can be represented as:

$$y_t = \mu_t + \tau_t + \epsilon_t$$

$$\mu_t = \mu_{t-1} + \tau_{t-1} + \eta_t$$

$$\tau_t = \tau_{t-1} + \zeta_t$$

Where $\epsilon_t \sim N(0, \sigma_\epsilon^2)$ is the observation noise, $\eta_t \sim N(0, \sigma_\eta^2)$ is the level disturbance and $\zeta_t \sim N(0, \sigma_\zeta^2)$ the trend disturbance (Maitra, 2025 & Klees, 2025). By adding more components, the full structural model can be created using two equations in matrix notation: the observation equation and state equations. The observation equation tells us how the observations relate to the hidden states defined in the state equation and the state equation tells us how the hidden system may evolve.

$$y_n = H_n x_n + v_n \quad v_n \sim N(0, V_n)$$

$$x_n = A_n x_{n-1} + w_n \quad w_n \sim N(0, W_n)$$

Above $y_n$ relates to all the observations, and the vector $x_n$, matrices $H_n$, $A_n$, $V_n$ and $W_n$ are all model specific. The vector $x_n$ contains the coefficients for each component, $H_n$ is the design matrix, which transforms the state vectors into observations, and $A_n$ is the state transition matrix which describes how the $x_n$ evolves over time. Finally, $V_n$ and $W_n$ represent the white noise component and the state vector disturbances.

The optimal estimates of the unobserved state vector are obtained through the Kalman filter and smoother. The Kalman filter recursively updates the estimates of the unobserved components as new observations become available, providing the optimal real-time (filtered) estimates $E[\alpha_t \mid y_{1:t}]$. Once the entire dataset is observed, the Kalman smoother combines the forward and backward recursions to obtain refined smoothed estimates $E[\alpha_t \mid y_{1:T}]$, which minimize the mean square error over the full sample (Klees, 2025). The time series model is a Gaussian model, assuming that all the disturbances $W_n$ and initial states are normally distributed (Harvey, 2006). The filter estimates the mean and covariance matrix of the conditional distribution per time step. The conditional mean then acts as the mean square error estimator, ensuring the best realisation possible for all observations (Harvey, 2006 & Klees, 2025). One of the advantages of Kalman-filter has to do with its handling of missing values, which is a common occurrence in measured time series as a result of errors in hardware or renovations.

When the Kalman filter encounters a missing observation at time step $t$, it skips the update equation and goes directly to the prediction step. This ensures a continuous prediction of the model, even when no previous time step data is available.

After model refinement and selection a forecast can be made to evaluate the performance of the model for future observations. For this process the model uses the previously selected parameters and computed state's. The model parameters govern the stochastic behaviour per time step while the model state at that time step shows the current level, slope and seasonal phase of the model is. The confidence intervals are computed as a result of the AR() processes from the trained model. The coefficients for this component shows the possible range that might fall within the 95% confidence interval.

### 4.2.1. Methodology

The Unobserved Component Model (UCM) was implemented in a Python environment using the `statsmodels` package's UCM function (Perktold et al., 2024). The package offers various functions to help with diagnostic tests and forecasting, making interpretations of results and model sections straightforward. The methodology to obtain a well fitting model is adopted from (Klees, 2025), with the step wise process portrayed in figure (4.1). The Unobserved Components function in statsmodels does all the mathematical computation, including creation of the state space equations, selection of initial values, implementing maximum likelihood and the application of the Kalman filter (Perktold et al., 2024). Consequently, our focus can be fully directed to choosing an optimal model for the time series.

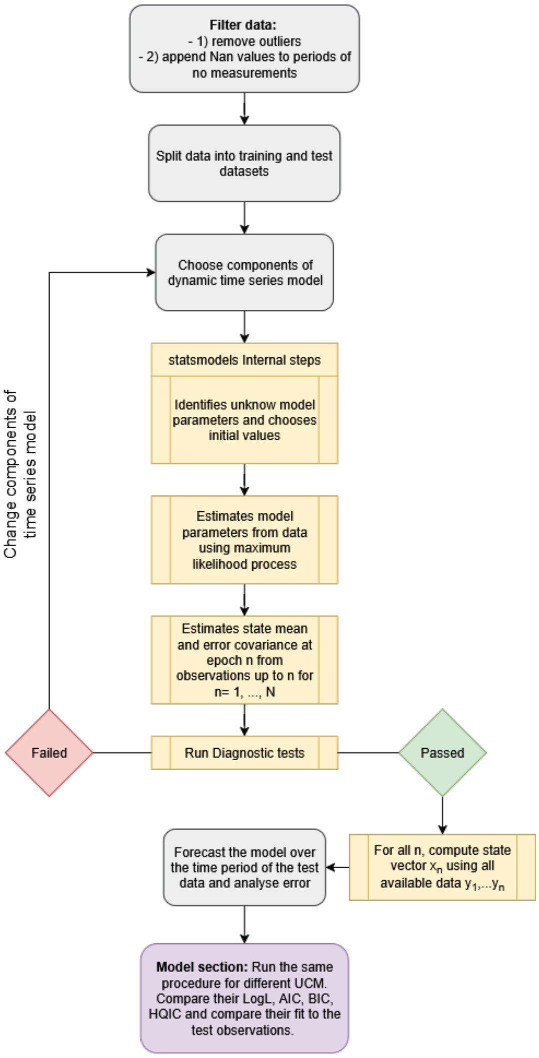

Figure 4.1: Procedure of analysing and forecasting time series using the *statsmodels.tsa.UnobservedComponents* function (Klees, 2025).

Before implementing the Unobserved Component Model (UCM), several data preprocessing and preparation steps were necessary. These steps ensure data integrity and establish the necessary training and test sets for model validation. The procedure is structured as followed:

- **1:** Remove outliers from the observed data.
- **2:** Identify periods where no observations were made or measurement device failure occurred, and transform the data to NaN values.
- **3:** Splitting the data into a training and test dataset: at least a full calender year of test data should be available.

The above steps are essential as outliers and false observations (related to step 2) lead to bias in the estimation of state space parameters. Furthermore, model performance is validated by analysing the mean error and error distribution across all time steps. The components within the model are defined after the preprocessing steps. The statsmodels package then internally defines the state space model equations and using the Kalman filter and smoother function estimates the optimal values. Finally a diagnostics test is run, producing an overview of the remaining errors the model produces. The error distribution may tell us if the model has sufficiently captured the true underlying processes of the time series. In order for a model to be accepted the following three tests have to be passed:

- **Ljung-Box test:** tests if autocorrelation is present in the residuals.
- **Jarque-Bera test:** tests normality of the residuals.

- **Heteroskaticity:** tests if the variance of the residuals is constant.

If all diagnostic tests are satisfied, the model is deemed to be sufficiently capturing the underlying process of the time series. Other models can be tested too, and if passed the model with the best fit may be chosen. `Statsmodels` offers several tests to evaluate the performance of models such as Lok-likelihood, AIC, BIC and HQIC. The model with the lowest combined score of all is generally accepted to be the best fit model. The exact procedure which was followed is depicted in Figure 4.1.

## 4.3. Results

### 4.3.1. Mann-Kendall test

The SMK and RMK tests were applied to the temperature, precipitation and soil moisture data to evaluate the existence of a significant trend within each season. The magnitude of the identified trends was measured using the Theil-Sen's slope method. An overview of the results from the two tests is presented in table 4.1 which includes the p-values per test and the slope.

| Station | Seasonal MK p | Seasonal MK Slope | Robust MK p | Robust MK Slope |
|---|---|---|---|---|
| **Temperature** | | | | |
| Toreadora | 1.4972e-03 | 0.097138 | 5.9986e-02 | 0.000215 |
| Virgen | 9.1356e-03 | 0.071586 | 9.8596e-02 | 0.000157 |
| Chirimachay | 2.5449e-02 | 0.060009 | 2.8850e-01 | 0.000089 |
| Balzay | 5.0558e-04 | 0.139293 | 8.6502e-03 | 0.000470 |
| Zhurucay | 1.6166e-08 | 0.054656 | 8.1751e-06 | 0.000149 |
| **Precipitation** | | | | |
| Toreadora | 1.2745e-01 | -1.322501 | 1.3508e-01 | -0.120933 |
| Virgen | 3.2764e-02 | -1.836753 | 5.2579e-02 | -0.226486 |
| Chirimachay | 1.4080e-01 | 1.213586 | 6.1075e-01 | 0.061876 |
| OPNC | 2.6277e-02 | 4.991412 | 1.5263e-01 | 0.332630 |
| Balzay | 9.4302e-01 | 0.417500 | 8.0411e-01 | -0.083177 |
| Zhurucay | 4.9351e-02 | -1.583270 | 5.6548e-07 | -0.154484 |
| **Soil Moisture** | | | | |
| Zhurucay | 7.8649e-01 | -0.000118 | 6.0926e-01 | -0.000023 |
| Quinuas | 8.3565e-04 | -0.001782 | 1.3025e-03 | -0.000180 |
| 6120191830 | 1.2771e-05 | 0.003521 | 2.0026e-02 | 0.000343 |
| 6120208780 | 7.5784e-02 | -0.000685 | 4.6097e-02 | -0.000076 |
| 6120254390 | 5.7949e-02 | -0.000745 | 3.6026e-04 | -0.000068 |
| 6120288400 | 4.2946e-04 | -0.002389 | 2.9425e-04 | -0.000179 |
| 6121039290 | 1.5770e-03 | -0.001434 | 4.5167e-03 | -0.000129 |
| 6121047290 | 4.8880e-01 | -0.000340 | 5.2146e-01 | -0.000035 |
| 6121051790 | 7.8649e-01 | -0.000115 | 8.2475e-01 | -0.000011 |
| 6121064220 | 5.4978e-12 | -0.003322 | 1.8221e-10 | -0.000272 |

Table 4.1: Comparison of Seasonal and Robust Mann–Kendall test p-values and slopes for Temperature, Precipitation, and Soil Moisture across all stations. A p-value $< 0.05$ indicates a statistically significant trend. The direction of the slope (negative or positive) indicates whether the trend is increasing or decreasing.

Looking at the p-values in the table results of the seasonal and robust Mann-Kendall tests we may observe that the SMK and RMK tests do often not not provide the same result. Looking for instance at the Toreadora station for temperature, the Null hypothesis $H_0$ for the SMK test is rejected while the Null hypothesis for the RMK test is accepted (p-value = 0.06), although with a small margin. The SMK test predicted a trend in 13 time-series. For temperature it even predicted a trend at all 5 stations. The RMK test on the other hand only predicted a trend in 10 time-series. For the temperature data for instance it only predicted a significant trend at two locations: Balzay and Zhurucay.

For the temperature measurements **five** of the **five** stations show a significant trend with the SMK test and only **two** stations show a significant trend with the RMK test. The Robust Mann–Kendall (RMK) test yielded p-values of 0.059 for the Toreadora station and 0.098 for the Virgen station. The p-values for the Virgen and especially the Toreadora stations are near the conventional 0.05 significance threshold, indicating a borderline result. The null hypothesis of no trend can therefore not be confidently rejected or accepted, suggesting an inconclusive indication of a possible trend. Moreover, both test methods resulted in a positive value of the slopes for all stations in the range of 0.05 - 0.1 degrees per month for the SMK test and resulting is a slope of 0.6 to 1.2 degrees per year. The slopes of the RMK test ranged from 0.00008 to 0.0004 degrees per day equalling a slope of 0.03 to 0.15 degrees per year. The latter one is a more realistic value, especially when looking at the raw time-series. Overall there seems a good possibility of an increasing trend in the temperature data in the Quinuas and Zhurucay data as most of the tests resulted in a significant increasing trend

The monthly cumulative precipitation measurements only show a (borderline) significant trend at **three** of the **five** SMK test results and only **one** of the RMK test results. Moreover, the slope values vary in sign, being either positive or negative depending on the direction of the trend. Consequently it is hard to justify the existence of a uniform trend in the Zhurucay and Quinuas catchments and surrounding area. A possible interesting observation relates to the direction of the slopes. The highest-elevation stations — Toreadora, Virgen, and Zhurucay — all exhibit negative slopes in their time-series, whereas the lower-elevation stations — Chirimachay, OPNC, and Balzay — predominantly show positive slopes. Both the SMK and RMK tests indicate a significant trend at the Zhurucay station, with a borderline significant (nearly rejected) trend at the Virgen station. Overall, this pattern may suggest a decrease in monthly cumulative precipitation at the higher-altitude Páramo stations, while lower-lying stations surrounding the Páramo appear to experience increasing precipitation.

Finally, the results of the soil moisture data collected through satellite data as described in chapter 2. The SMK test predict a significant trend at 5 of the 10 catchments, with 2 borderline non-rejected $H_0$ tests. The RMK tests rejects the $H_0$ test **seven** times, indicating an overall significant trend. Only one of the nine stations – ... – resulted a positive slope. Overall, the analysis indicates a statistically significant decreasing trend in soil moisture, as evidenced by the rejection of the null hypothesis and the predominance of negative slope values.

### 4.3.2. Unobserved Components Model

In the following section, the Unobserved Components model results are presented. The same data as used for the trend analysis was used. All the results are generated using the `statsmodel.tsa.UnobservedComponents` class in python. The flowchart presented in figure 4.1 presents the workflow followed for each variable. First of all the data was pre-processed to make it suitable for the analysis. Secondly the model has to pass all the necessary statistical tests. Finally, the best model is chosen taking into account model fit and forecasting ability. The full code can be accessed through **Github** (https://github.com/Matglassaa/Trend_analysis_Paramo).

For the air temperature and precipitation, the full dataset at 5 minutes resolution was resampled to daily/weekly or monthly mean air temperature depending on which resampling data managed to pass all diagnostics tests. Using the data of different stations, model components were added until the best configuration was reached. A summary of the components in each model per variable can be found in table 4.2. There the model components, outcome of statistical test for the model created and the goodness of fit w.r.t. the test data is presented. Additionally an overview of the test statistics, 'Jarque-Bera', 'Heteroskaticity' and 'Normality' can be found. Moreover the tables provides and overview of the RMSE (root mean square error) and variance of the residuals produced by comparing the forecast with the test data. They tell us the how well the model was able to predict future values (test data) based on its own mean prediction.

| **(1) Temperature** | | | | | |
|---|---|---|---|---|---|
| **Site** | **Zhurucay** | **Toreadora** | **Virgen** | **Chirimachay** | **Balzay** |
| **(a) Model Components** | | | | | |
| Level | True | True | True | True | True |
| Trend | True | False | True | False | False |
| Stochastic trend | Fals | False | False | False | False |
| Seasonality | 12/2 | 365/2 | 365/2 | 365/2 | 52/1 |
| AR Order | 2 | 1 | 2 | 2 | 1 |
| **(b) Statistical Test Results** | | | | | |
| JB p-value | 0.28 | 0.00 | 0.00 | 0.00 | 0.06 |
| Q p-value | 0.81 | 0.64 | 0.36 | 0.27 | 0.78 |
| H p-value | 0.68 | 0.09 | 0.98 | 0.41 | 0.82 |
| **(c) Forecast / Data Fit Metrics** | | | | | |
| RMSE | 0.67 | 1.22 | 1.22 | 1.01 | 2.73 |
| Variance of Residuals | 0.32 | 1.05 | 0.77 | 0.83 | 3.36 |

| **(2) Precipitation** | | | | | |
|---|---|---|---|---|---|
| **Site** | **Zhurucay** | **Toreadora** | **Virgen** | **Chirimachay** | **Balzay** |
| **(a) Model Components** | | | | | |
| Level | True | True | True | True | True |
| Trend | False | True | True | True | False |
| Stochastic Trend | False | False | False | False | False |
| Seasonality | None | None | None | None | 12/1 |
| Regressor | None | AirTC_Avg | None | None | AirTC_Avg |
| AR Order | 1 | 1 | 1 | 1 | 1 |
| **(b) Statistical Test Results** | | | | | |
| JB p-value | 3.27e-04 | 9.28e-01 | 5.95e-01 | 3.92e-01 | 9.48e-07 |
| Q p-value | 0.835 | 0.914 | 0.981 | 0.666 | 0.448 |
| H p-value | 0.779 | 0.598 | 0.629 | 0.291 | 0.000449 |
| **(c) Forecast / Data Fit Metrics** | | | | | |
| RMSE | 49.173 | 62.003 | 45.995 | 45.261 | 120.459 |
| Variance of Residuals | 2417.937 | 3835.226 | 2065.112 | 2048.527 | 13955.859 |

| **(3) Soil Moisture** | | | | | | | | | | |
|---|---|---|---|---|---|---|---|---|---|---|
| **Site** | **Zhurucay** | **Quinuas** | **Basin 1** | **Basin 2** | **Basin 3** | **Basin 4** | **Basin 5** | **Basin 6** | **Basin 7** | **Basin 8** |
| **(a) Model Components** | | | | | | | | | | |
| Trend | False | True | True | False | True | False | False | True | True | True |
| Stochastic Trend | False | True | True | False | False | False | False | False | True | False |
| Seasonality | (52/1) | (52/1) | (12/1) | (52/1) | (12/1) | (12/1) | (52/1) | (52/1) | (12/1) | (12/1) |
| AR Order | 1 | 2 | 2 | 1 | 1 | 1 | 1 | 2 | 1 | 1 |
| **(b) Statistical Test Results** | | | | | | | | | | |
| JB p-value | 0.88 | 0.07 | 0.06 | 0.11 | 0.04 | 0.98 | 0.48 | 0.06 | 0.07 | 0.72 |
| Q p-value | 0.08 | 0.75 | 0.92 | 0.17 | 0.61 | 0.52 | 0.33 | 0.35 | 0.36 | 0.36 |
| H p-value | 0.19 | 0.38 | 0.38 | 0.64 | 0.24 | 0.12 | 0.58 | 0.44 | 0.50 | 0.52 |
| **(c) Forecast / Data Fit Metrics** | | | | | | | | | | |
| RMSE | 0.025 | 0.026 | 0.076 | 0.019 | 0.021 | 0.028 | 0.027 | 0.028 | 0.029 | 0.033 |
| Variance of Residuals | 0.010 | 0.000 | 0.003 | 0.000 | 0.000 | 0.001 | 0.001 | 0.000 | 0.000 | 0.000 |

Table 4.2: Combined summary of model components, statistical test results, and forecast performance metrics for temperature, precipitation, and soil moisture time series across all study sites. JB, Q, and H refer to Jarque–Bera, Ljung–Box, and heteroscedasticity test p-values. Seasonality entries (e.g., 12/1, 52/1 and 365/1) indicate the period and harmonic structure, corresponding to monthly, weekly or daily data.

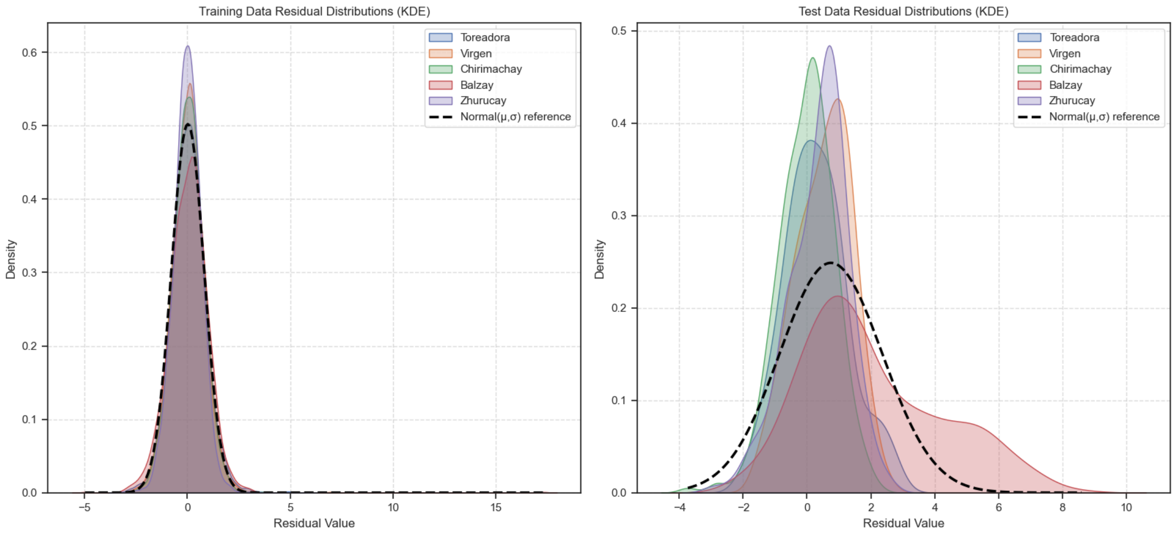

(a) Temperature residuals overview for the Zhurucay station and all stations in the Quinuas catchment.

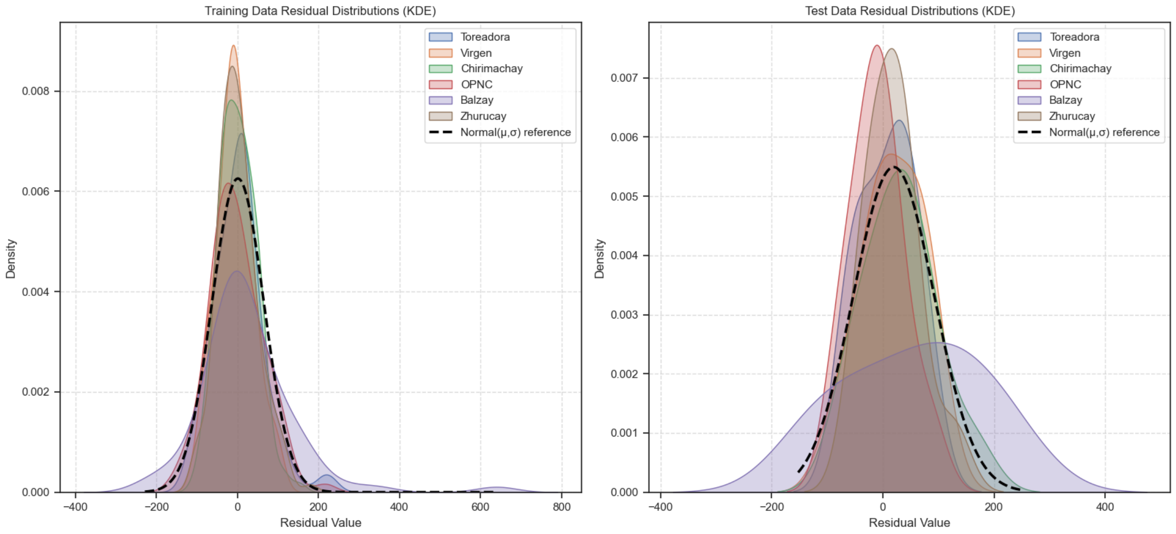

(b) Precipitation residuals overview for the Zhurucay station and all stations in the Quinuas catchment.

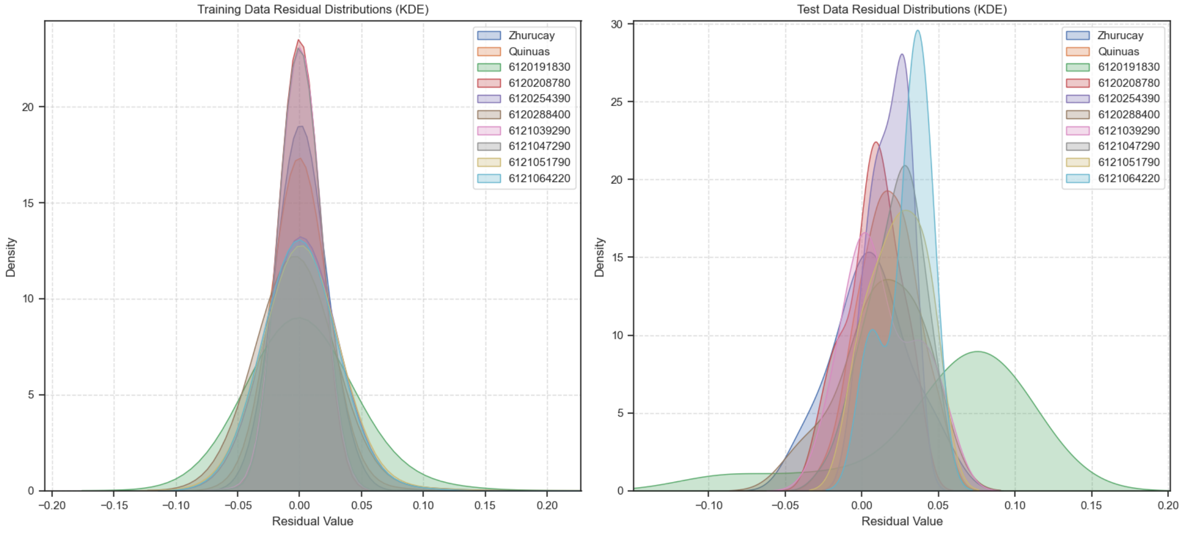

(c) Soil moisture residuals overview for the Zhurucay and Quinuas catchments and other catchments specified in Chapter 2.

Figure 4.2: Overview of the residuals in the training and test datasets for temperature, precipitation, and soil moisture across the Zhurucay and Quinuas catchments.

The model components show which processes have significant influence on the model. It should be noted here that the components do not necessarily have to reflect the conclusions of the trend analysis as performed by the Mann-Kendal tests. This behavior is related to the fact that the UCM includes dynamic components that can vary over time. As a result, a small trend can be absorbed by the stochastic variation in the seasonal frequency or by the autoregressive component. Examining the model components, the UCM fitted to the temperature data includes two harmonics, indicating that there is more than one dominant seasonal frequency per year. This is consistent with figure 4.3, where the temperature observations (both training and test data) exhibit a main cycle of approximately eight months with an amplitude of around 6° C, along with a smaller oscillation superimposed on that cycle.

As the model wont exactly be able to produce the same fitted values as the actual observations residuals will arise. Ideally, the residuals of the training and test data will follow a normal distribution, resembling the white noise present in the data. This is especially important for the training data as this means that the model is fully captured by the model components. Figure 4.2 contains an overview of all the residuals produced by the UCM.
Starting with the UCM applied to the temperature data (Figure 4.2a), the residuals of the training dataset closely follow a normal distribution, indicating a good model fit. In contrast, the residuals of the test dataset show a larger deviation from normality. This deviation mainly arises because the forecast cannot fully account for the autoregressive components. The autoregression component does however determine the spread of the 95% confidence interval. The key aspect to note is that the residual distribution peaks around zero, suggesting that the model provides a reasonably good fit to the observed data.
The same observations can be made for precipitation and soil moisture models. What is positive is that the variance of the training and test data seem to have the same variance; the distributions of both datasets seem to drop to a density of zero around the same values. It should be noted that the resampling of the soil moisture data varies between weekly and monthly mean as can be seen in table 4.2. This results less residual values for the monthly data, with a higher peak density around 0.

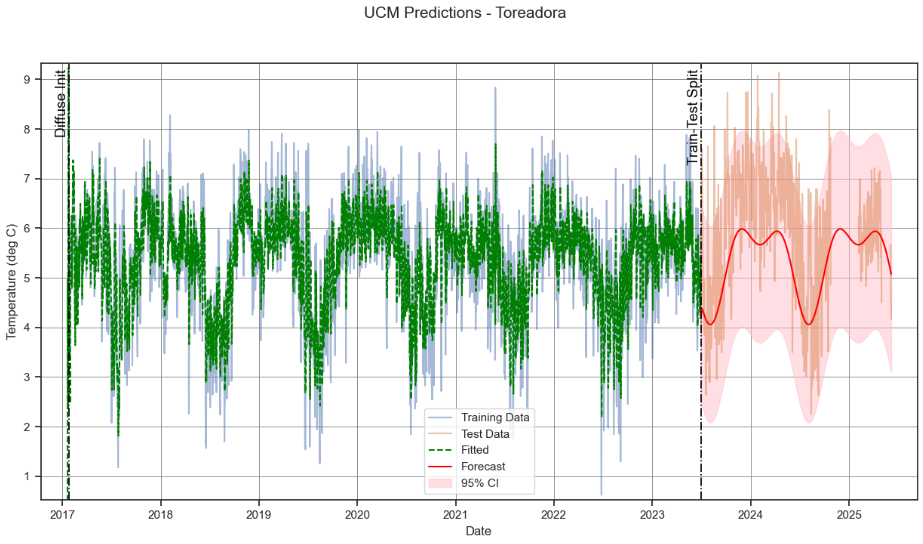

Figure 4.3: UCM model fit and forecast on the temperature data from the Toreadora station. The boundary between the fit and forecast is indicated after which the mean prediction (red line) is displayed including a 95% confidence interval which is based on the autoregression component.

Figure 4.3 presents the temperature forecast for the data collected at the Toreadora station. The fit–forecast boundary for this station was set to 30 June 2023, which is indicated in the plot as the "Train–Test Split." One of the most notable findings is that the UCM forecasts for all stations exhibit considerable error during the period from July 2023 to June 2024. This pattern is evident in Figure 4.3 as well as in Figures B.1 and B.2 in Appendix B. Consequently, the results of the trend analysis should be interpreted with caution, as this anomalous period may have introduced bias into the test results.

## 4.4. Complementary Páramo watersheds

The Quinuas and Zhurucay observatories represent only a small fraction of Ecuador's diverse Páramo region. Consequently, it is valuable to explore whether similar trends can be observed across other watersheds in the country. Section 2.2 details the data acquisition process for these watersheds.

Although the watersheds are highly diverse, making a simple classification impossible, several distinctions were made based on multiple criteria. Figure 4.4 illustrates the temporal evolution of land cover changes. In general, land cover types remained relatively stable over time, though a slight increase in the fraction of "Tussock Grasses" was observed in some watersheds over the past 40 years. A notable exception is the abrupt and significant land cover shift in 2023, compared to 2022. This could be attributed to the extreme anomalies of that year as described in this chapter or to satellite misclassification. However, as 2023 is the final year of available land cover data from the Mapbiomas dataset, it is difficult to definitively determine the cause of this change (MapBiomas Ecuador Project, 2023).

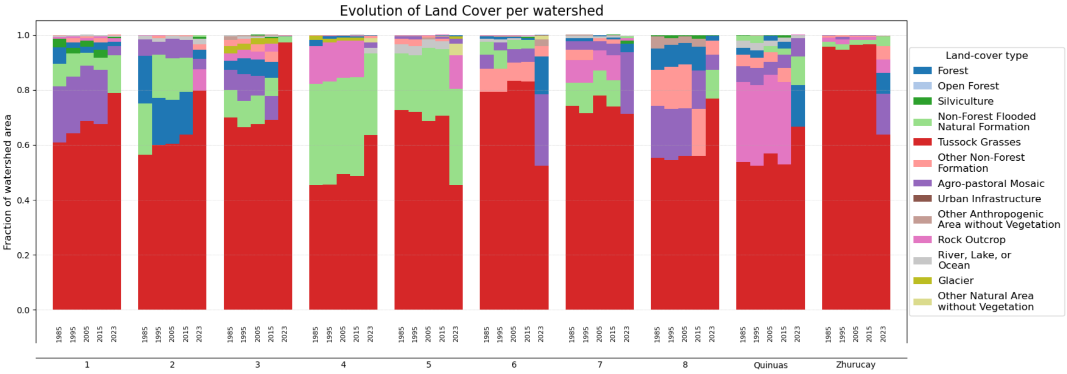

Figure 4.4: Stacked, grouped bar chart of the evolution of land cover for each watershed. Each individual bar represents a different year. Data acquired from MapBiomas Ecuador Project, 2023.

Using the same methodology described earlier in this chapter, the seasonal Mann-Kendall (MK) test was applied, and the slope was calculated based on soil moisture (SM) data generated by the satellite model for each watershed. The results of these analyses are summarized in Figure 4.5. The seasonal MK slopes are compared against three key watershed characteristics: mean elevation, latitudinal distance from the northernmost watershed, and the fraction of land cover occupied by "Tussock Grasses."

The latitudinal distance was determined using the centroids of the watersheds, which were extracted from Google Earth Engine. The location in the Andes (west, east or central) was determined based on the Andes chains as described in Chapter 1. The fraction of "Tussock Grasses" was obtained from MapBiomas. The LC-values corresponding to 2015 were used, due to the uncertainty described in the previous section. Fraction of "Tussock Grasses" provide valuable insights into the watershed characteristics, as this land cover type is prevalent in Páramo regions. Understanding how different proportions of "Tussock Grasses" respond to variations in SM is crucial, as it likely has a significant impact on regional water balance.

Interpreting these results, however, is challenging due to the high variability among the watersheds, combined with the limitations of the SM model when applied to such diverse regions (see Chapter 9). Furthermore, no clear correlation was found between the MK slope and any of the watershed characteristics. As a result, no further analysis of these figures was conducted to avoid presenting misleading patterns. Nevertheless, comparing different watersheds could offer valuable insights into the dynamics of Páramo ecosystems and how they might respond to various environmental drivers.

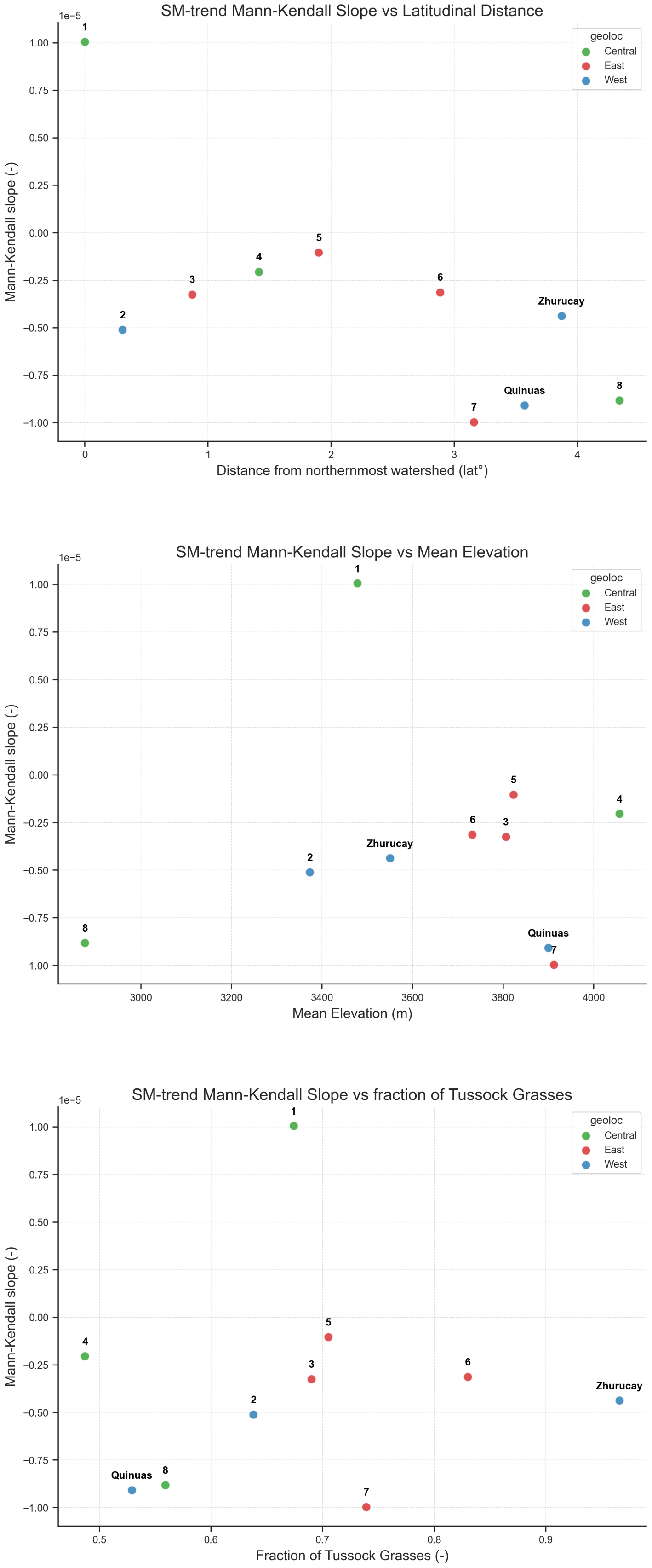

Figure 4.5: Seasonal Mann–Kendall slope per watershed, against (a) latitudinal distance from northernmost watershed, (b) mean watershed elevation, and (c) fraction of ”Tussock Grasses”.

# 5

# Landslides

The following chapter investigates the relation between landslides and observed hydrological trends. The chapter is structured with an introduction, literature study, a methodology and finally with results.

## 5.1. Introduction

Among these hazards, this report focuses on a frequently occurring one which are landslides. There is an observed correlation between climate changes and an increase in landslides across the globe (Seneviratne et al., 2012). Increasing temperatures, contributing to thawing of permafrost, and more extreme weather events, like longer rainfalls, result in more run-off water triggering landslides. According to Haque et al (Haque et al., 2019) report, in the period of 1995 to 2014 a significant global rise in deadly landslides and hotspots was observed linked to global climate change. Climate change caused more extreme weather patterns triggering more landslide incidents. In the 20 analysed years a total of 3876 landslides took place worldwide resulting in 163,658 deaths. In the 2023 IAIA (International Association of Impact Assessment) conference an economic loss of $ 20 billion annually was determined and presented (Sim et al., 2023).

This slope stability investigation will focus on landslides in the Quinuas observatory, located in Cajas in the Andes west of Cuenca, through which a vital transport artery runs from Cuenca to Guayaquil. There are no available online records of the number of landslides on this road each year; however, landslides occur multiple times annually and can close the road for periods ranging from a few hours to several weeks or even months. When closures happen, all traffic between the two largest southern cities is diverted to the southern road, leading to severe congestion and significant disruption.

Using meteorological data collected since 2012, together with records of past landslides, the Limburg Soil Erosion Model (LISEM), developed at the University of Twente, is utilised to predict slope failures along this road. By simulating rainfall events with different return periods, sections of the corridor that are most prone to landslide risk can be identified. The availability of detailed and accurate measurements makes this setting particularly suitable for the development of robust predictive models.

Against this background, the chapter addresses the following questions:

- What are the slope stability scenarios in the Páramo region of Cuenca, considering long-term hydrological trends?
- What further research and information would be needed for increasing the accuracy of a landslide hazard assessment system in the Azuay province?

## 5.2. Literature study

### 5.2.1. Landslide susceptibility

The Quinuas catchment is located in the province of Azuay, a province in Ecuador highly susceptible to landslides. The mountainous Andes that goes through the province, combined with the presence of vital transport arteries between major cities, means that landslides not only occur frequently but also carry significant socio-economic consequences. The United Nations office for Disaster Risk Reduction (UNDRR) has seen a drastic increase in the amount of landslides in Azuay from 1 in 1974 to 77 in 2023 (UNDRR and DesInventar, n.d.). This increase could partially be due to a better registry of events, however, the number of registered landslides in Azuay increased from 2011 to 2021 from 29 to 81, indicating that the number of events is also increasing.

In the year 2022 a large and deadly landslide occurred just outside the Quinuas observatory. On 27-03-2022, on the road Cuenca-Molleturo, a landslide of 7,000 cubic metres came down on a populated part of the road resulting in 4 deaths (Tapia, 2022). Not only the damage was devastating, but also the economic damage was significant. All traffic to the west had to be re-routed for two weeks through the roads in the south and north.

The susceptibility of landslides are closely linked to the properties of the Andean soils and the slopes. The region is primarily composed of Histic Andosols, which are volcanic ash-derived with high organic matter and high porosity (Buytaert et al., 2005). During intense rainfall the soil can become oversaturated, leading to a reduction in shear strength and slope stability. Additionally, deforestation for agriculture, urban development, and infrastructure expansion further increases slope instability by removing root structures that provide mechanical reinforcement and by enhancing surface run off (Sharma and Ram, 2014). As a result, slopes have become prone to higher risks of landslides.

Understanding the serious threat landslides pose to lives and the economy, the Ecuadorian government has taken steps to reduce risks and occurrences of landslides. Different measures have been taken. From physical changes to the slopes surrounding roads to national digital warning systems for potential hazards. As of late the government has published a map showing the risk of a potential landslide depending on the region shown in Figure 5.1 below.

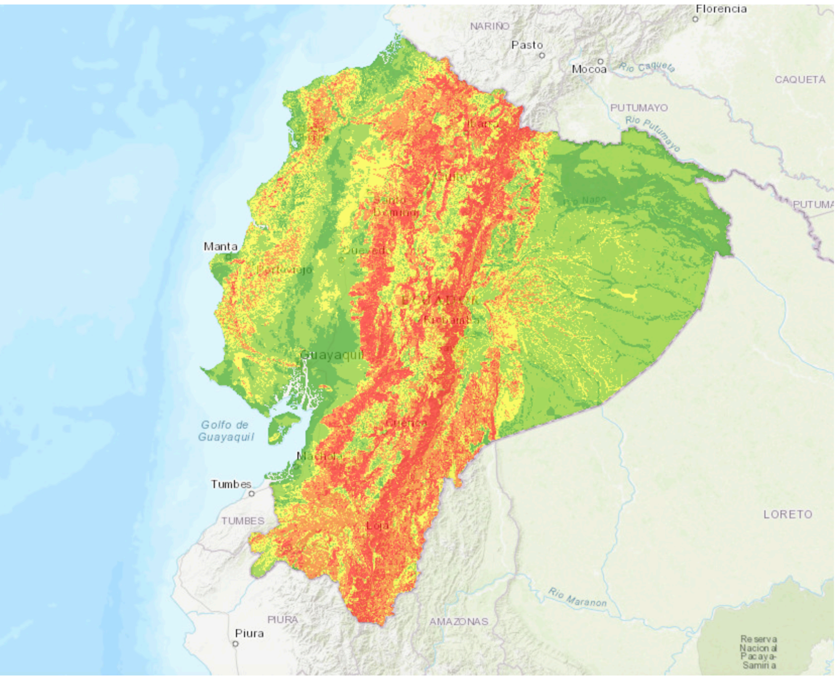

Figure 5.1: National landslide risk. Source: Ministerio de Energía y Recursos No Renovables / GeoEnergía (2025) (Ministerio de Energía y Recursos No Renovables, 2025).

Figure 5.1 depicts a static susceptibility layer derived from slope, lithology, relief, vegetation and hydrology. It functions to warn of potential risk, but is not able to determine under what conditions a landslide may occur or how the risk changes depending on precipitation. The application of LISEM could be a step forward in creating a more dynamic method to determine risk of landslides.

### 5.2.2. Types of landslides

Before making a dynamic model it is important to understand the theory behind landslides. Landslide is a term describing the downslope movement of soil, rock, and organic materials under the effects of gravity and also the landform that results from such movement. Different terms may be used to describe landslides such as: movements of mass or slope failure, but all come down to the same event. According to (Highland and Bobrowsky, 2008) there are 11 different types of landslides. These different landslides have been summarised by Varnes shown in the following Figure 5.2 below.

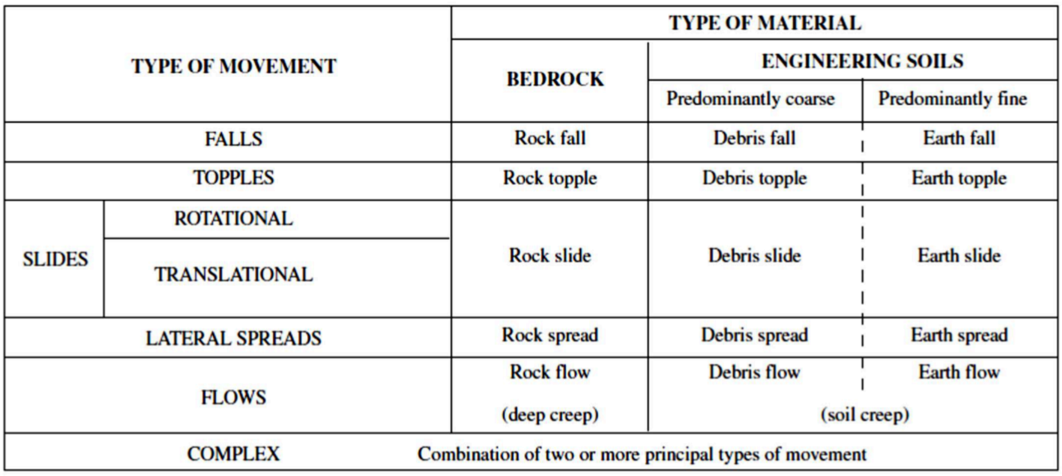

| TYPE OF MOVEMENT | | TYPE OF MATERIAL | | |
|---|---|---|---|---|
| | | BEDROCK | ENGINEERING SOILS | |
| | | | Predominantly coarse | Predominantly fine |
| FALLS | | Rock fall | Debris fall | Earth fall |
| TOPPLES | | Rock topple | Debris topple | Earth topple |
| SLIDES | ROTATIONAL<br>TRANSLATIONAL | Rock slide | Debris slide | Earth slide |
| LATERAL SPREADS | | Rock spread | Debris spread | Earth spread |
| FLOWS | | Rock flow<br>(deep creep) | Debris flow<br>(soil creep) | Earth flow |
| COMPLEX | | Combination of two or more principal types of movement | | |

Figure 5.2: Classification slope movements (Varnes, 1978)

Due to the soft soil in the Andes the most recurring landslides are the translational landslide and the rotational landslides depicted in Figure 5.3 below. These landslides are also the most typical worldwide and vary in speeds. They can be very sudden or slow in occurring. These landslides are mainly initiated due to hydrological changes. These consist of intense rainfalls, surface water table changes, increase in the water table and molten ice run-off. The landslide can also be initiated by earthquakes but are less common. Due to the characteristics and recurrence of landslides in Azuay, along with the availability of extensive hydro-meteorological data, makes this region highly suitable for detailed analysis. The presence of continuous observations of the hydrological cycle, together with the time series analysis conducted in this study, provides a solid foundation for the analysis of slope stability in the region.

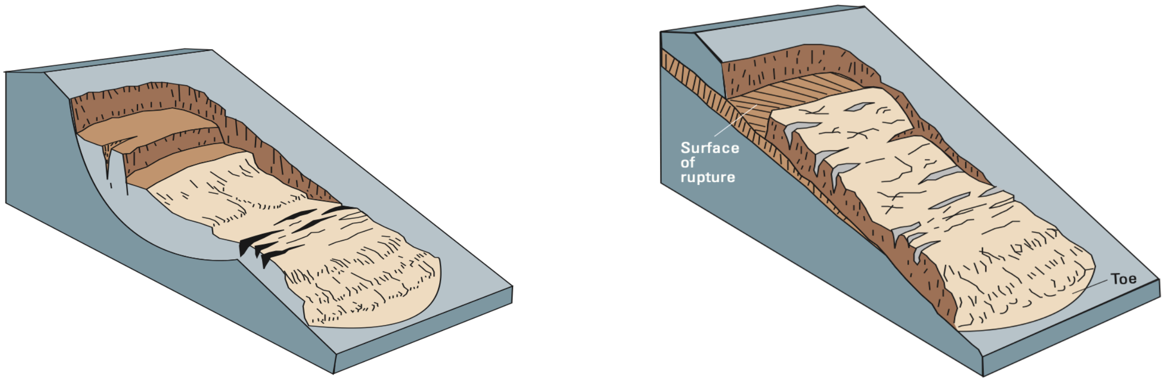

(a) Rotational landslide

(b) Translational landslide

Figure 5.3: Examples of rotational and translational landslides. Source: (Highland and Bobrowsky, 2008)

### 5.2.3. Landslide failure mechanisms

Landslide occur due to the following four mechanics listed below:

- Effective stress reduction from rainfall infiltration
- Loss of cohesion in unsaturated soils
- Hydraulic-gradient forces parallel to slope
- Debris-flow mobilisation

The first landslide mechanism is the reduction of effective stress as a result of increasing pore pressure. This is one of the primary failure mechanisms for shallow landslides in steep terrain. Rainfall infiltrating the soil leads to an increase in pore pressure (u) in the subsurface, resulting in a reduction of effective stress according to Terzaghi's principle of effective stress, which states that the effective stress equals the total stress minus the pore pressure (Terzaghi, 1943). This reduction in effective stress leads to a reduction in shear stress according to another formula of Terzaghi which he called the Coulomb's Equation. Both equations are shown respectively in Eq.5.1 and Eq. 5.2

$$\sigma' = \sigma - u \tag{5.1}$$

Where $\sigma'$ is the effective stress, $\sigma$ is the total stress, and $u$ is the pore water pressure.

$$\tau = \sigma' \tan(\phi') + c' \tag{5.2}$$

Where $\tau$ is the shear strength, $\sigma'$ is the effective normal stress, $\phi'$ is the effective angle of internal friction, and $c'$ is the effective cohesion.

A decrease in the effective stress also results in the reduction of shear strength; thus, an increase in rainfall infiltration leads to increased pore pressure resulting in weaker soil and a greater chance of soil failure. Iverson (Iverson, 2000) demonstrated that transient pore-pressure pulses, generated by rainfall infiltration governed by a simplified form of Richards' equation, play a dominant role in triggering shallow slides. These pressure transients, rather than steady groundwater levels, determine both the timing and depth of failure.

The second failure mechanism involves the reduction of apparent cohesion as soil becomes increasingly saturated. In unsaturated conditions, negative pore-water pressures act as a binding force between soil particles, giving the soil additional shear strength (Fredlund, 2019). As rainfall infiltrates, this suction decreases, leading to a loss of apparent cohesion. Lu and Godt (Lu and Godt, 2012) emphasise that this reduction in suction during wetting is a key driver of rainfall-induced slope failures in unsaturated soils.

During extended dry periods, soils can develop higher suction, temporarily increasing their shear strength. However, when intense or prolonged rainfall follows, the rapid wetting of these dry soils causes a sharp drop in suction, resulting in a sudden reduction of shear strength. This sudden transition from a stronger unsaturated state to a weaker saturated one can trigger slope failure.

The third failure mechanism is related to infiltration developing driving forces parallel to the slope surface. As rainfall infiltrates and groundwater flow develops downslope, the hydraulic gradient generates seepage forces that act in the same direction as gravity (Iverson, 2000). These forces effectively increase the driving stress on potential slip surfaces while simultaneously raising the pore-water pressure within the slope (mechanism 1). This mechanism is explicitly represented in transient rainfall–infiltration models such as LISEM, which calculates the hydraulic head distribution within the soil to estimate the time-varying balance between resisting and driving forces during rainfall events.

The fourth failure mechanism focuses on the transformation of a failed soil mass into a debris flow once saturation and mobility conditions are met. Under highly saturated conditions, part of the mobilised material may transition into a flow like state, where inter granular contact is replaced by fluid motion. This marks a relation between shallow landslides and debris flows, as described by Iverson (Iverson, 2000, Iverson, 1997). The degree of saturation, sediment composition, and slope gradient determine whether the material behaves as a slow moving slide or a rapid debris flow.

Whether a slope will fail depends on the balance between resisting and driving stresses, both influenced by the failure mechanisms discussed above. In a slope, several forces act simultaneously, as simplified in Figure 5.4. These include the resisting force, representing the shear strength of the soil; the normal force, which acts as the reaction force to the soil's weight; the weight of the soil mass itself; and the driving force, which is the downslope component of that weight.

As illustrated in Figure 5.4, slope a has a gentler inclination than slope b, resulting in a smaller driving force. The previously described failure mechanisms can either increase the driving force, by adding weight through water infiltration, or decrease the resisting force—by reducing the soil's shear strength. When the driving force exceeds the resisting force, the slope loses stability, and a landslide occurs.

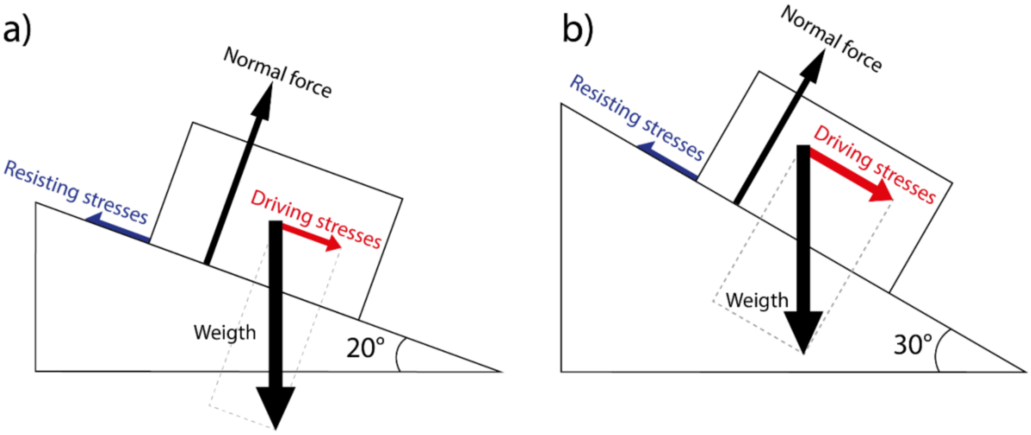

Figure 5.4: Forces acting on slope (de Vugt, 2018)

### 5.2.4. LISEM incorporation of failure mechanisms

LISEM simulates rainfall-induced landslides by combining hydrological and slope stability processes within a physically based and fully dynamic framework. It models infiltration, run-off, subsurface flow, and slope failure, allowing both the beginning and following motion of mass to be represented.

The first failure mechanism, in which an increase in pore pressure reduces the effective stress, is implemented in LISEM through the infinite slope stability model (Skempton and DeLory, 1957). The factor of safety is continuously updated for each grid cell based on the net balance between driving and resisting forces. Pore-water pressure is determined from rainfall infiltration using a simplified form of Richards' equation, which are the transient pressure pulses of Iverson (Iverson, 2000). When the factor of safety falls below one, failure is triggered, and the affected soil might start displacing.

The second mechanism, the loss of apparent cohesion as the soil becomes increasingly saturated, is represented in LISEM through its unsaturated soil formulation. The model uses the van Genuchten–Mualem soil water retention relationship to link soil suction to water content (van Genuchten, 1980, Mualem, 1976). As rainfall infiltration reduces suction, the apparent cohesion decreases, resulting in a lower shear strength and therefore a reduced factor of safety. This allows LISEM to mimic the progressive wetting and weakening of the upper soils in which stability fluctuates due to changes in suction.

The third failure mechanism, concerning hydraulic gradients and seepage forces, is represented in LISEM through the dynamic interaction between infiltration, soil moisture, and the infinite-slope stability computation. Rainfall infiltration changes local soil water content and pore pressure, which are updated at each time step by the hydrological module (de Roo et al., 2018). As a result it changes the effective stress and the total soil weight, thereby altering the balance between driving and resisting forces on the slope. Although the model does not explicitly calculate seepage force vectors between grid cells, it accounts for their effect indirectly: subsurface forcing and variations in hydraulic loading reduce the factor of safety and change the stable depth of the soil column.

As last the fourth mechanism, the debris flow mobilisation, is determined through a two phase run out flow combining water and solid dynamics developed by Pudasaini (Pudasaini, 2012). Using this method the interaction between landslides, water flow and debris flow can be determined. This set of two phase equations contains a physically based two phase momentum balance (de Roo et al., 2018). This not only incorporates pressure and gravitational acceleration but also non-Newtonian stress terms, a two phase drag component and a Mohr-Coulomb friction force for the solid phase. For LISEM to be able to model flows from clear water to hyper concentrated debris flow the frictional resistance in the water has been replaced by the Darcy Weisbach equation to represent hydraulic roughness more realistically. Forces can now be adjusted according to the local sediment concentration and flow state. Other properties like the viscosity are empirically estimated following O'brien and Julien (O'Brien and Julien, 1988), calibrated to conditions with more sediment.

By integrating these four mechanisms into a single framework, LISEM connects the hydrological and mechanical aspects of slope failure. Providing a realistic representation of how rainfall triggers landslides and debris flows through time-dependent interactions between infiltration, pore pressure, suction, and slope geometry.

## 5.3. LISEM multi-hazard modelling methodology

LISEM is a geospatial modelling tool developed by V. Jetten and B. van den Bout, which can simultaneously model multiple hazards. Since its development in 1994, it has been used in many studies on landslides and soil erosion (Jetten and Van den Bout, 2018). It is able to combine rainfall data, soil properties and hydrology, which makes it a suitable tool to assess slope stability scenarios within the Quinuas catchment. The software has been proven to work for similar landslide studies in other regions, such as on the island of St Eustasius (de Vugt, 2018) and in central Norway (Awgechew, 2022), however, in both cases calibration based on past landslide events and field observations was required to improve its accuracy.

The LISEM software uses a numerical model, which is based on many theoretical equations that describe the behaviour of various natural phenomena. The continuous version of these equations is elaborated on in this subsection. The physical phenomena that are incorporated into this LISEM model can be divided into hydrological processes and slope processes.

### 5.3.1. Hydrological processes

Various hydrological processes are incorporated in the LISEM software. One is rainfall data based on collected rainfall intensity, provided as an input file. Then, the software spreads it over the cells based on cell size, corrected for slope (de Roo et al., 2018). Another process is interception. This includes all rainwater that does not enter the soil directly but is hindered by vegetables, buildings or other surface covers (Simmonds and Linsley, 1982. For interception, a formula by Aston (1979) is used:

$$I_c = S_{max}(1 - e^{-k\frac{Ptot}{S_{max}}}) \tag{5.3}$$

Where $I_c$ is the interception level in mm,
$S_{max}$ is maximum canopy storage in mm,
$P_{tot}$ is the total precipitation in mm
and k is a constant based on leaf area index (LAI).

More details on how the canopy storage is calculated can be found in section 5.4.3. Next to canopy storage, there is also Micro Depression Storage (MDS), for which the following equation was established by Kamphorst et al. (2000):

$$MDS = 0.243RR + 0.010RR^2 + 0.012RR \cdot S \tag{5.4}$$

Where MDS is in meters,
S is the slope in m/m
and RR is the standard deviation of the surface heights in mm.

Infiltration is modelled with Darcy's equation for a vertical soil water balance:

$$\frac{\delta\theta}{\delta t} = -K_s \frac{\delta h}{\delta z} \tag{5.5}$$

Where $\theta$ is the soil moisture content (-),
h is the hydraulic head (m),
z is the vertical elevation (m)
and $K_s$ is the hydraulic conductivity (m/s)

Evaporation and transpiration are processes that are neglected in this model, because they are of time scales larger than that of a landslide. Some other processes that are taken into account are groundwater flow and surface flow.

### 5.3.2. Slope processes

Slope stability assessment in the LISEM software is based on the infinite slope model, as described by (de Roo et al., 2018). In this model, the factor of safety is given by equation 5.6. This equation solely depends on local properties.

$$FoS = \frac{c' + w_b \cdot \cos(\beta)^2 \cdot \tan(\phi)}{w \cdot \sin(\beta) \cdot \cos(\beta)} \tag{5.6}$$

Where $c'$ is the effective cohesive soil strength (kPa), defined in equation 5.7,
$w_b$ is the weight of the bedrock (N),
$w$ is the weight of the soil (N), defined in equation 5.8,
and $\beta$, defined in 5.9.

$$c' = c + c_{veg} + \psi \tag{5.7}$$

Where $c$ is soil cohesive strength (kPa),
$c_{veg}$ is the cohesion caused by plant roots (kPa)
and $\psi$ is the soil water potential (kPa).

$$w = g \cdot h \cdot (\gamma \cdot (1 - \theta) + \gamma_s \cdot \theta) \tag{5.8}$$

Where $g (\approx 9.8)$ is gravitational acceleration $(m/s^2)$,
$\theta$ is effective soil saturation (-),
$\gamma$ is dry soil density $(kg/m^3)$
and $\gamma_s$ is saturated soil density $(kg/m^3)$.

$$\beta = atan(\frac{max(h_{h_{x-1}-h_x}, h_x - h_{x+1})}{dx}) \tag{5.9}$$

Formula 5.9 describes the maximum slope of a cell with one of its neighbouring cells. When calculating the failure depth, the same equation (5.6) can be used, but rewritten to isolate the soil depth. Assuming a FoS of 1 results in an equation that can be solved with the trigonometric identities (de Roo et al., 2018). Upslope iterations are then repeated until a cell is reached where failure does not occur. The sum of failure depths for each cell can be used to obtain a total failure volume.

## 5.4. Model input

The input that the software requires to model slope stability scenarios can be divided into two categories: rainfall data and maps.

**Rainfall data**

For rainfall input, synthetic data was developed based on various return periods, which were obtained from the available data at the Quinuas catchment. Refer to section 2.5 for the methods to generate this synthetic data. For the results, dummy precipitation data based on return periods of 1, 5 and 10 years was used. An overview of rainfall distribution for the synthetic storms can be found in appendix C.

#### Spatial data

The required input maps are described in further detail in this section, together with a description of the source or calculation methods. Further processing of the maps included masking them to the correct area, converting them to the required units, matching the resolution and eliminating faulty pixel values. Table 5.1 provides an overview of the necessary maps, their source and their resolution.

| Mapped parameter | Unit | Source |
|---|---|---|
| Digital elevation model (DEM) | m | Copernicus Satellite data |
| Land cover classification (LCC) | - | Mapbiomas |
| Manning's n coefficient | $s/m^{1/3}$ | From LCC |
| Building cover | frac | From LCC |
| Road width | m | neglected |
| Vegetation height | m | From LCC |
| Vegetation cover | frac | From LCC |
| SMAX surface | m | From Sentinel-2 data |
| SMAX canopy | m | From Sentinel-2 data |
| Clay | frac | Soilgrids |
| Sand | frac | Soilgrids |
| Gravel | $m^3/m^2$ | Soilgrids |
| Organic matter | $kg/m^2$ | Buytaert et al., 2005 |
| Density | $kg/m^3$ | Buytaert et al., 2005 |
| Soil depth | m | From DEM |
| Groundwater height | m | From DEM |
| Theta initial | frac | From Sentinel-2 data |
| Cohesion top | Pa | Buytaert et al., 2005 |
| Cohesion channel | Pa | Neglected |
| Internal friction angle | Rad | From soil type |
| Cohesion bottom | Pa | Based on 'Dominica' dataset |
| Density bottom | $kg/m^3$ | Carmichael, 1984 |
| Rock size | m | Based on 'Dominica' dataset |

Table 5.1: Collection of map data to use in LISEM model

### 5.4.1. Maps based on DEM and LCC

As mentioned in section 2.4, the LCC and DEM maps are public, both of which have a resolution of 30m. These are considered base maps, as various other maps can be developed based on this data. Table 5.1 depicts which of the required input maps of the LISEM model are based on these base maps.

#### DEM derivatives

To get a better understanding of the research area, the DEM was used to visualise the slope and aspect of the Quinuas catchment in QGIS, as can be seen in figure 5.5. For this, the DEM was first filled with a module of the SAGA plugin in QGIS: 'Fill sinks (Wang & Liu)'. Also, the assumption was made that the groundwater table is equal to the elevation. This is a very conservative assumption, but since a higher groundwater table means a higher landslide susceptibility (as effective stress and thus shearing resistance is reduced (Zhou, 2010)), it is safer to assume a higher water table. As there are only two measurements of groundwater height within this catchment, a more advanced spatial interpolation of this property was not possible. Finally, the DEM was used as a basis to develop a soil depth model, the methods of which are elaborately described in section 5.4.2.

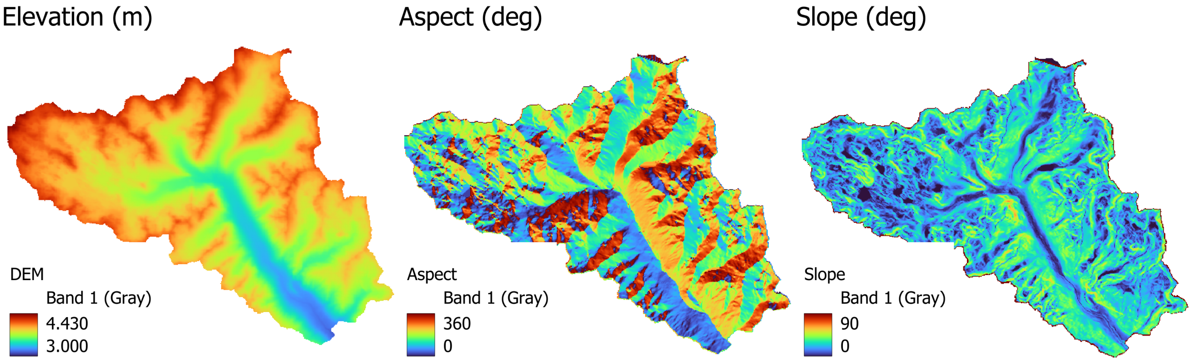

Figure 5.5: Digital elevation map (left) and two maps derived from it; aspect (middle) and slope (right)

### LCC derivatives

From the LCC,Figure 5.6, it can be seen that grasslands are dominant in the Quinuas catchment. They are tussock grasses (Calamagrostis sp. and Festuca sp.), which are responsible for (67.8%) of the land cover (Pesántez et al., 2018). Another share of the land, 12.7%, is covered with forests (Polylepis sp.). The rest of the vegetation in this area is good for 5.1% the land cover, and consists of a combination of pasture (Lolium sp.) and pine plantations (Pinus patula) (Pesántez et al., 2018). See figure 5.6 for images of this vegetation.

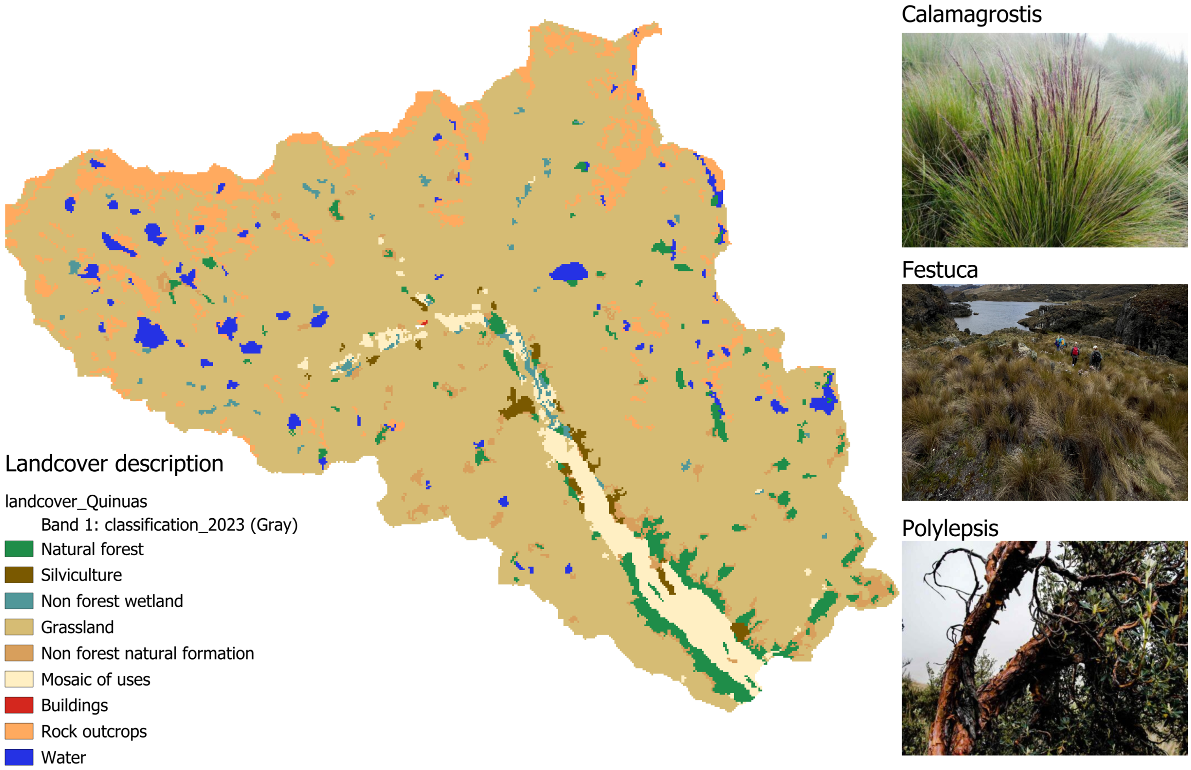

Figure 5.6: Land cover classes with photo's of the most dominant vegetation types (Land cover: MapBiomas Ecuador Project, 2023. Top & bottom photo: Ecuventure, 2018. Middle photo: Loes Vogelaar, 2025)

The first map derived from the LCC is the building cover map. This was done by assigning a value of 1 to the LCC band containing buildings and assigning a value of 0 to all other bands. The other maps derived from the LCC (Manning's n, vegetation height, and vegetation cover) are created by assigning characteristic values to the type of land cover. These are shown in Table 5.2. Manning's n coefficient was based on (Chow, 1959), and typical values for vegetation height and cover were based on appendix A of the LISEM manual (de Roo et al., 2018) in combination with field observations.

| Land cover class | Band | N ($s/m^{1/3}$) | Veg height (m) | Veg cover (frac) |
|---|---|---|---|---|
| Forest formation | 3 | 0.1 | 5 | 0.9 |
| Silviculture | 9 | 0.1 | 5 | 0.8 |
| Non forest wetland | 11 | 0.1 | 5 | 0.9 |
| Grassland | 12 | 0.1 | 0.2 | 1.0 |
| Non forest natural | 13 | 0.1 | 0.2 | 1.0 |
| Mosaic of farming uses | 21 | 0.1 | 3 | 0.9 |
| Antropic non vegetated | 25 | 0.01 | 0 | 0 |
| Rocky outcrop | 29 | 0.01 | 0 | 0 |
| Mining | 30 | 0.01 | 0 | 0 |
| River, lake, ocean | 33 | 0.05 | 0 | 0.9 |

Table 5.2: Parameters derived from land cover classes, based on (**Chow1959; LISEM_Manual_2018**)

### 5.4.2. Soil depth

Soil depth is one of the determining aspects of the landslide hazard model, as it directly influences the factor of safety and infiltration potential (de Roo et al., 2018). Therefore, assuming a uniform value throughout the whole research area does not suffice. Multiple methods have been described in literature to predict the spatial variability in soil depth. As described by (Tesfa et al., 2009), topographic properties of the area have a larger influence on the soil depth than land cover variables. (Saulnier et al., 1997) proposes a linear relationship between elevation and soil depth, based on known minimum and maximum soil depth, see eq. 5.10. (Molina et al., 2024) have described the soil in relation to vegetation of the nearby Cuevas catchment, which is of similar height and land cover as the Quinuas catchment. The heighest soil depth they describe is that under tussock grasses (65±19 cm). Thus, the maximum soil depth used in equation 5.10 is 85 centimetres.

$$m_i = m_{max} - \frac{m_{max} - m_{min}}{z_{max} - z_{min}}(z_i - z_{min}) \tag{5.10}$$

Where $g(\approx 9.8)$ is gravitational acceleration ($m/s^2$),
$\theta$ is effective soil saturation (-),
$\gamma$ is dry soil density ($kg/m^3$)
and $\gamma_s$ is saturated soil density ($kg/m^3$). Where $m_i$ is the calculated soil depth in a cell
$m_{max}$, the maximum soil depth, set to be 0.85m
$m_{min}$, the minimum soil depth, is set at 0m
$z_i$ is the elevation in a cell
$z_{max}$, the maximum elevation, is 4424m
$z_{min}$, the minimum elevation, is 3147m

The above described method is a first estimate for soil depth which incorporates spatial variability better rather than picking a constant uniform over the whole area. However, it neglects other processes that influence the soil depth. Erosion is likely to occur at higher altitudes and sediments accumulate near channels. Next to this, sediments are less likely to accumulate on high slopes. Finally, when the curvature is convex, soil is less likely to settle than on a concave slope as there is an inverse correlation between profile curvature and soil depth (Heimsath et al., 1997). Therefore, (Saulnier et al., 1997) have proposed the following equations for soil depth in relationship to channel distance, slope and curvature:

$$m_i = m_{max} - \frac{m_{max} - m_{min}}{s_{max} - s_{min}}(s_i - s_{min}) \tag{5.11}$$

$$m_i = m_{max} - \frac{m_{max} - m_{min}}{DC_{max} - DC_{min}}(DC_i - DC_{min}) \tag{5.12}$$

$$m_i = m_{max} - \frac{m_{max} - m_{min}}{c_{max} - c_{min}}(c_i - c_{min}) \tag{5.13}$$

Where s describes the slope in degrees,
DC the distance to a channel in meters
and c the curvature.

Once four soil depth maps were created based on equation 5.10 through 5.13, an interpolation was performed based on a subset of 250 random points of each of the maps, so 1000 in total. This was combined with known data. Unfortunately, no measurements of soil depths within the Quinuas catchment were available. However, one of the distinguished land covers in the LCC is bare rock which logically has a soil depth of zero meters. From these locations, 250 random points were selected as calibration points. Together with 1000 random points from the four other soil depth maps, a stochastic interpolation was applied to obtain the final prediction of the soil depth map. Block Regression Kriging (BRK) was chosen as an interpolation method, Kuriakose (Kuriakose et al., 2009) describes this as a suitable estimator for soil depth when very little data is available. Furthermore, Regression Kriging is suitable for datasets containing a regression trend. It takes into account the trend of the target variable, and applies Simple Kriging to the residuals of the regression (Hengl et al., 2007). The built-in module of the SAGA plugin in QGIS was used to perform this interpolation.

Figure 5.7 presents a visual comparison of the four linear single-parameter and the multi-parameter BRK soil depth maps for the Quinuas catchment.

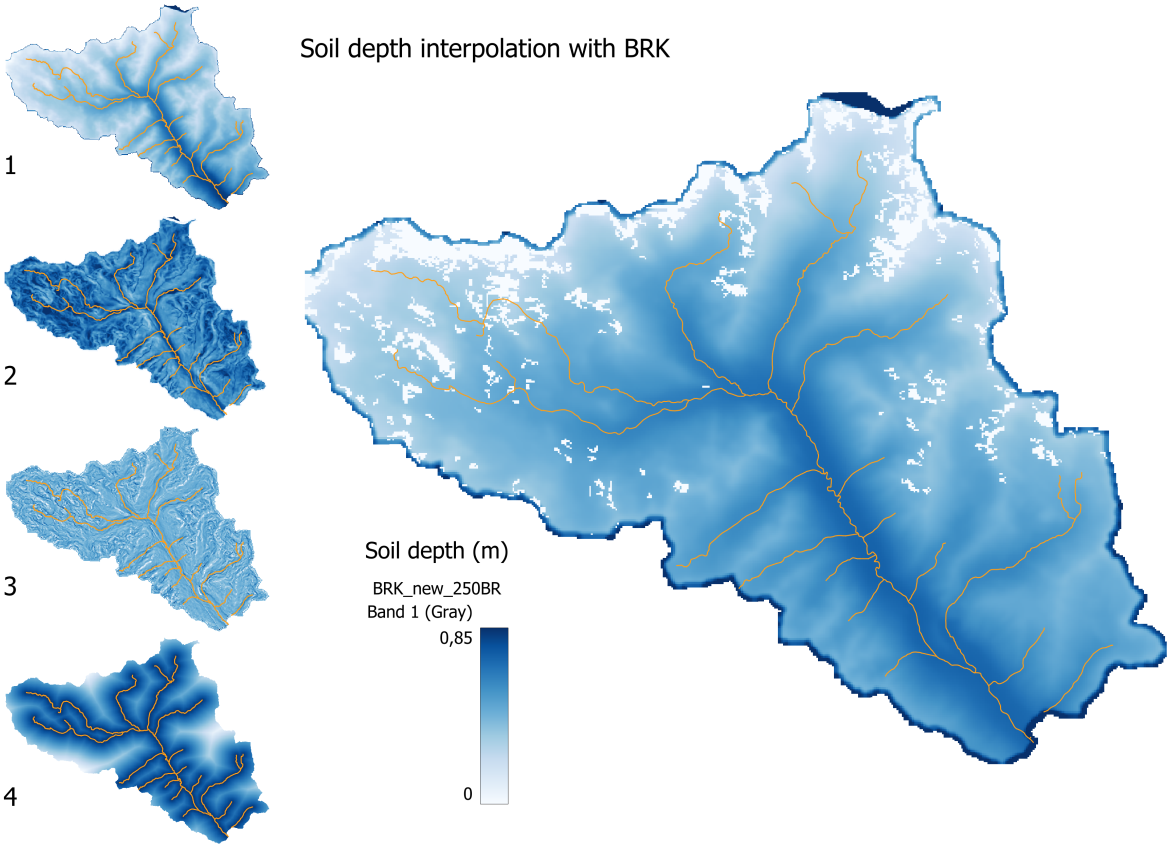

Figure 5.7: Results of linear soil depth distributions based on elevation (1), slope (2), curvature (3), channel distance (4) and resulting BRK interpolation (right) of the Quinuas catchment

### 5.4.3. Maximum water storage

Water storage (mm) plays an important role in the LISEM model, as it directly influences surface run off generation and slope stability. The Páramo ecosystem, with its characterised cushion plant vegetation and organic rich Andsols, is known for its exceptional capacity to retain water (Lazo et al., 2019). This capacity, however, varies considerably between land cover types, making accurate spatial mapping essential for realistic hydrological and slope stability modelling. This is done using the land cover classification shown in Figure 5.6 (2023), two distinct water storage maps were created: the Smax Canopy, representing the maximum interception storage of vegetation, and the Smax Surface, representing the surface storage in micro-depressions. Both layers are determined using the land-cover map as a base but rely on different supplementary parameters such as vegetation characteristics or surface roughness and slope. These maps are vital for the LISEM model, as interception, infiltration and run off can be determined during rainfall. The model is able to simulate hydrological response and the effects of land cover on slope stability better as it is able to determine the quantity at which rainwater is not stored and run off begins. The corresponding code for the water storage calculation can be found in landslide analysis folder **Github** (https://github.com/Matglassaa/Trend_analysis_Paramo).

The water storage due to the surface of flora is determined by calculating a maximum storage capacity. This maximum storage capacity is determined by using and equation developed by Von Hoyningen-Huene (von Hoyningen-Huene, 1981). This equation uses Leaf Area Index (LAI) parameters for each different vegetation. The vegetation categories in which the Quinuas has been described are: broadleaf, pine, bracken, grass and crop. As a result a map is created with Smax canopy values per pixel depending on the vegetation. The corresponding formulas are shown below.

$$S_{\text{max, broadleaf}} = 0.2856\,LAI \tag{5.14}$$

$$S_{\text{max, pine}} = 0.2331\,LAI \tag{5.15}$$

$$S_{\text{max, grass}} = 0.59\,LAI^{0.88} \tag{5.16}$$

$$S_{\text{max, bracken}} = 0.1713\,LAI \tag{5.17}$$

$$S_{\text{max, crop}} = 0.935 + 0.498\,LAI - 0.00575\,LAI^2 \tag{5.18}$$

The LAI values used per vegetation and the resulting Smax canopy value is shown in Table 5.3. The code for this calculation can be found in the landslide analysis folder **Github** (https://github.com/Matglassaa/Trend_analysis_Paramo).

The water storage in micro-depressions is also calculated in a similar way as the Smax canopy, however the LAI is replaced with the Random Roughness (RR) variable and also the Digital Elevation Map (DEM) parameters are applied. The DEM is important as the slope per pixel is computed. The storage is determined through the use of equations created by Onstad and Linden (Linden et al., 1988; Onstad, 1984). In the formula the RR stands for the Random Roughness and S stands for slope.

$$S_{\text{max, surface}} = 0.243\,RR \;+\; 0.010\,RR^2 \;+\; 0.012\,RR\,S \tag{5.19}$$

Each land cover type has a different RR parameter, determined from LISEM appendix A (de Roo et al., 2018), and each pixel has a designated slope value. The determined values are depicted in Table 5.3. The value for Smax surface for eacht land cover class is the average. This is because the slope is not constant for the land cover types.

### 5.4.4. Soil parameters

The soils in the Páramo system can be classified as Andosols, which are high in organic matter content and have a strong soil structure with a high water retention potential (Buytaert et al., 2005). Buytaert et al. (2005) describe an estimated value for the bulk density of this soil of $0.3 Mg/m^3$ and a range of organic carbon content of $100-400 g/kg$. Breakdown of volcanic ash deposits results in a high content of aluminium, iron and amorphous minerals.

The LISEM model requires an input map for clay, sand and gravel fractions. This is obtained from Soilgrids (ISRIC – World Soil Information, 2020), with a spatial resolution of 250m. The resolution is rather high with respect to the scale at which landslides occur, so further improvements can be made based on field measurements. However, for a global model this data suffices.

Furthermore, some additional soil information was required by the software. As little information was available from tests and literature, a uniform constant value was assumed for the initial soil moisture,

| **Land cover class** | **LAI** | **RR [cm]** | **Smax canopy [mm]** | **Smax surface [mm]** |
|---|---:|---:|---:|---:|
| Forest formation | 5.76 | 1 | 1.64 | 14.30 |
| Silviculture | 4.02 | 1 | 0.94 | 9.34 |
| Non forest wetland | 5.76 | 1 | 0.97 | 5.14 |
| Grassland | 34.51 | 0.5 | 13.31 | 9.86 |
| Non forest natural | 34.51 | 0.5 | 5.91 | 5.24 |
| Mosaic of farming uses | 5.76 | 1 | 3.61 | 11.51 |
| Antropic non vegetated | 0 | 0.5 | 0 | 4.36 |
| Rocky outcrop | 0 | 0.5 | 0 | 33.13 |
| Mining | 0 | 0.5 | 0 | 2.10 |
| River, lake, ocean | 5.76 | 0.1 | 0 | 1.11 |

Table 5.3: LAI and Smax parameters derived from land cover classes

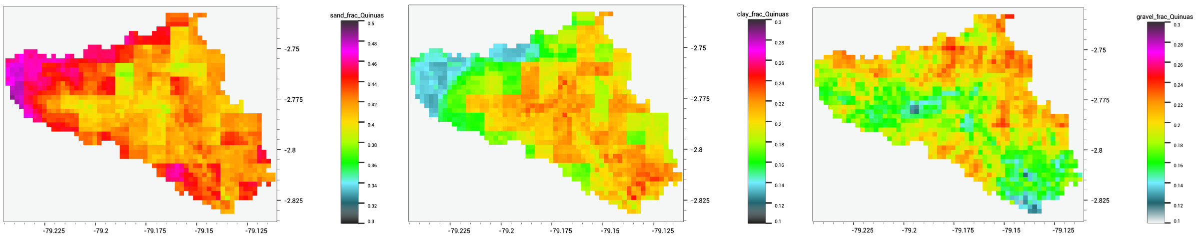

Figure 5.8: Quinuas catchment soil classification from Soilgrids (2020). Maps show fractions of sand (left), clay (middle) and gravel (right).

cohesion, density and rock size. The initial soil moisture was based on values from satellite data, see section 3.2.1. The chosen value was 0.6. For the rock size and bedrock cohesion, the example dataset of Dominica was used, available at the LISEM website ("Downloads — LISEM", 2022). Out of all locations for which datasets are available, the Dominica one was chosen because is a volcanic island in the Caribbean and he soil in our research area is also of volcanic origin. The value for the rock size parameter is 0.05 m. Finally, the cohesion and density of the bottom rock layer has to be obtained. The geological map in 1.4 shows many rhyolitic bedrocks, of which Carmichael (Carmichael, 1984) describes a mean density of 2.5 g/cm3.

## 5.5. Model results

Once the LISEM model starts running, many parameters can be visualised. For this research, the Factor of Safety is of most relevance. It is shown in figure 5.9. At a first glance, the model seems to differentiate well between slopes and soil thicknesses. Higher slopes have a lower Factor of Safety, and the area around the river has a low Factor of Safety. So spatially, the first steps in a hazard modelling system have been made. However, numerically, the values of the Factor of Safety seem very off. With the configuration of maps described in 5.4, factors of safety of between 0.8 and 1.2 were found. This would mean that part of the area is extremely prone to landslides, whilst none have happened thus far in this specific catchment. Manual alterations of the model show that changing bedrock the parameters unexpectedly influence the final Factor of Safety map. To get a better understanding of why this has such an effect, the mathematics behind the model should be analysed. The challenges of this are discussed in chapter 9.

## 5.6. Model refinement

As described in section 2.4, many of the input data is still based on assumptions and a uniform distribution throughout the whole catchment. To refine the model, these maps should be updated to have more representable values and accurately reflect their spatial variability. In order to do this, soil tests should be deducted at various locations in the catchment. From these tests, properties such as cohesion, internal friction angle and density can be deducted.

Specifically, for the soil depth map some relatively easy but accurate measurements can be done

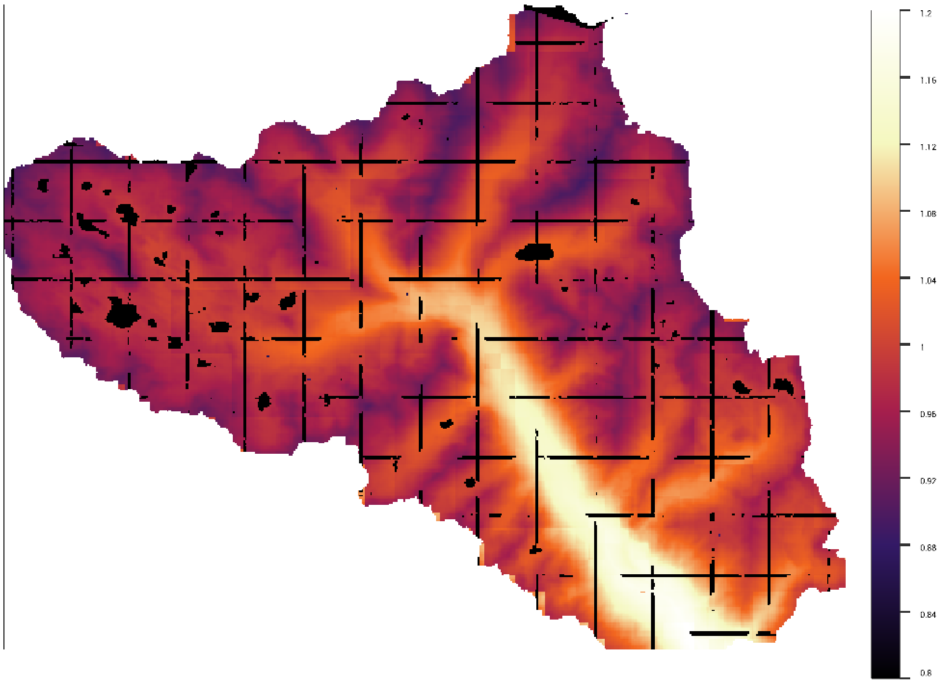

Figure 5.9: LISEM visualisation of Factor of Safety during 10y return period dummy storm

using a soil hydraulic sampler. Currently, the only real depth that is incorporated into the model is the zero depth at bare rock patches. However, when there is no or little soil there is also a lower chance of landslides. Thus, the most accurate parts of the soil depth model are the less relevant to the final landslide model. Random measurements of medium to large depth would improve the accuracy of the soil depth map.

Another refinement which functions as a LISEM input is the synthetic storm. As explained in section 2.5, the average 24 hour rainfall intensity of different returning periods is used to model the storm. A more accurate method would be to extract the exact rain intensities of such storms from the 12 year dataset. This takes more time and could therefore be refined to increase accuracy and create a more representative IDF curve.

Furthermore, the model should be calibrated with known occurrences of landslides. The methods described earlier in this chapter can be applied to other regions. Then, the parameters can be manually adjusted until they produce a result similar to the actual landslide event.

Finally, once the model produces accurate and reliable results, it can be updated even further by adding in extra functions of the LISEM software. Examples of this that might be relevant in this specific region are including infiltration, groundwater flow and a channel.

# 6

# Water quality

## 6.1. The Quimsacocha National Recreation Area

The Quimsacocha National Recreation Area is located in the Cuenca Canton in the Azuay Province of Ecuador. It covers 3217 hectares and is part of a large Páramo ecosystem of 18172 hectares. It is part of the collapsed caldera of the ancient Quimsacocha volcano, now a wetland area characterized by lakes, marshes and springs (Barros et al., 2024).

Since 2012 the Ecuadorian Ministry of Environment and the City of Cuenca have a coordination and action agreement to optimize the management, handling, control, and administration of the Quimsacocha National Recreation Area. This agreement aims to protect and preserve the diversity of the flora and fauna of this area (Ministry of the Environment and Transition, n.d.).

The area is of great importance due to its water reserve and wetland zone, being a crucial site for the conservation of natural resources and the water supply for the region. Quimsacocha is a hydrological divide feeding both the Amazone and the Pacific watersheds. The water sources that form the sub-watersheds of the Tarqui, Yanuncay and Rircay rivers originate here. The Tarqui and Yanuncay river belong to the Cuenca canton and drain to the Amazone. These rivers cross the city of Cuenca as well. The Rircay river belongs to the Girón canton and drains to the Pacific (Barros et al., 2024).

The potable water supply for the city of Cuenca depends on these Páramo-fed rivers. Over 661,000 inhabitants rely on this water source for domestic and industrial use. The Páramo ecosystem also provides habitat for diverse endemic species. According to the Constitution of Ecuador, the Páramo is fragile ecosystems that require special protection (Articles 406, 314, and 411) (República del Ecuador, 2017).

### 6.1.1. Groundwater Recharge In The Andean Páramo

In the Páramo, water circulates through a tightly connected surface–subsurface network. Rainfall infiltrates the upper soils, which consist mainly of Andosols on the slopes and Histosols in the wet valley bottoms. Rain-fed Histosols absorb and temporarily store water, while groundwater-fed Histosols receive additional inflow from deeper layers (Jerves et al., 2023).

Beneath the soils lies fractured volcanic bedrock full of faults and cracks that create preferential flow paths. Water rapidly percolates downwards through these fractures, recharging both shallow (2–15 m) and deep (20–231 m) groundwater reservoirs. During the rainy season, most recharge occurs through these pathways and water mixes vertically and laterally across depths (Jerves et al., 2023).

During the dry season, when rainfall is scarce, the deep groundwater and groundwater-fed Histosols slowly release stored water upwards towards springs and streams, maintaining a steady base flow. This dynamic exchange process enables the Páramo to act as a natural water regulator, capturing rain efficiently and sustaining rivers year-round, even during droughts (Jerves et al., 2023).

## 6.2. Mining

Even though it is a preserved area, Dundee Precious Metals (DPM) acquired the Loma Larga gold project in 2021. A 16 year underground mining project, of which 4 years of construction and destruction, 30 kilometres south-west of the city of Cuenca, right in the middle of the Quimsacocha National Recreation Area. The deposit is a high-sulfidation epithermal Gold-Copper-Silver system. More than 13 million tons of rock are estimated to be extracted to obtain 62.4 tons of gold over a period of 12 years (Barros et al., 2024; DPM Metals, 2025).

### 6.2.1. Groundwater Handling

The mine will be operated as an underground mining operation. As stated by DPM this should minimize the surface impact compared to an open-pit mining operation. The mine design should produce 3000 to 3500 tons per day (Frost et al., 2021; DPM Metals, 2025). Based on hydrological modeling by Itasca the groundwater inflows were estimated. During the ramp development phase the peak inflow will be 7.5 l/s and during the production phase the peak inflow will be 13.8 l/s. These represent the amount of groundwater entering the mine (DPM Metals, 2025).

**Ramp development phase:**

During the ramp development phase water will first be pumped out of the settling pond near the portal. As the ramp development advances small underground collection basins (sumps) will collect the groundwater and wastewater, which is then pumped to the settling pond near the mine portal (DPM Metals, 2025).

For the ramp development equipment will be used that uses on average 10.800 liters of water per day. During the fist 300 meters of the ramp the natural groundwater inflow will not be sufficient so 50% of the necessary water will have to come from anther water source. After this 100% of the water will be recycled. Eventually a second development crew will start working which will double the water required (DPM Metals, 2025).

**Production phase:**

During the production phase all process water will come from the main dewatering system, this means that only water pumped from the mine itself is used. The production drills and the equipment that was already used during ramp development will have a daily water consumption of 45.000 liters. Throughout the full mine life the underground water supply will entirely come from the water collected underground (DPM Metals, 2025).

### 6.2.2. Streams

In this section the different streams from the mining processes are defined. For this study, not all mine activities are relevant. Therefore, these will not be discussed further here. The various (waste)water streams will be discussed below.

**High-pH Process Water:**

The high-pH process water comes from the grinding circuit thickener, copper thickener and pressure filters. This water ends up in a tank that is part of the distribution system and is reused in several places. It feeds directly into the ball mill, which is part of the grinding circuit and the copper flotation feed is conditioned with the high-pH process water and milk of lime (DPM Metals, 2025).

**Low-pH Process Water:**

The low-pH process water is recovered from the grinding circuit, the tailings thickener and the pyrite pressure filters. Like the high-pH process water this water also ends up in a tank that is part of the distribution system. This water will only be reused for pyrite flotation conditioning (DPM Metals, 2025).

**Contact Mine Water:**

Contact mine water comes from the mine and is a mix of contact water and groundwater that is pumped from the mine to maintain a safe working environment. This water is collected and either used as mineral process water or treated in the waste water treatment plant (DPM Metals, 2025).

**Filtered Tailings Filtrate:**

The filtered tailings filtrate first comes from the pyrite flotation where the tails and up in the tailings thickener. From here the filtered tails are it either goes to the filtered tailings storage facility or is used as paste backfill plant at the mine. The low-pH water is recovered and used as stated above (DPM Metals, 2025).

**Fresh/Raw Water:**

When fresh water is needed this will either be collected from local ponds or comes from the wastewater treatment plant located onsite. This water is mainly used as a buffer when process demands are not met, for pump gland seals as these need fresh water to work properly and as fire water reserve (DPM Metals, 2025).

**Sewage and Grey Water:**

A buried sewer network collects the sewage and gray water of the various buildings across the facility and discharges to a sewage treatment plant where the water is treated and discharged (DPM Metals, 2025).

## 6.3. Effluent Handling Plan (DPM)

Contact water, including groundwater extracted for safe operations, is collected, treated through thickeners and filters, and reused in mineral processing whenever possible. The water management system minimizes mixing of clean surface water with contact water, defined as any water that has been in contact with mineralized materials, ore, waste rock, tailings, or processing areas. Unused contact water is treated in the WWTP before discharge, while sewage is handled separately and sent to an external treatment facility.

Treated water must meet drinking-water standards before discharge, which occurs outside the Cuenca municipal watershed to protect upstream quality. All precipitation and runoff within the site catchment are captured and treated as needed to meet the most stringent of Ecuadorian or downstream standards. The main contaminants of concern are dissolved metals and nitrogen compounds from blasting and waste rock; metals remain the dominant concern during operation. Natural runoff is diverted around the site where feasible to further reduce contamination(DPM Metals, 2025).

### 6.3.1. Chemistry Mine Drainage Water

DPM did some research on the expected chemistry of the mine drainage. ETAPA has indicated that these design parameters are implausible. However, as this is the only numerical information available on mine drainage chemistry, it will be discussed briefly (DPM Metals, 2025; Barros et al., 2024). The most important values are summarized in table 6.1. This table displays all parameters that are close to, or go over the Ecuadorian water standards (FAO/FAOLEX, 2022).

All parameters mentioned are either close to the limit in the high-concentration scenario or exceed the limit (entirely).

### 6.3.2. Waste Water Treatment Plant (WWTP)

As stated before, contact water that is not used for mineral processing will be treated at the onsite wastewater treatment plant with a maximum capacity of 3300 $m^3$/day. The WWTP is designed as a single line treatment plant (Barros et al., 2024). The Feasibility study by DPM only provides the steps and reagents required for the wastewater treatment plant. This section will elaborate further on this and explained treatment steps in more detail. The following steps and corresponding reagents are mentioned in the study and combined in figure 6.1.

**Oxidation:**

The first treatment step is oxidation. In this case, this step is used to oxidize $Fe^{2+}$ to $Fe^{3+}$ and $Mn^{2+}$ to $Mn^{4+}$. Calcium hypochlorite, $Ca(OCl)_2$, is used as an oxidizing agent. The oxidizing agent is the chemical used in a redox reaction that accepts an electron from the reducing agent. Chlorine and its compounds, like $Ca(OCl)_2$, are commonly used as oxidizing agents. (Riedewald, 2011);(van Dijk,

| **Parameter** | **Low Concentration** *[mg/L]* | **Base Concentration** *[mg/L]* | **High Concentration** *[mg/L]* | **Limit Concentration** *[mg/L]* |
|---|---|---|---|---|
| **pH** | 5.5 | 5 | 4.3 | 5-9 |
| **Alkalinity** | 68 | 93 | 120 | - |
| **Al** | 0.073 | 3.6 | 7.1 | 0.1 |
| **As** | 0.016 | 0.03 | 0.044 | 0.5 |
| **Mn** | 0.78 | 0.97 | 1.17 | 0.1 |
| **Fe** | 9 | 20 | 36 | 0.3 |
| **Pb** | 0.002 | 0.009 | 0.019 | 0.01 |
| **$SO_4^{2-}$** | 39 | 120 | 210 | 400 |
| **$NO_3^-$** | 29 | 58 | 87 | 10 |
| **Cr** | 0.00073 | 0.023 | 0.046 | 0.05 |
| **Hg** | 0.0001 | 0.00015 | 0.0002 | 0.0002 |
| **Se** | 0.011 | 0.0111 | 0.012 | 0.01 |

Table 6.1: Mine Drainage Water Chemistry Barros et al., 2024

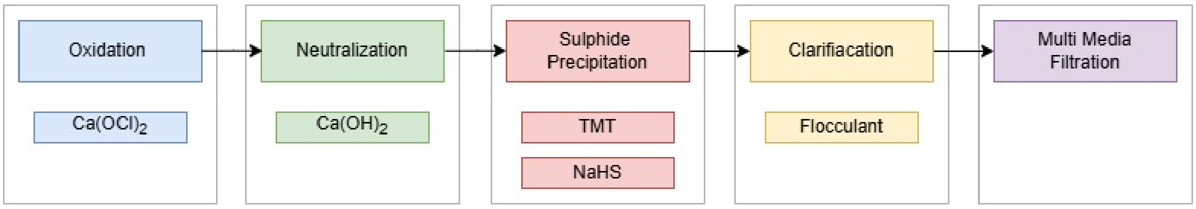

Figure 6.1: Treatment Line Flow Diagram Waste Water Treatment Plant, Authors own figure

2016b)

**Neutralization:**

After oxidation, a neutralization step is applied. Since chlorine oxidation is less effective at higher pH levels, it is more efficient to first oxidize the effluent and afterwards neutralize it once oxidation is complete (van Dijk, 2016b; Balladares Varela et al., 2018). Lime, $Ca(OH)_2$, is added to the water, which not only increases the pH but also promotes the precipitation of metal hydroxides.

$$\mathrm{M}^{n+} + n(\mathrm{OH})^{-} \leftrightarrow \mathrm{M(OH)}_n$$

$M^{n+}$ and $OH^-$ represent the dissolved metal ions and the precipitant, respectively, while $M(OH)_2$ is the resulting insoluble hydroxide that precipitates from the solution (Pohl, 2020).

**Sulphide Precipitation:**

Sodium hydrosulphide (NaHS) is used for sulphide precipitation, which is also an effective method for removing heavy metals. The main advantage of this method compared to lime precipitation is that metal sulphides have much lower solubility than metal hydroxides (Pohl, 2020).

$$\mathrm{M^{n+}} + n\mathrm{HS}^- \rightarrow (\mathrm{MS_n})_{(s)} + n\mathrm{H}^+$$

A precipitation reaction with sodium hydrosulphide occurs when metal ions ($M^{n+}$) react with hydrosulphide ions ($HS^-$) released from NaHS, forming insoluble metal sulphide (MS) precipitates.(Lewis, 2010)

TMT is also mentioned for sulphide precipitation. TMT or Trimercapto-s-triazine ($C_3N_3S_3^{3-}$) is an organosulphide reagent commonly applied for the precipitation of heavy metals such as Cu, Cd, Hg, and Pb due to its ability to form highly stable metal–sulphur compounds (Yazici et al., 2019). The general reaction of TMT with a metal ($M^{n+}$) has the following form:

$$3\,\mathrm{M^{n+}} + n\,(\mathrm{C_3N_3S_3})^{3-} \rightarrow \mathrm{M_3(C_3N_3S_3)_n}$$

It is important to notice that this reaction is pH dependent and its behaviour will change for a lower pH.

**Clarification:**

Clarification is used to separate the treated water from the precipitate. To enhance this process a flocculant. The next step in the process is slow mixing to enhance flock formation (van Dijk, 2016c). A basic clarifier is displayed in figure 6.2:

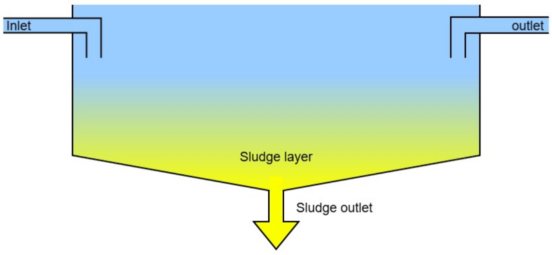

Figure 6.2: Schematized Clarifier Design, Authors own figure

As stated before the Feasibility study by DPM does not clarify what type of flocculant and clarifier are used.

**Multi Media Filtration:**

Multi Media Filtration consist of a layered filter bed where the different layers vary in grain size. On top lays a layer with a large grain size and on the bottom a layer with a small grain size. This means that solids solids end up in the top layer and smaller solids end up in the bottom part of the filter (van Dijk, 2016a). This is the last step of the WWTP design by DPM.

### 6.3.3. Tailings

After the ore from the mine is processed the valuable minerals are separated from the waste material. These are the tailings. This done through a flotation process of which the tailings slurry is a by product. The tailings slurry goes through several steps before disposal. These steps will be discussed below.

**Thickening and Filtration:**

The tailings are first thickened to remove as much water as possible. Afterwards they are filtered to create a semi-dry, clay like material with minimal moisture content. This process minimizes the risk of dam failures and reduces the need for a large tailings pond (DPM Metals, 2025).

**Tailings destinations:**

The tailings are divided over two destinations. Half of the tailings are stored on the surface in the filtered tailings storage facility (FTSF). The other half of the tailings are mixed with cement and water to create a paste backfill which is pumped underground to fill empty mining space to provide structural support. This method is used to limit the mine size and promotes underground stability (DPM Metals, 2025).

**The Filtered Tailings Storage Facility (FTSF):**

The filtered tailings facility is located on at an elevation of approximately 3800 meters on a topographic saddle at the head of a small watershed. The FTSF will have a ring dike configuration using rock fill embankments. Enclosing the tailings in all directions. The tailings are potentially acid-generating (PAG) and can leach metals and other constituents of potential concern (COPCs). Because of this the following design components are included:

- Surface water diversion channels;
- Geomembrane lining systems;
- Underdrain collection systems;

- Leachate recovery ponds;
- Embankment drains and risers;
- Closure cover system;
- Groundwater collection system.

All drainage, seepage and runoff water from the FTSF is routed to the WWTP for treatment (DPM Metals, 2025).

It is expected that the FTSF will contain six million tonnes of tailings after twelve years of mining. The facility will then be sealed with a multilayer cover consisting of a geomembrane, overburden, and topsoil to promote the regrowth of native Páramo vegetation. Drainage and seepage collection will continue for about ten years after closure. Once the water from the underdrain system meets discharge standards, the wastewater treatment plant (WWTP) will be dismantled, and all other installations will be removed so that the site can blend back into the natural landscape. Long-term monitoring will be carried out to ensure environmental stability and successful reclamation (DPM Metals, 2025).

## 6.4. Environmental impact

Mining is identified as one of the human activities that have the greatest negative impact on environmental quality. Its impacts range from ecological destruction to loss of biodiversity and pollution of water resources. Which makes mining sites a permanent toxicological problem for the surrounding ecosystems and human health (Wahab, 2011). This section will further elaborate on the environmental impact of the Loma Larga mining project.

### 6.4.1. Contamination Pathways

In this chapter, many different contmination pathways were defined. All streams defined in section 6.2.2 could potentially leak into the environment when systems and pipes are not maintained properly, causing environmental problems. But acid mine drainage, tailings seepage and structural failure of the FTSF, and inadequate water treatment cause environmental hazards.

Furthermore, it is of great importance that all water entering the system meets de right standards due to connectivity in the surface–subsurface network. On a yearly basis the direct groundwater contribution to stream discharge is 26.8% in wet periods and 45.5% in dry periods. During wet periods, groundwater recharge is strong and infiltration is rapid. The system mixes vertically and laterally and even in dry periods there is still infiltration into deep groundwater layers (Jerves et al., 2023). This means that drainage, seepage, and run-off that ends up in the environment can end up in the deep groundwater system. In this section, different streams that could cause contamination are identified.

**Acid Mine Drainage:**

Metal sulphide minerals are present in most types of rock associated with metal mining activity. The oxidation of these minerals and the formation of sulphuric acid, as well as the mobilization of these metals, is a slow natural process. Mining activity exposes large volumes of sulphide rock to water and oxygen, increasing the oxidation rate (U.S. Environmental Protection Agency, 1994). The mineralogical analysis done by DPM shows that pyrite, $FeS_2$, is a dominant mineral in the mining area (DPM Metals, 2025). This means that pyrite, but also other sulphide mineral containing rock surfaces, will constantly be exposed to infiltration water, leading to acidification of subsurface flows and open water in the area (Barros et al., 2024). Once oxidation begins, acid mine drainage can persist for centuries if continuous neutralization measures are not applied. The same process has caused chronic contamination in Andean mines (U.S. Environmental Protection Agency, 1994).

**Tailings Seepage and Structural Failure:**

Approximately 5.5 million dry tonnes of tailings will be placed at the filtered tailings storage facility during the lifetime of the mine (DPM Metals, 2025). The FTSF is located directly upstream of Cuenca's drinking water intakes. Nineteen water intake points by the rivers Irquis, Portete, Tarqui, Bermejos, and Yanuncay are connected to this upstream area (Barros et al., 2024). Water contamination by the tailings facility can be caused by seeping. However, other problems can also occur, such as spills, pipe leaks, or overtopping of the facility (Morrill et al., 2022). A big risk formed by the FTSF is structural failure. The structural failure of a tailings dam could result in the release of large amounts of contamination into the environment (Witt and Schönhardt, 2004). The most common failure mechanisms are overtopping, piping, internal erosion, liquefaction, and slope instability, but collapse of internal pipes or towers can also trigger failure. The Andean rainfall regime (1000-1400 mm/year precipitation) and the steep slopes amplify the changes of these failure modes. Overall the FTSF design is unsafe and unsustainable, missing emergency response protocols, and could cause permanent environmental damage to the area (Barros et al., 2024).

**Water recirculation:**

Within the water recirculation circuit, filtration and thickening are applied to remove suspended solids, although dissolved contaminants remain untreated. Recirculation accumulates dissolved contaminants over time (Barros et al., 2024).

**Inadequate water treatment:**

As the feasibility report of DMP provides only limited information on the wastewater treatment plant design, a literature study was done to gain a clearer understanding of the design. This shows that no final pH correction takes place. This means that the effluent will still be too acidic when it returns to the environment, causing acidification of streams. As stated before, the WWTP will have a maximum capacity of 3300 $m^3$/day. With a total water use between 533 and 610 $m^3$/hour (Barros et al., 2024) and taking into consideration that water recirculation will cause accumulation of contaminants so additional treatment will be necessary, the WWTP capacity will not be sufficient.

### 6.4.2. Water Scarcity

ETAPA (Barros et al., 2024) states that the region is already struggling with structural water shortages. The current water demand for human consumption and irrigation in the region is approximately 300 l/s. This greatly exceeds the dry season supply of 51 l/s. The Loma Larga mine will extract 22.6 l/s of rainwater and groundwater. This makes this dry season deficit even larger. Chapter 4 observes a possible negative rainfall trend for the higher-lying areas, as well as a negative trend in soil moisture. This could mean that in the future, even without the construction of the mine, water scarcity could increase. Ultimately, this will only amplify each other.

# 7

# Stakeholder analysis

The goal of this analysis is to identify the stakeholders involved in the loma larga project, map them and analyze their relationships. In addition, conclusions can be drawn from these analyses.

## 7.1. Literature study

This first section is a study in literature about the loma larga project. It starts with more background information on the mine. After that, the policies regarding the project are discussed.

### 7.1.1. Loma larga background information

The Loma Larga project, formerly known as Quimsacocha, is a proposed large-scale underground mine for the extraction of gold, silver and copper. It is located around 30 km southwest of Cuenca in the Azuay Province of Ecuador's Andean highlands, at an elevation of approximately 3,500 metres. The project area covers approximately 8,000 hectares of the important wetland ecosystem of the Quimsacocha páramo, which feeds the Tarqui, Yanuncay and Rircay rivers. These rivers provide drinking water to Cuenca and nearby rural communities (Barros et al., 2024; Hidayat, 2025; Valladares and Boelens, 2019).

The concessions were originally explored by IAMGOLD in the 1990s, transferred to INV Metals in 2012, and acquired by Dundee Precious Metals (DPM) in 2021. The mine's feasibility study predicted that approximately 1.86 million ounces of gold could be produced over 13 years through underground extraction (Frost et al., 2021). However, strong resistance to the project has been fuelled by environmental and social concerns, such as the risks of acid drainage, arsenic contamination and damage to sacred, water-rich páramo ecosystems. Local, indigenous and farming organisations, including Interjuntas, SCA and CONAIE, have joined forces to defend 'water and life over gold' (Valladares and Boelens, 2019).

This ongoing conflict has made Loma Larga one of Ecuador's most symbolic cases of tension between national resource policy, local autonomy and environmental protection, highlighting the deep social and political divisions concerning mining in the Andes.

### 7.1.2. Policies

The Loma Larga project is taking place in a context of changing legal and institutional settings, which reflect Ecuador's management and control of its natural resources.

The Mining Mandate (2008) and the Mining Law (2009) marked a turning point by reopening the country to large-scale mining investments following a period of prohibition (Valladares and Boelens, 2019). Although these laws were intended to centralize control over natural resources under state authority and attract foreign capital, they also triggered strong opposition from indigenous, rural, and environmental movements who are opposed to mining in areas that are sources of water (Valladares and CEDLA-UvA, 2018).

The draft Water Law (2010) further fuelled social unrest. While it aimed to modernize water management, critics argued that it reinforced state dominance and restricted local and community-led water governance (Boelens et al., 2015). Movements such as SCA and CONAIE organized national protests, road blockades and legal challenges against what they viewed as violations of the constitutional principles of ”Buen Vivir” and the rights of nature (Valladares and CEDLA-UvA, 2018).

At the same time, the government adopted what Boelens et al., 2015 describe as ’neoliberal-centralised water governmentality’, combining economic liberalisation with increased state control. This included promoting extractive projects as national priorities, using compensatory programmes to reduce opposition and restricting critical NGOs through presidential decrees that regulated civil society organisations and dissolved groups considered to ’undermine public peace’ (Valladares and CEDLA-UvA, 2018).

These policies and laws show that Ecuador’s mining and water rules officially promote sustainability and fairness. However, in practice they limit local decision-making and increase tensions over projects like Loma Larga.

## 7.2. Stakeholder mapping

In this part of the chapter, all involved stakeholders are listed and divided into three groups: public, private and civil stakeholders (see chapter 2.6 Figure 2.4 for the full overview).

### 7.2.1. Public stakeholders

This section lists the public stakeholders and describes their role in the Loma Larga project. Figure 7.1 provides an overview of the public stakeholders.

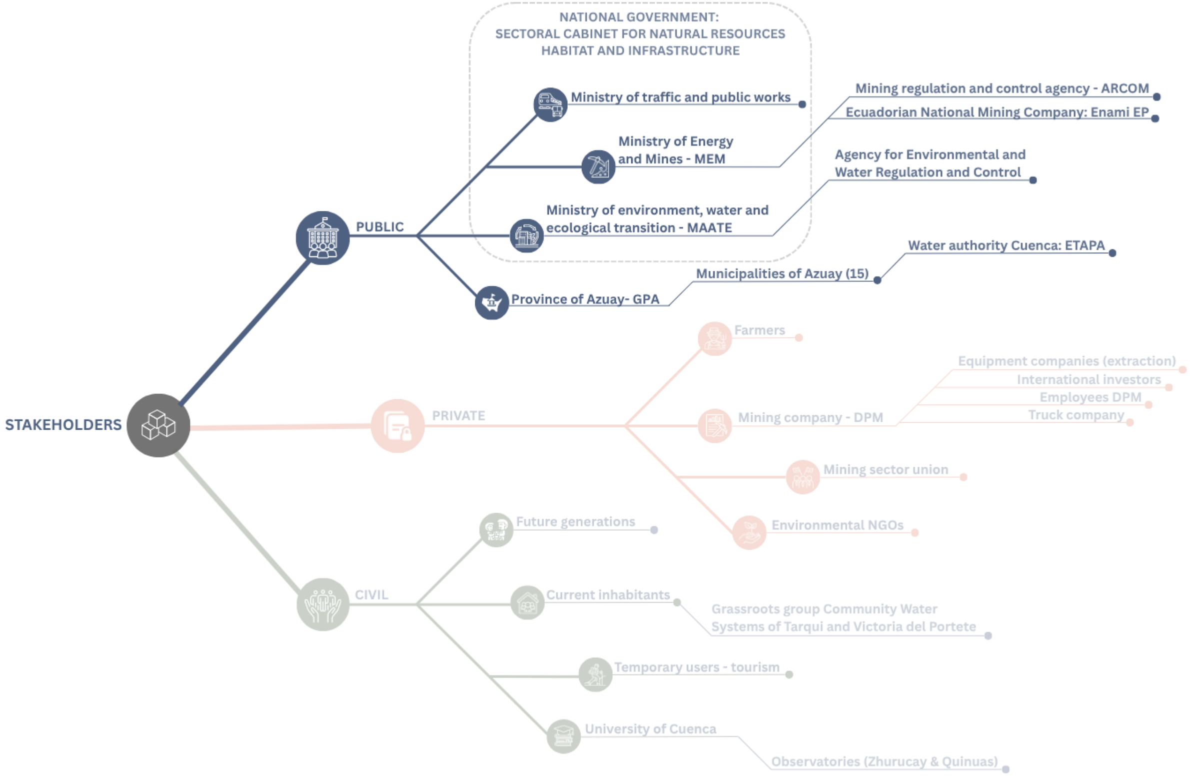

Figure 7.1: Overview of public stakeholders

**National Government**
As part of its economic development strategy, the national government of Ecuador plays a central role in regulating and promoting the mining sector. Mining is a major source of public revenue, creating tens of thousands of jobs and generating billions in taxes and export earnings (International Trade Administration, 2025). Several ministries oversee and support the Loma Larga project, each with specific responsibilities, which are described in the following sections. The national government coordinates these institutions and makes final decisions on permits and policies. Recently, however, it revoked the Loma Larga environmental permit due to local opposition, environmental concerns and an incomplete report by Dundee Precious Metals (**schertow-2025**; **valencia-2025**).

**Ministry of Traffic and Public works - MTOP**
The Ministry of Transport and Public works (MTOP) is responsible for managing national infrastructure, including roads, bridges and transport systems (Ministerio de Infraestructura y Transporte, n.d.). In the Loma Larga project, the MTOP coordinates transport routes for machinery and mineral exports. The ministry also collaborates with regional governments to integrate mining-related infrastructure into broader development plans.

**Ministry of Energy and Mines - MEM**
The Ministry of Energy and Mines (MEM) regulates Ecuador's mining sector, grants concessions and oversees project implementation (BNamericas, 2025). For the Loma Larga project, MEM manages the mining contract and ensures compliance with safety, technical and social requirements. It also coordinates with other agencies, such as ARCOM, to monitor the project (Frost et al., 2021).

**Mining regulation and control agency - ARCOM**
ARCOM (Agencia de Regulación y Control Minero) enforces mining laws, monitors concessions and controls mining activities nationwide (Agencia de Regulación y Control Minero, n.d.). In Loma Larga, it ensures that the operator complies with mining regulations and safety standards.

**Ecuadorian National Mining Company - Enami EP**
ENAMI EP is Ecuador's state-owned mining company, responsible for promoting and managing public mining interests (ENAMI EP, n.d.). While it is not directly involved in the Loma Larga project, ENAMI EP supports national mining policy, attracts investment and ensures state participation by forming partnerships, sharing technology and building local infrastructure.

**Ministry of environment, water and ecological transition - MAATE**
The Ministry of environment, water and ecological transition (MAATE) is responsible for environmental policy and the issuance of environmental permits in Ecuador (**Ministerio-del-Ambiente**). In the context of the Loma Larga project, MAATE oversees the assessment of environmental impacts, ensures compliance with environmental laws and monitors water resource protection. The ministry's decisions are crucial for project approval and continuation. Until new laws are approved, companies must follow executive orders and ministry guidelines. On October 4th, 2025, MAATE revoked the environmental permit for the Loma Larga project (**valencia-2025**).

**Agency for Environmental and Water Regulation and Control - ARCA**
As part of MAATE, ARCA is responsible for regulating and monitoring Ecuador's water resources. It ensures fair distribution of water, establishes technical standards and oversees compliance. In the Loma Larga project, for example, ARCA is responsible for verifying that mining activities and water-use permits comply with national water quality and sustainability regulations (Agencia de Regulación y Control del Agua, n.d.).

**Province of Azuay - GPA**
The GPA coordinates regional development policies with a focus on sustainable land and water management (Gobierno Provincial del Azuay, n.d.). The GPA plays a central role in aligning provincial environmental priorities with national mining strategies, as well as mediating between local communities and national authorities.

**Municipalities of Azuay**

Azuay has fifteen municipalities, the largest of which is Cuenca in terms of population. Municipalities are responsible for local planning and the implementation of environmental regulations. The Loma Larga area overlaps with Cuenca’s water reserve, which has made it a central topic of public concern. Local authorities also have the constitutional right to hold community referendums on mining near water sources (**international-trade-administration-2025**).

**Water authority - ETAPA**

ETAPA EP is, among other public services, Cuenca’s public water company that protects drinking and irrigation water in the Quimsacocha reserve (EP, 2025). By monitoring potential contamination, it works to ensure that mining does not endanger Cuenca’s water supply, playing a critical role in environmental protection (Barros et al., 2024).

## 7.2.2. Private stakeholders

Private stakeholders (see Figure 7.2) are the companies and economic actors that are directly or indirectly involved in the mining value chain.

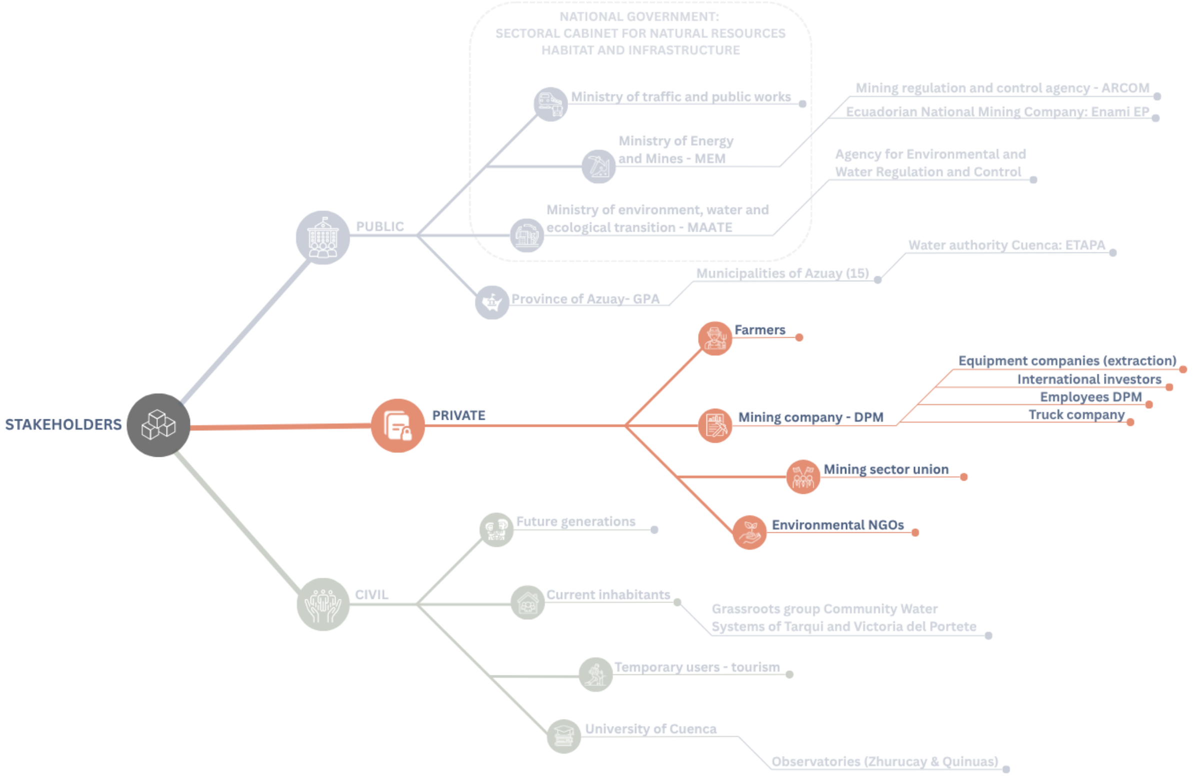

Figure 7.2: Overview of private stakeholders

**Farmers**

Local farmers near the project rely on agriculture and cattle farming for income (Frost et al., 2021). The irrigation potential in Ecuador far exceeds current usage, meaning that water demand is expected to increase (Buytaert et al., 2006). As they depend on clean water sources such as the Quimsacocha system, farming communities are financially vulnerable to mining operations.

**Mining sector union - Ecuadorian Chamber of Mines**

The Ecuadorian Chamber of Mines is the representative union for the national mining industry. The Chamber promotes responsible mining and sustainable development and facilitates dialogue between companies, the government and civil society (CME, 2025).

**Mining company: Dundee Precious Metals - DPM**
Dundee Precious Metals Inc., a Canadian mining company, owns 100% of the Loma Larga project through its subsidiary, DPM Ecuador Holdings Inc. The company is responsible for the mine's design, construction and operation. The company follows international standards, such as the IFC Performance Standards, for environmental and social management (Frost et al., 2021).

**Equipment companies**
Suppliers provide the machinery and technical services required for drilling, extraction, hauling and processing. They benefit from industrial demand and frequently work together with the main operator during the construction and production phases.

**International investors of Dundee Precious Metals**
Dundee Precious Metals' investors and shareholders provide funding for the Loma Larga project and receive a share of its profits (DPM Metals Inc., 2025; Metals, n.d.). They expect the company to meet international environmental and social standards in order to protect their investments and its reputation.

**Employees of Dundee Precious Metals**
Dundee Precious Metals (DPM) employees are responsible for operating and managing the Loma Larga project (Feasibility Study Report, Dundee Precious Metals, 2021). This team includes engineers, technicians and administrative staff who ensure that mining operations are carried out following the rules and regulations safely and efficiently. As members of the company workforce, they also benefit from wages, training and the local employment opportunities created by the project (Frost et al., 2021).

**Truck company transporting materials to and from mine**
Local and regional transport firms will be responsible for delivering mineral products from the mine to ports such as Guayaquil (Frost et al., 2021). They play an essential role in export logistics and regional employment.

**Environmental NGOs**
Environmental NGOs have played a significant role in opposing the Loma Larga project, providing research, legal support and advocacy in order to protect the Quimsacocha páramo and its water sources. Despite these efforts, many NGOs have faced government restrictions, with some even being dissolved under presidential decrees for allegedly threatening state security or public order (Valladares and Boelens, 2019). Nevertheless, they remain allies of local and indigenous movements defending water and nature's rights.

### 7.2.3. Civil stakeholders

Civil stakeholders are the non-governmental and community organisations affected by or involved in the project, see Figure 7.3.

**Future generations**
The social and ecological outcomes of current decisions about Loma Larga will be inherited by future generations. Although they are not involved in direct negotiations, they are very important for the constitutional principles of sustainability and the Rights of Nature (Barros et al., 2024; Valladares and CEDLA-UvA, 2018). Local and Indigenous movements often talk about their protection as a moral duty. They say that resisting mining is a way of protecting water, land, and the wellbeing of future generations (Valladares and Boelens, 2019).

**Current inhabitants**
The communities living near the project area, including indigenous and rural populations (like in Girón and San Fernando), depend on farming and livestock (Frost et al., 2021). They have organised protests to protect the Quimsacocha watershed, expressing concerns over water quality and cultural impacts (Morin, 2025).

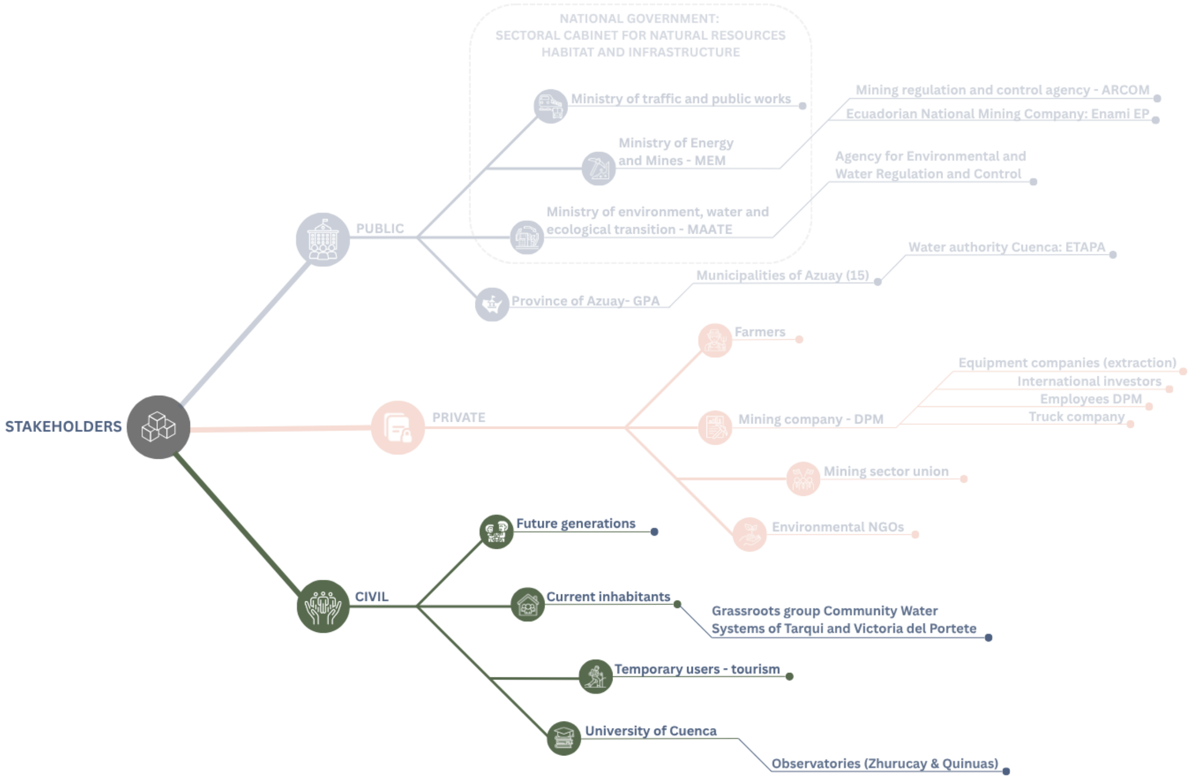

Figure 7.3: Overview of civil stakeholders

**Grassroots group: Community water systems of Tarqui and Victoria del Portete**
The Community Water Systems of Tarquí and Victoria del Portete are grassroots collectives of rural and indigenous residents who depend on the Quimsacocha páramo for drinking water and farming. They have led opposition to the Loma Larga project, organising community consultations that rejected mining in local water recharge zones by an extensive majority (Morin, 2025).

**Temporary users - tourism** The majority of temporary users are tourists visiting national parks in the páramo region, such as El Cajas. These visitors are attracted by the area's unique landscapes, biodiversity and cultural value. However, unregulated tourism has already harmed the páramo ecosystem: ”(...) estimating that more than three quarters of the entire area originally occupied is modified or has been transformed by human activities, among them, tourism developed in these areas.” (Almeida Peñaherrera, 2023). The development of the Loma Larga mine will concentrate tourists in an even smaller area, further intensifying environmental pressure. In order to ensure that tourism can continue to be viable in this vulnerable environment, it is essential to implement a sustainable tourism management model (Almeida Peñaherrera, 2023), to balance tourism with ecosystem protection.

**University of Cuenca**
The University of Cuenca is a leading institution in the research of páramo ecosystems around Azuay. In collaboration with ETAPA and other partners, it has gathered valuable data on hydrology, biodiversity and ecosystem dynamics (Correa et al., 2016; Jerves et al., 2023; Pesántez et al., 2018; Pesántez et al., 2023). Its research underscores the critical role of the páramo in regulating water and maintaining ecological balance. Findings suggest that mining activities such as those at Loma Larga could seriously disrupt these functions (Barros et al., 2024; Buytaert et al., 2006; Mosquera et al., 2023; Valladares and Boelens, 2019), emphasising the importance of continued scientific monitoring and research.

**Observatories (Zhurucay & Quinuas)**
The Zhurucay and Quinuas observatories collect high-quality data on rainfall, water flow and soil conditions in southern Ecuador's páramo ecosystems. Their role is purely technical, ensuring the reliable

monitoring of these variables. The University of Cuenca uses this data to analyse ecosystem dynamics and evaluate their impact on the environment.

## 7.3. Methodology

In this section the methodology used to analyse the stakeholders, is discussed. The two methods used to analyse the stakeholders are a power/interest matrix and a conflicting diagram. With these two methods, the stakeholders will be evaluated on the following criteria: level of power, degree of interest and attitude.

### 7.3.1. Power/interest matrix explanation and relevance

The power/interest matrix is a stakeholder analysis (SA) tool that is widely used to identify and understand stakeholder influence and engagement strategies. It categorizes stakeholders based on the first two criteria: their level of power and degree of interest regarding a specific project or issue. Considered a top-down analytical method, it divides stakeholders into four categories according to their relative influence (or power) and involvement (or interest) in the problem being addressed (Reed et al., 2009). This approach enables people working in this field to determine which engagement strategies to use, allocate resources effectively and anticipate potential conflicts. Power is defined as a stakeholder's ability to influence decisions, control resources or affect project outcomes. Interest, on the other hand, reflects the degree to which a stakeholder is affected by or cares about these outcomes (Ahsan and Pedersen, 2018; Guðlaugsson et al., 2020). The matrix's four quadrants represent different engagement strategies (InterregCentralEurope, 2025; Reed et al., 2009):

- **High power / high interest (manage closely):** These stakeholders are highly influential and deeply engaged. They require regular communication and involvement.
- **High power / low interest (keep satisfied):** These influential but less invested stakeholders should be kept informed and satisfied to avoid opposition.
- **Low power / high interest (keep informed):** These are stakeholders who are involved but have limited influence. They should be supported and consulted in order to maintain trust.
- **Low power / low interest (monitor):** These stakeholders have minimal influence or concern, so they only require periodic monitoring to detect changes in their position.

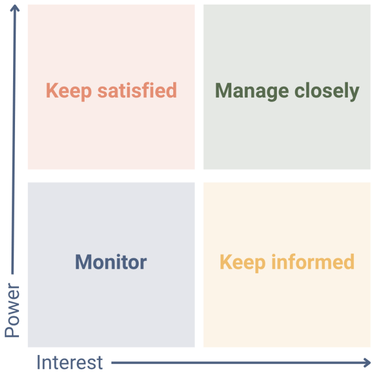

Figure 7.4: Power/interest matrix quadrants (Author's work based on (Eden and Ackermann, 1998)

In addition to power and interest, a third criterion, attitude (or commitment), has been added to the power/interest matrix to indicate stakeholders' views on the project. According to Riahi (2017), considering attitude enables project managers to adapt their engagement approach based on whether stakeholders are resistant, neutral or supportive. The original model identifies five commitment levels (unaware, resistant, neutral, supportive, and leading), but this analysis uses only three categories (resistant, neutral, and supportive) for simplicity. This allows for a clearer focus on the attitudes that most directly influence stakeholder behaviour and engagement strategies. Each level calls for a different strategy, as shown in table 7.1.

| Commitment Level | Recommended Strategy |
|---|---|
| **Resistant** | Listen carefully to concerns, influence through transparent communication and convince by pointing out underlying issues and demonstrating project benefits. |
| **Neutral** | Listen and monitor to evaluate whether attitudes shift toward resistance or support; provide clear information to prevent misunderstandings. |
| **Supportive** | Listen, inform, and thank stakeholders for their engagement; explore opportunities to involve them more deeply as advocates for the project. |

Table 7.1: Stakeholder commitment levels and corresponding strategies, based on (Riahi, 2017)

### 7.3.2. Conflict diagram explanation and relevance

A conflict diagram is a useful addition to the power/interest matrix as it offers a dynamic, relationship-based view of stakeholder interactions instead of a static classification of power and interest levels. While the power/interest matrix helps to identify and prioritize stakeholders, a conflict diagram illustrates how these actors interact with each other, revealing their relationships within complex projects (Wang and Wu, 2020).

In this diagram, stakeholders are divided into public, private and civil sectors (see also chapter 7.2). The distance from the centre indicates their degree of affectedness. Different kinds of lines are used to represent the relationship between the actors. Arrows represent collaboration, dotted lines represent conflict and solid lines represent coexistence. This makes the underlying social and institutional tensions visible, which cannot be captured by positional models (like power/interest matrix) alone. Additionally, shades of grey representing power levels (light = low, normal = medium, dark = high) provide a hierarchy of power.

This aligns with systematic conflict management approach (Wang and Wu, 2020), which emphasizes that mapping stakeholder conflicts improves conflict identification, resolution and prevention. The most important thing is not to stop conflict, but to understand why it happens, how it affects people and how we can deal with it in a positive way.

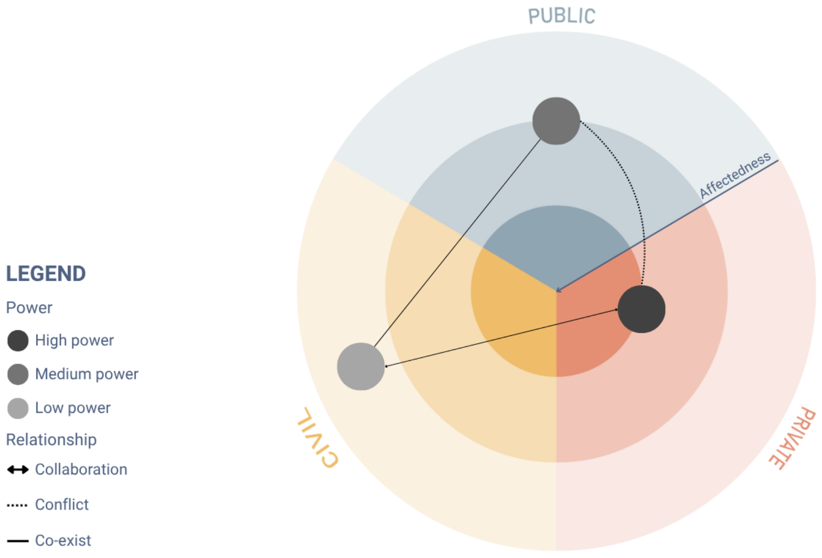

Figure 7.5: Conflicting diagram (Author's work)

## 7.4. Results

In this section both the power/interest matrix and the conflicting diagram are applied to all the stakeholders. The results are presented below.

### 7.4.1. Power/interest matrix

The power–interest matrix was developed using information from news articles and scientific studies (SOURCE). A detailed table (see Appendix D table **??**) presents all stakeholders ranked from highest to lowest in terms of power, and from most to least interested in the Loma Larga project. Important to point out are the following three stakeholders (circled in black in Figure 7.6): the national government, the canadian mining company Dundee Precious Metals and the current inhabitants. These three players from the most relevant players since they play central but contrasting roles in terms of power, interest and attitude. The national government holds the greatest power, as it controls mining policies, issues permits, and has the final authority to approve or suspend projects like Loma Larga. Its interest in the project is high, driven by the potential for significant economic growth. In 2024, the president even attended the Mining Conference in Canada to reassure investors and the company of the government's continued support for large-scale mining (Mining watch Canada, 2024).

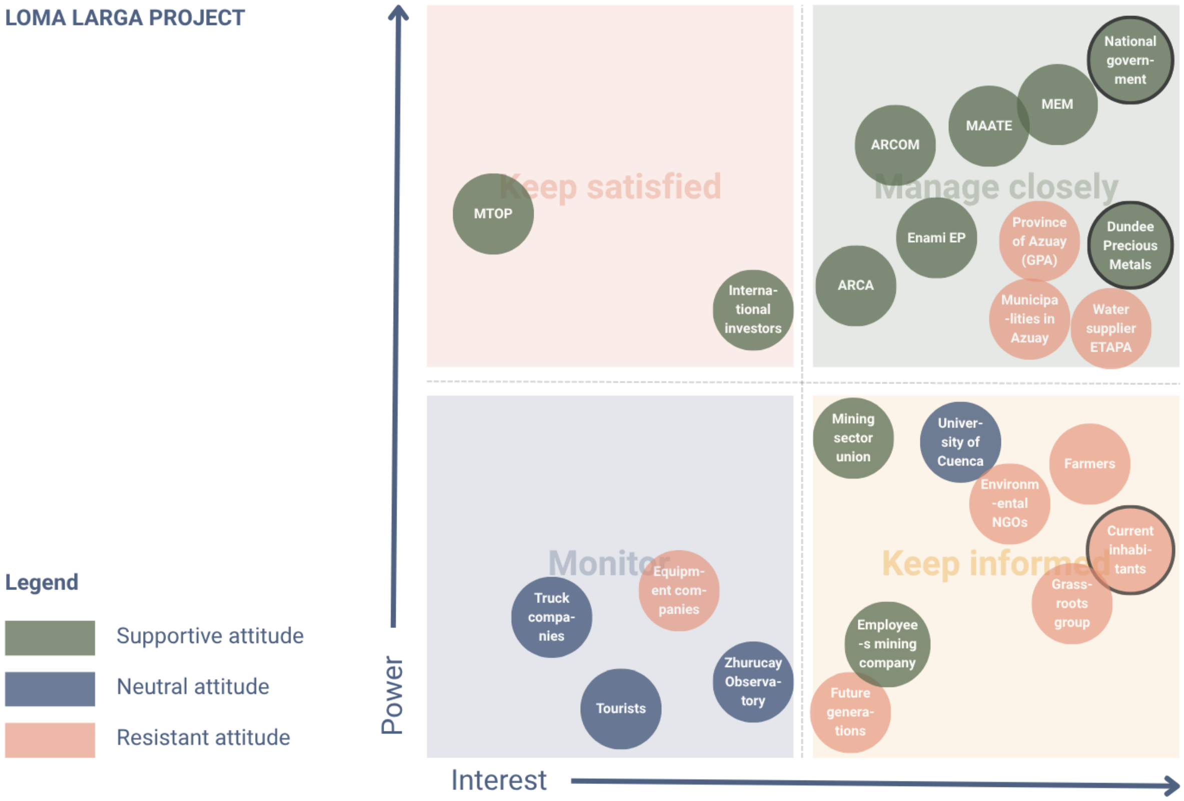

Figure 7.6: Power/interest matrix on the Loma Larga project (Author's work, 2025)

As the project operator, Dundee Precious Metals holds significant power due to its financial resources and technical expertise. The company has a strong interest in the project, as its success depends directly on the mine's approval and operation. Despite setbacks like the revocation of the environmental permit in October 2025 (Valencia, 2025), the company continues to negotiate with the authorities in order to move the project forward, so its attitude can be described as supportive.

By contrast, while the current inhabitants are strongly interested in the project, they have very limited influence. Their livelihoods depend on clean water and the fragile páramo ecosystems, yet they are not involved in decision-making processes. They oppose the mine due to deep concerns about water security and the will to protect the cultural and spiritual significance of the páramo (Morin, 2025).

These three actors play the most central roles in shaping the project's dynamics. While the government and the company prioritise development and economic growth, the local communities focus on protecting their environment and water resources. The way in which these groups interact will have a significant impact on the direction and outcome of the Loma Larga project. More on the interactions will be made clear in the conflicting diagram section 7.4.2.

### 7.4.2. Conflicting diagram

As already mentioned in section 2.4, the potential construction of the mine is a complex case involving many different stakeholders and conflicting interests. A conflict diagram has therefore been created, with the help of a conflicting table (see Appendix D table D.1) to illustrate the various (conflicting) interests (see figure 7.7).

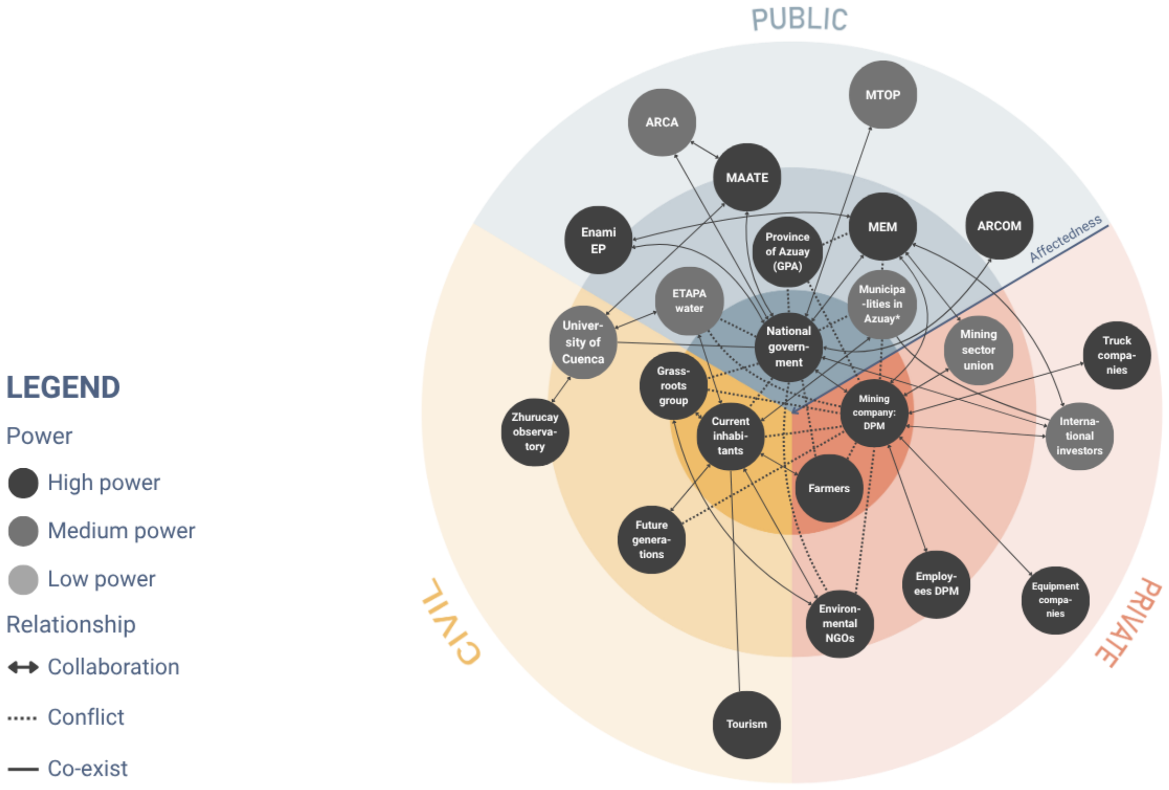

*15 municipalities in Azuay: Camilo Ponce Enríquez, Chordeleg, Cuenca, El Pan, Girón, Guachapala, Gualaceo, Nabón, Oña, Paute, Pucará, San Fernando, Santa Isabel, Sevilla de Oro, Sigsig

Figure 7.7: Conflicting diagram Loma Larga Project (Author's work, 2025)

In appendix D is a table with all stakeholder relationships and on what sources they are based. For a clearer overview, the conflicting diagram does not show all connections. In section 7.4.3 a conclusion is drawn from both analyses.

### 7.4.3. Conclusion from the results: main stakeholder conflicts

The main conflicts surrounding the Loma Larga project are caused by opposing interests between local communities, government authorities and the mining company (SOURCE).

The most prominent conflict is between local communities and the national government (Figure 7.8 [1]), which continues to approve plans with Dundee Precious Metals despite significant opposition. According to Brandi Morin (2025), 85% of residents living downstream rejected the mine, yet government institutions proceeded with environmental and development approvals. Community water organisations such as the SCA and the Community Water Systems of Tarqui and Victoria del Portete have filed multiple lawsuits demanding the withdrawal of mining concessions in protected water source zones (Valladares and Boelens, 2019). These groups argue that government actors have used constitutional principles, such as Buen Vivir (well-being beyond GDP) and the rights of nature, to justify mining projects while ignoring or silencing the voices of local communities (Instituto Nacional de Estadística y Censos, 2015; Valladares and CEDLA-UvA, 2018). Moreover, on 16 September 2025, more than 100,000 people marched through Cuenca, Ecuador, to demand the revocation of the environmental permit for the Loma Larga mine. They cited threats to the Quimsacocha water reserve as the reason for their protest (Fabara, 2025; Hanbury, 2025). The protesters were chanting slogans such as 'Water is worth more than anything' in an attempt to pressure the government into stopping mining operations (Reuters, 2025).

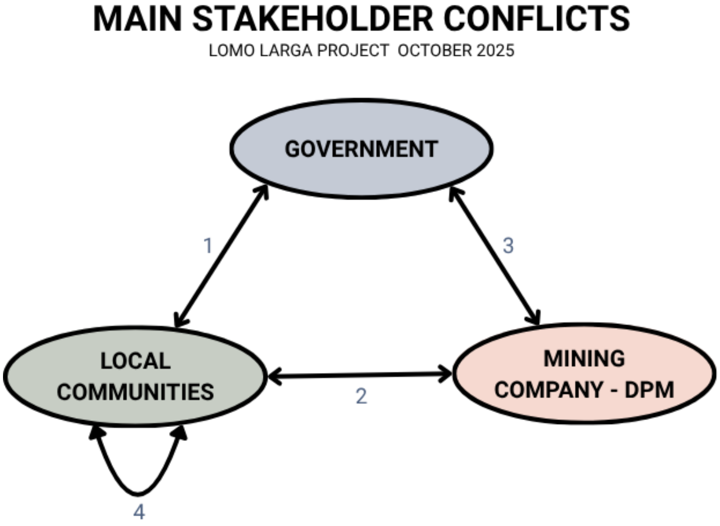

Figure 7.8: Main stakeholder conflicts (Elke van Thiel (2025) based on Wang and Xiang, 2019)

There are also notable tensions between local communities and Dundee Precious Metals (Figure 7.8 [2]). Independent studies warn that the mine could cause acid drainage, releasing arsenic and other heavy metals into nearby rivers and aquifers for generations (Morin, 2025). Activists such as Father Vega and community leader Koldo emphasize that local referendums in 2011, 2019 and 2021 all rejected mining in the páramo. Nevertheless, the company persists in its efforts to develop the project (Abulu et al., 2025; Morin, 2025). Many residents view this as a violation of their right to consultation and the cultural importance of Quimsacocha's sacred waters (Valladares and CEDLA-UvA, 2018).

More recently, a conflict has emerged between Dundee Precious Metals and the Ecuadorian government (Figire 7.8 [3]) following the revocation of the project's environmental permit in October 2025. The government cited shortcomings in the company's environmental assessment and growing local opposition as the reasons behind this decision (Hidayat, 2025). In response, DPM suspended drilling operations, expressing its "deep disappointment" with the decision. The company maintains that its studies met Ecuadorian standards and that the project would bring major economic and social benefits (Network, 2025). The company also requested clarification from the Ministry of Environment and indicated that it would collaborate with the authorities to resolve the issue. This dispute highlights the fragile balance between Ecuador's commitment to environmental protection and its efforts to attract foreign investment in the mining sector (Tomesco, 2025).

Finally, the project has caused divisions within local communities (Figure 7.8 [4]). The economic hopes of employment and infrastructure improvements are in direct contrast to the fear of water loss and contamination, resulting in social unrest. Incidents of violence, such as the attack on 62-year-old farmer Fanny Paute by residents who support the mining project, mark a shift from peaceful protest to open confrontation, highlighting the ongoing impact of unequal power dynamics between the state, corporations and communities on the conflict (Morin, 2025; Valladares and CEDLA-UvA, 2018).

Overall, the stakeholder analysis reveals that the Loma Larga project is defined by unequal power relations and complex social dynamics. Collective action is one of the few ways in which local communities can influence decisions, as was seen during the protests in September 2025. However, with the future of the project still uncertain, the balance between economic interests and environmental protection remains unstable.

# 8

# Conclusions

Reflecting on the main research question, *What are the effects of meteo/hydrological trends and mining projects in the south Ecuadorian Páramo system with respect to water quality, slope stability and local stakeholders?*, we find that a multi-source, multidisciplinary lens is essential to understand potential future risk in the South-Ecuadorian Páramo. Changes in weather patterns may drive significant risks related to water security and landslide occurrence. Furthermore, mining projects such as the Loma Larga mine could potentially degrade water quality. In subsequent sections, the answers to other research questions will be discussed in more detail.

*1) Can satellite data be used in the Páramo to create reliable models that predict parameters from the water balance?*

Remote sensing obtained data can be used to supplement in-situ measurements in the Páramo, depending on the parameter. Usability of these results is inherently limited due to lack of diverse in-situ measurements and satellite specifications. We found that soil moisture could successfully be retrieved from satellites, while other satellite parameters, such as land surface temperature and solar net radiation, produce insufficiently reliable results in the Páramo.

*2) Do temperature, precipitation, and soil moisture data collected in the catchment basins show any sign of a multi-year trend and whether a model can accurately forecast at least one year ahead*

In response to the research question defined in the introduction the analyses provide partial but meaningful insights. The Mann–Kendall tests suggest a consistent decreasing trend in soil moisture across most stations, while precipitation and temperature trends are less uniform and, in several cases, statistically debatable. The Unobserved Components Model (UCM) successfully captured the dominant temporal dynamics, particularly the autoregressive patterns, and was able to produce forecasts that remain reasonably accurate up to one year into the future. However, deviations in the 2023–2024 period indicate limitations in capturing short-term anomalies and highlight the model's sensitivity to abrupt climatic variability. Overall, the findings suggest emerging signs of long-term warming and possible hydrological shifts in the Páramo region, while also demonstrating that the UCM provides a robust framework for forecasting with the data at hand. Further refinement and extended datasets are needed to strengthen predictive reliability and trend confidence.

*3) What are the slope stability scenarios in the Páramo region of Cuenca, considering long-term hydrological trends? 4) What further research and information would be needed for increasing the accuracy of a landslide hazard assessment system in the Azuay province?*

Due to climate change, more frequent droughts and heavy-rainfall events are expected, and the Quinuas catchment is vulnerable to both. Extended dry periods can temporarily stabilise slopes, but rapid re-wetting during intense storms reduces effective stress through pore-pressure build-up, triggering shallow landslides. Prolonged wet anomalies and storm clusters on already wet soils expand susceptible zones on steep midslopes and convergent hollows, whereas brief stability during dry spells is lost rapidly upon re-wetting. These failures have substantial impacts on human lives and on the transport artery connecting Cuenca and Guayaquil. It is therefore of utmost importance to assess landslide risk in this catchment.

The LISEM model, which uses an infinite slope model, creates a first basis for mapping the risk of landslides throughout the Quinuas catchment and can be elaborated to the rest of the Azuay province. However, some adjustments and data collection have to be implemented to improve its reliability. With the amount of assumptions and generalisations that are currently present in the model, there is much room for increasing the accuracy of parameter values and incorporating spatial variability of the region. Hydrological parameters, such as Manning's N coefficient and vegetation cover, are based on the land cover classification which has a resolution of 30 meters. This is a sufficient resolution for landslide mapping. The soil parameters, internal friction angle, cohesion, density and soil depth, require spatial and numerical improvement. As little prior soil investigations have been done in this region, this is the area in which the most improvements can be made. Furthermore, manual calibration can be done based on known landslide occurrences to increase the accuracy of the landslide hazard assessment map further.

*5) How do differences in power, interest and commitment among involved stakeholders explain the main conflicts surrounding the Loma Larga mining project in Azuay?*

In regard to this subresearch question, the following conclusions can be drawn. Analysis of the Loma Larga project shows that main conflicts arise from imbalances of power, interests and commitment among stakeholders. The national government and Dundee Precious Metals hold the most power and influence, which is driven by their commitment to economic development and foreign investment. In contrast, local communities, who depend directly on the Páramo ecosystem for drinking water and irrigation, have a high level of interest but limited influence over decision-making processes. Their strong opposition results from concerns about water contamination, loss of livelihoods, and the protection of the Páramo's cultural and ecological value.

These differences in power and interest explain why conflicts have emerged between the government, the company and local residents. Within the communities themselves, however, tensions exist for different reasons. Here, the conflict stems from diverging interests: while some residents support the mine for its potential economic benefits and job opportunities, others prioritise protecting their cultural values and, most importantly, ensuring their access to clean, secure water. The project's unstable and uncertain future is further affected by the shifting political context, including the revocation and possible reinstatement of the environmental permit.

In relation to the main research question, the findings show that social and political factors, especially the unequal distribution of power among stakeholders, strongly influence the outcomes of mining in the Ecuadorian Páramo. The local population has very limited power compared to the government and the mining company, which makes it difficult for them to influence decisions. However, the protests in September 2025 demonstrated that collective action can be effective — when many people unite, their voices cannot be ignored. This highlights the fact that, in such a complex and unequal situation, strength lies in numbers.

*6) What are the regional water-related environmental impacts of the Loma Larga mine on surface and groundwater quality and water availability?*

The regional water-related environmental impacts of the Loma Larga mine on surface and groundwater quality and availability are considerable, despite the proposed mitigation strategies. The Loma Larga mine poses significant risks to both surface and groundwater within the Quimsacocha National Recreation Area. Due to the strong surface–subsurface connectivity of the Páramo, contamination from mine drainage, seepage, or runoff can easily infiltrate deep groundwater and reach downstream rivers. The likelihood of acidic effluent entering the environment is high because of the wastewater treatment plant's limited capacity and lack of final pH correction. Additionally, the filtered tailings storage facility, located at the head of a watershed, presents a major risk of seepage or structural failure, which could lead to irreversible contamination of local water bodies.

*7) How will the Cuenca water supply system be influenced by the Loma Larga mine?*

Cuenca’s potable water supply depends on rivers originating in the Quimsacocha páramo, making it highly vulnerable to mining activities in the area. The extraction of 22.6 l/s of groundwater and rainwater for mining will aggravate existing regional water scarcity, particularly during dry periods when supply is 51 l/s which already falls far below the demand of 300 l/s. Contaminants released through inadequate treatment or tailings leakage could enter the Tarqui and Yanuncay rivers, which directly supply Cuenca. Consequently, the Loma Larga project threatens both the quality and the reliability of Cuenca’s drinking water sources.

# 9

# Discussion

Interpretation of the findings in this report require caution. Firstly, most analyses are based on measurements that come from measurement stations. These measurements display an inherent uncertainty themselves due to the sampling techniques. The instruments might contain both systematic and random errors, for example due to accuracy, precision or uncertainty errors. For example, classical rain gauges, that were previously used to make precipitation measurements, do not properly include mist, which is a crucial form of precipitation in the Páramo. Figure 9.1 display a picture of the mist station from the Zhurucay observatory.

Figure 9.1: Mist precipitation station in the Zhurucay observatory (author's own).

As for the satellite data, some annotations must be made as well. For all parameters, only sets of 3 satellites were used, that were picked on performance based on literature. In future research, results could be improved by trying more (combinations of) satellites to create the model. Furthermore, when training the satellite, a constant bias was calculated between the model and the in-situ measurements. When validating the model, we saw that in some months the model performs significantly better than in other months. Therefore, utilizing a seasonally varying bias could improve model accuracy compared to in-situ. Also, features such as precipitation or land surface temperature could be used in future models to improve overall model accuracy.
Regarding the calibration of the SM-satellite model specificly, solely 1 in-situ measurement site was available (Zhurucay). This site is located on a slightly sloping hill with Tussock Grasses as land cover. Obviously, utilizing more in-situ sites to train the model, with different land covers, slopes, etc., would drastically improve model reliability. Also, a longer temporally aligned time-series compared to the $\sim 3$ years that were utilized now could improve model accuracy.

The combination of Mann–Kendall trend tests and Unobserved Components Models (UCM) provides valuable but somewhat contrasting insights into the hydro climatic dynamics of the Quinuas and Zhurucay catchments. While the SMK and RMK tests suggest generally decreasing soil moisture trends, mixed signals for precipitation and temperature readings, the UCM results reveal that short-term variability and autoregressive behaviour strongly influence the observed patterns. The substantial forecast error observed between mid-2023 and mid-2024 across all temperature stations suggests potential non-stationarity or external anomalies, possibly linked to short-term extreme periods. It should be noted that the identification of an extreme period is based solely on the UCM forecast deviation;

further analyses using extreme value theory or Monte Carlo simulations would be required to confirm this. Overall, the results suggest that while a long-term warming trend is plausible, part of the detected signal may be influenced by internal temporal dependence and short-term dynamics rather than a consistent external forcing.

For the prediction of landslides, various datasets are required to achieve the highest possible accuracy. One of these datasets is the synthetic storm used to represent extreme rainfall events. Due to time constraints, a 24-hour rainfall total was determined for each return period. However, the 24-hour total is not the form of input required by the LISEM model, which instead operates on a design storm with rainfall intensity values at 5-minute intervals.

Ideally, individual storms would be identified directly from the measured data, and their observed 5-minute rainfall intensities would be used in the model. This, however, is time-consuming, as each storm must first be isolated within the large dataset. Three aspects of the current storm representation could be improved: rainfall accuracy of the storm in the intervals, the storm duration and the IDF curve. The storm duration of five hours is an assumption, chosen to approximate the run off time of the Quinuas catchment, as no measured value was available. For the IDF curve, the 24-hour rainfall total was used as a basis for extrapolation. These assumptions for the synthetic storm do not make the current one inaccurate, but indicate that there is room for greater precision through calibration and analysis of rainfall data.

For the spatial input data of the LISEM model, it is described in 8 how this can be improved to make the model more accurate. However, this is mainly focussed on making a regional landslide hazard model for the Azuay province. When researching specific, smaller scale locations for their risk on land slides (e.g. a single slope), it is necessary to obtain data with higher resolutions. Now, most data is obtained from the base maps which have a resolution of 30m, but a resolution of around 1m would be better for local landslide risk mapping. However, the feasibility of this is low, as this would mean having to perform new satellite data measurements with enormous data amounts.

Finally, the methods of LISEM could be further investigated to see if all formulas are suitable in our research area. What happens behind the scenes of the software is globally described in the LISEM manual, but some ambiguities remain. Examples of this are: how is rock size incorporated in the calculations? Why are clay, sand and gravel fractions required if density, cohesion and internal friction angle already define the relevant soil parameters? And to what extent does the cohesion and density of the bedrock influence the final results?

For the social part on this report, it shows that the situation surrounding the Loma Larga project is largely shaped by the unequal power relations between the government, Dundee Precious Metals and the local community. It is the local people who are most affected, yet they have the least influence. As was evident during the protests in September 2025, collective action is often their only means of being heard. However, this also highlights the region's lack of stable and inclusive governance.

Future research should focus on identifying more equitable ways for communities and indigenous groups to participate in decision-making processes from the beginning. This could involve learning from other Andean regions or countries that face comparable challenges regarding mining and resource utilisation.

Additionally, while this study primarily examined mining-related conflicts, further research is required to understand the impact of changing weather and water patterns on these same groups. Changing weather patterns could alter water availability, land use and livelihoods, thereby changing the dynamics of power and conflict in the Páramo. Combining social and environmental research would improve our understanding of how mining and changing weather patterns threaten water security and community well-being together. Addressing these challenges will require technical, environmental and social solutions all together.

In this context, the Loma Larga project illustrates how mining activities can intersect with environmental change to amplify risks to water systems. The project is expected to have a significant impact on local and regional hydrology. Further research is needed to better understand the long-term behaviour of tailings and mine drainage, particularly their influence on deeper groundwater layers within the highly connected páramo system. The current design of the Filtered Tailings Storage Facility (FTSF) raises major concerns regarding safety and sustainability. A redesign is required to minimize seepage and ensure long-term environmental protection. Similarly, the wastewater treatment plant (WWTP) should be optimized through the addition of nitrate removal and improved pH control to meet water quality standards in this fragile ecosystem.

In addition, the quality and chemical composition of mine drainage water require more detailed investigation. This could be achieved through laboratory testing and comparative case studies of similar high-sulfidation mining operations, to better predict contaminant behaviour under local hydrogeochemical conditions. Finally, future assessments should integrate more detailed meteorological and hydrological data to accurately evaluate long-term risks and support adaptive, environmentally responsible management of the Loma Larga project.

# A

# Remote sensing

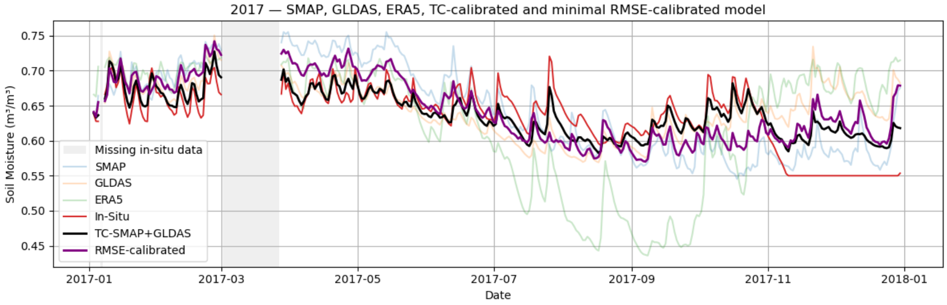

Figure A.1: Calibrated models vs. in-situ SM-data, 2017.

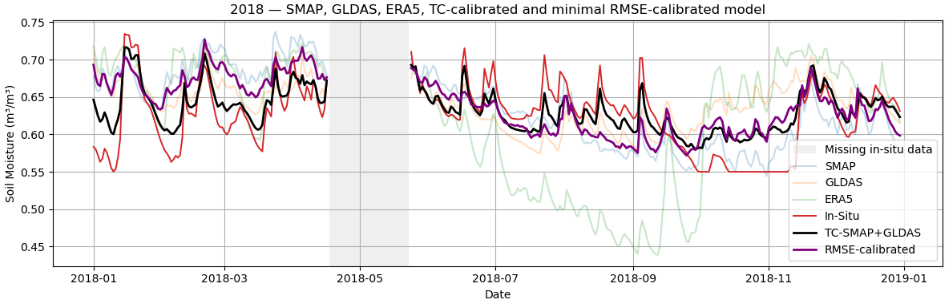

Figure A.2: Calibrated models vs. in-situ SM-data, 2018.

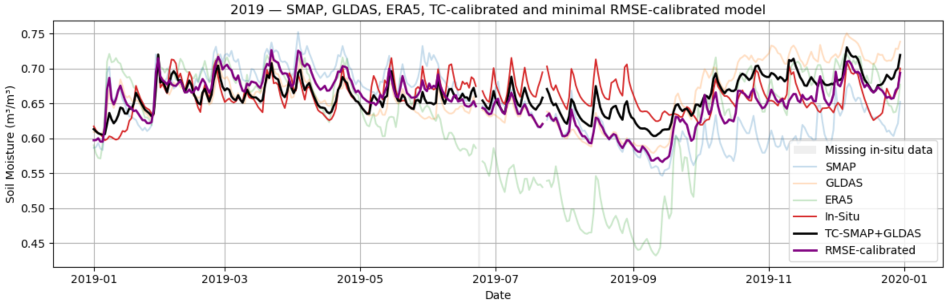

Figure A.3: Calibrated models vs. in-situ SM-data, 2019.

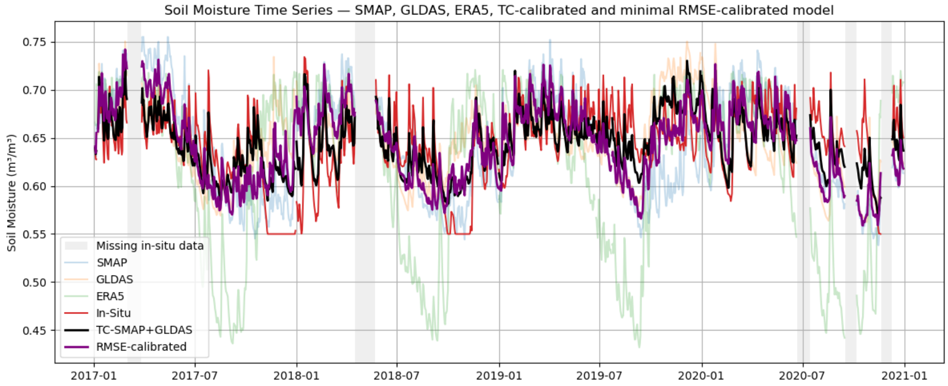

Figure A.4: Calibrated models vs. in-situ SM-data, all synced years.

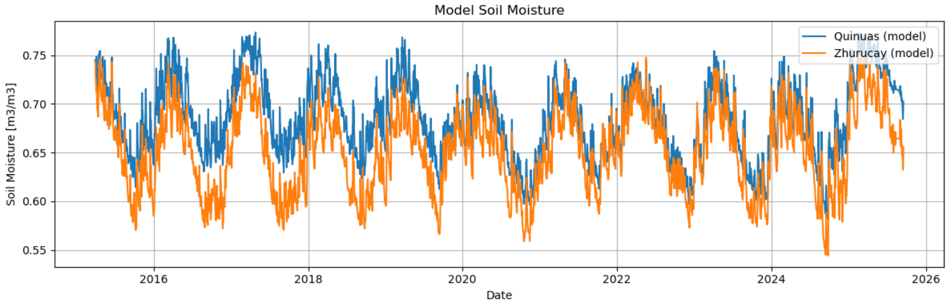

Figure A.5: RMSE-calibrated SM-model for Quinuas and Zhurucay.

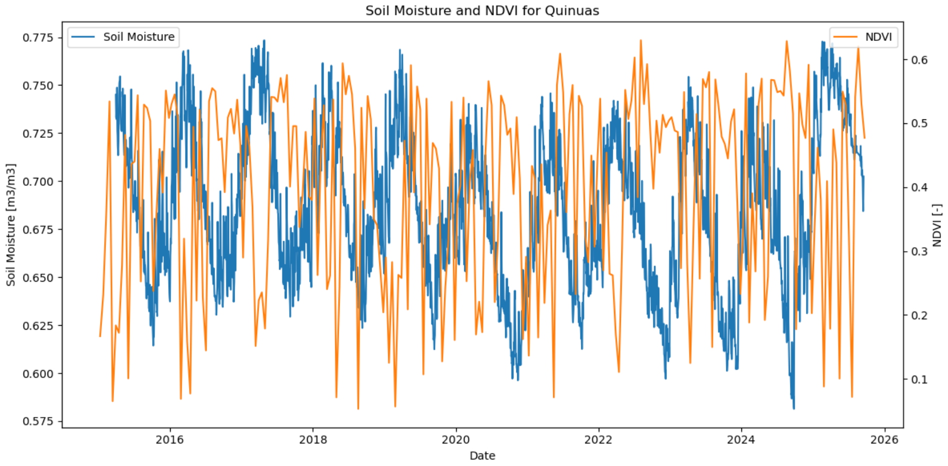

Figure A.6: RMSE-calibrated SM-model vs. NDVI, Quinuas.

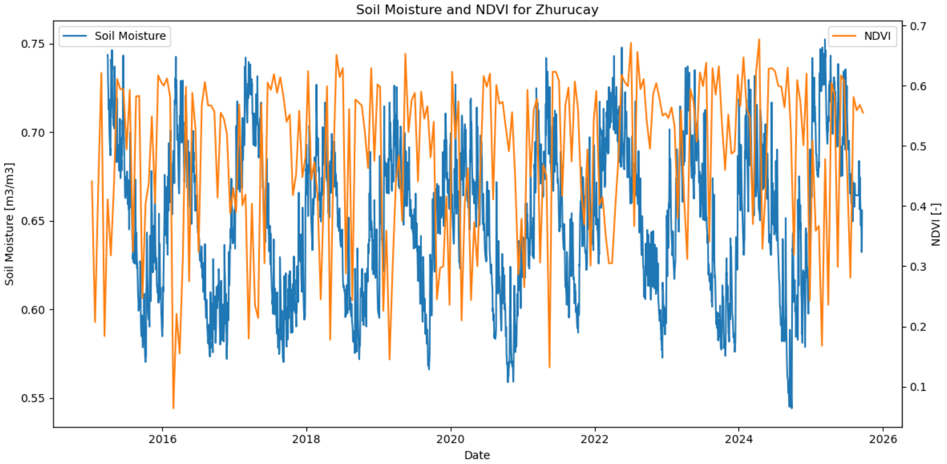

Figure A.7: RMSE-calibrated SM-model vs. NDVI, Zhurucay.

# B

# Trend analysis and forecasting

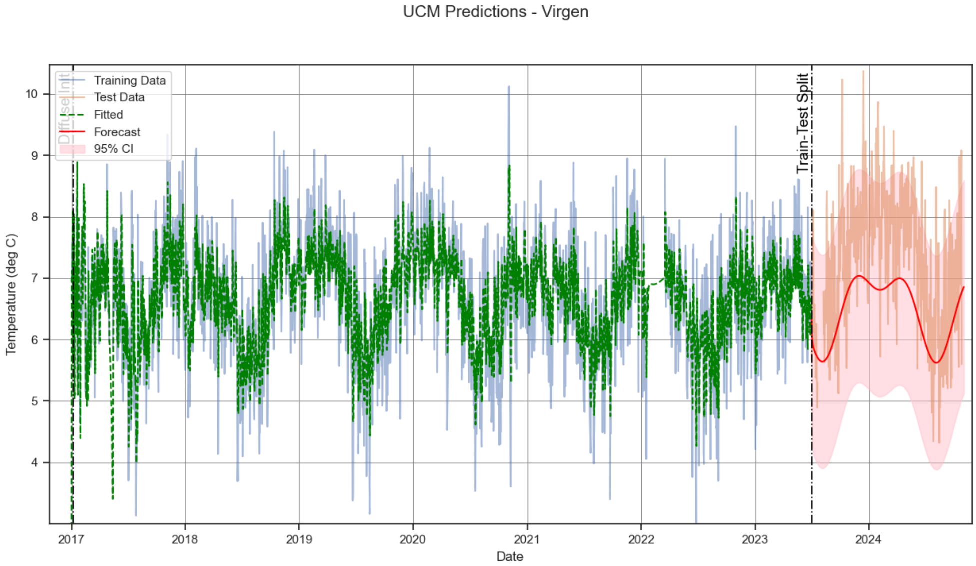

(a) UCM model fit and forecast on the temperature data from the Virgen station.

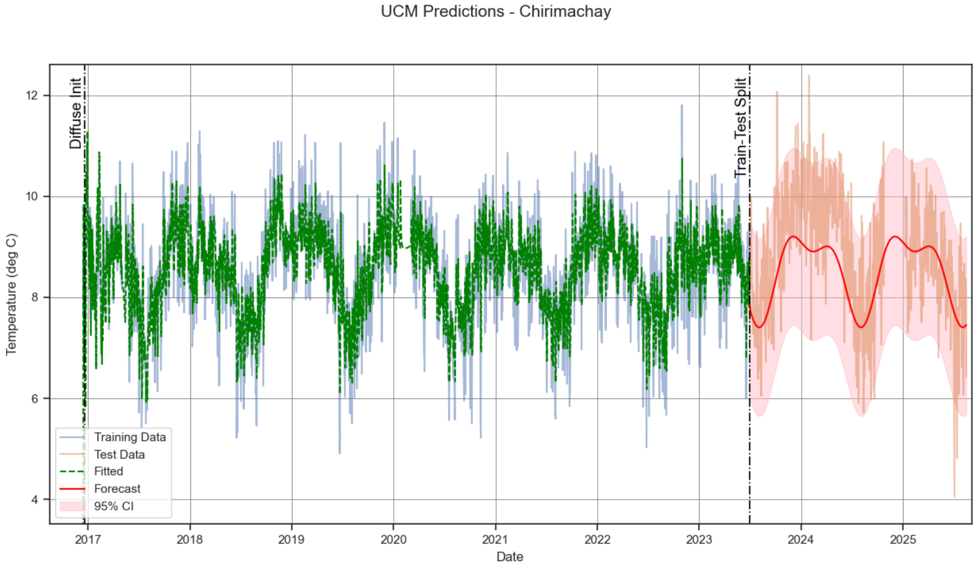

(b) UCM model fit and forecast on the temperature data from the Chirimachay station.

Figure B.1: UCM model fit and forecast for the Virgen and Chirimachay stations.

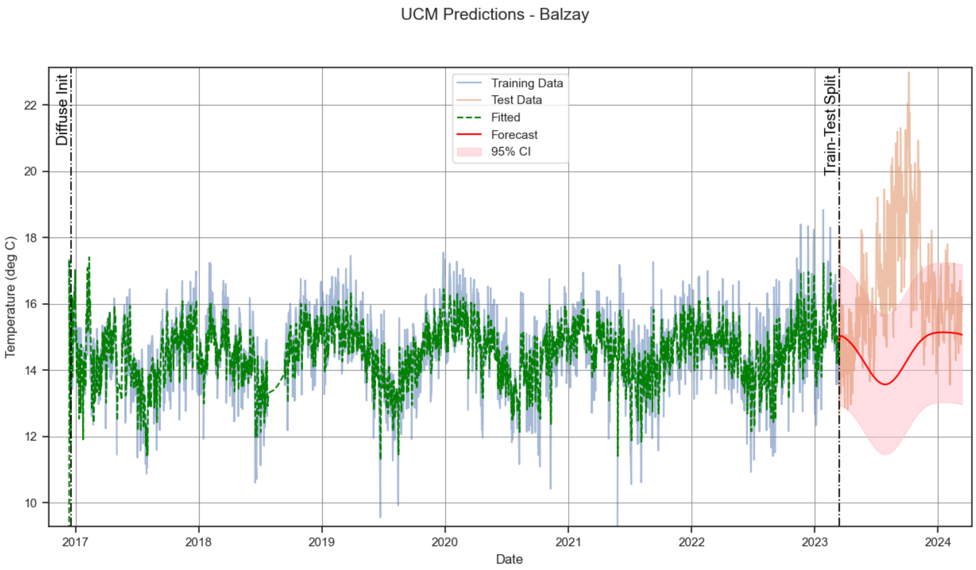

(a) UCM model fit and forecast on the temperature data from the Balzay station.

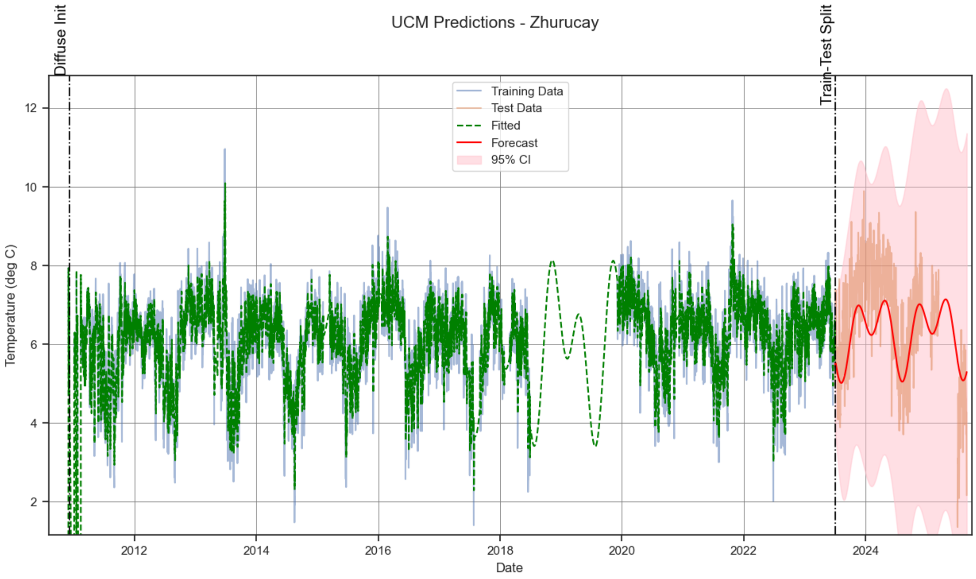

(b) UCM model fit and forecast on the temperature data from the Zhurucay station.

Figure B.2: UCM model fit and forecast for the Balzay and Zhurucay stations.

# C

# Synthetic storms

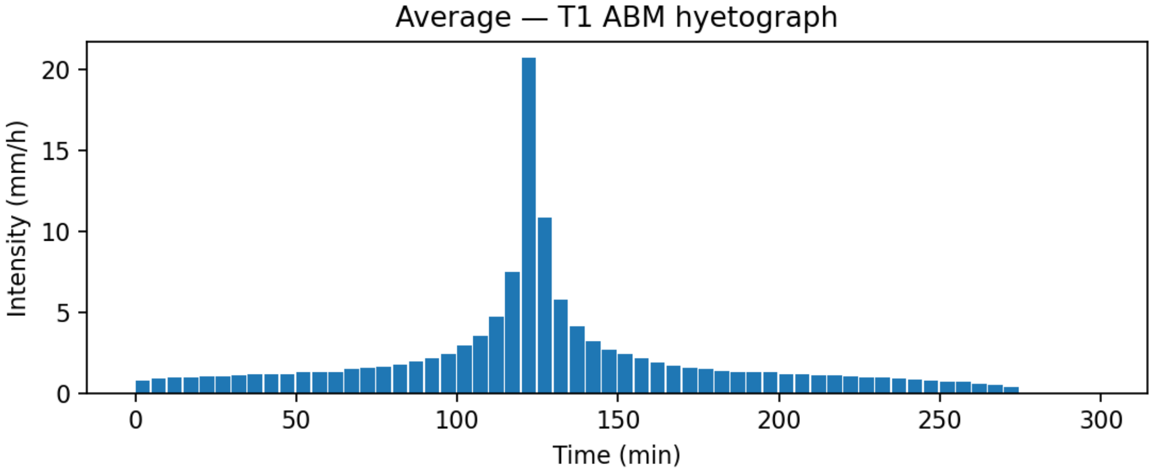

Figure C.1: Average storm with return period 1 year

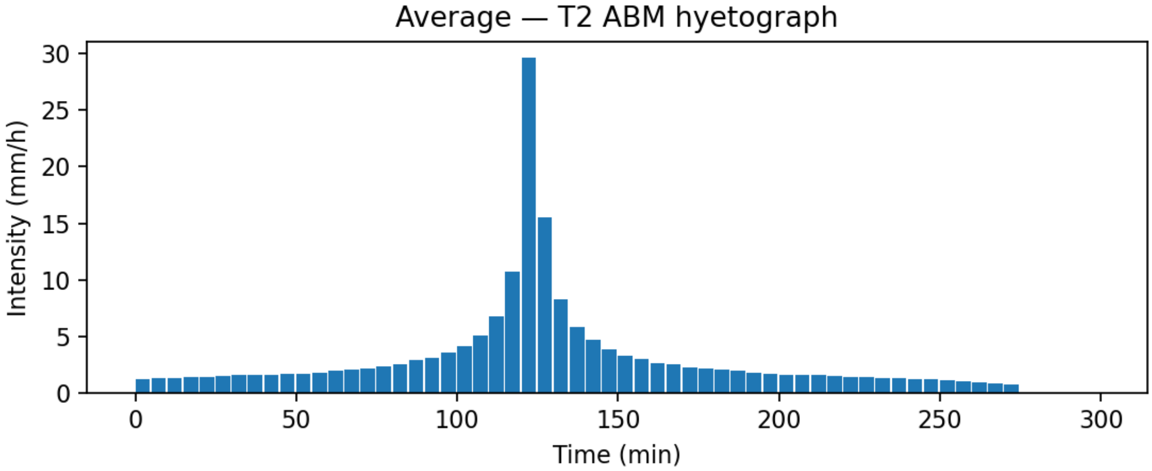

Figure C.2: Average storm with return period 2 years

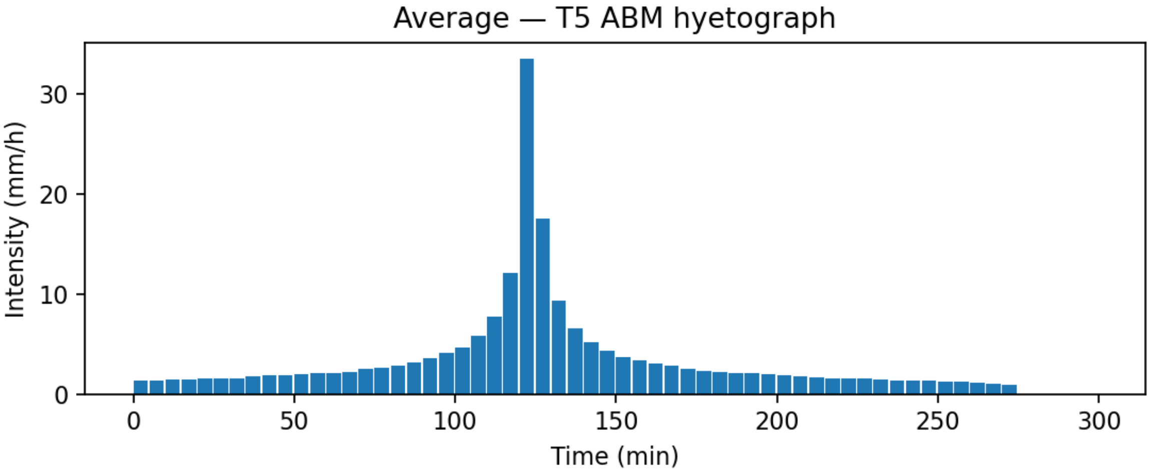

Figure C.3: Average storm with return period 5 years

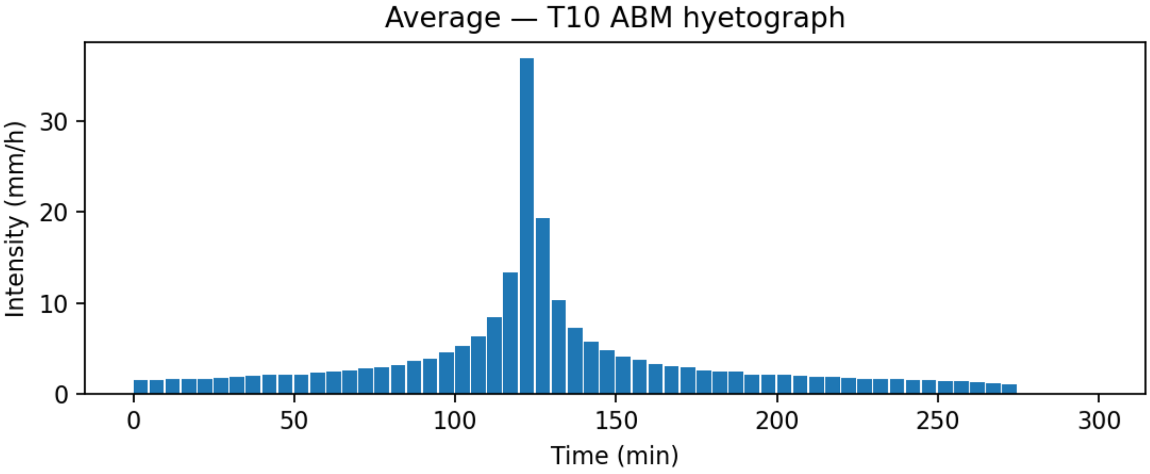

Figure C.4: Average storm with return period 10 years

# D

# Stakeholder tables

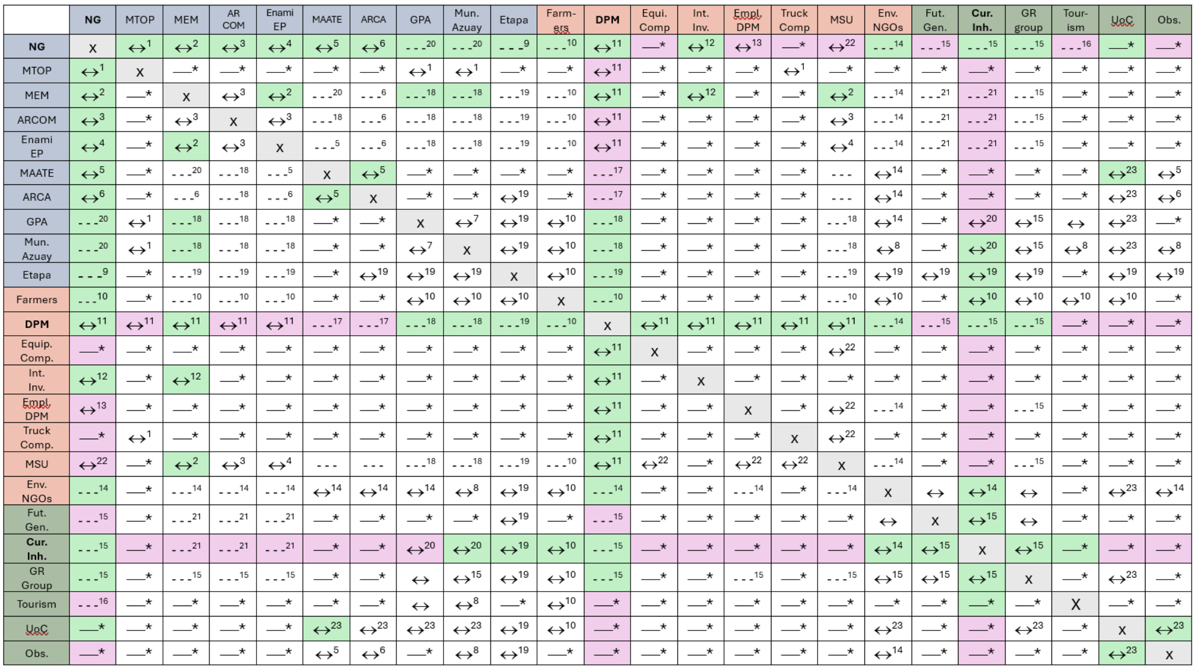

| | **NG** | MTOP | MEM | AR COM | Enami EP | MAATE | ARCA | GPA | Mun. Azuay | Etapa | Farm-ers | **DPM** | Equi. Comp | Int. Inv. | Empl. DPM | Truck Comp | MSU | Env. NGOs | Fut. Gen. | **Cur. Inh.** | GR group | Tour-ism | UoC | Obs. |
|---|---|---|---|---|---|---|---|---|---|---|---|---|---|---|---|---|---|---|---|---|---|---|---|---|
| **NG** | X | ↔[1] | ↔[2] | ↔[3] | ↔[4] | ↔[5] | ↔[6] | - - -[20] | - - -[20] | - - -[9] | - - -[10] | ↔[11] | —[*] | ↔[12] | ↔[13] | —[*] | ↔[22] | - - -[14] | - - -[15] | - - -[15] | - - -[15] | - - -[16] | —[*] | —[*] |
| MTOP | ↔[1] | X | —[*] | —[*] | —[*] | —[*] | —[*] | ↔[1] | ↔[1] | —[*] | —[*] | ↔[11] | —[*] | —[*] | —[*] | ↔[1] | —[*] | —[*] | —[*] | —[*] | —[*] | —[*] | —[*] | —[*] |
| MEM | ↔[2] | —[*] | X | ↔[3] | ↔[2] | - - -[20] | - - -[6] | - - -[18] | - - -[18] | - - -[19] | - - -[10] | ↔[11] | —[*] | ↔[12] | —[*] | —[*] | ↔[2] | - - -[14] | - - -[21] | - - -[21] | - - -[15] | —[*] | —[*] | —[*] |
| ARCOM | ↔[3] | —[*] | ↔[3] | X | ↔[3] | - - -[18] | - - -[6] | - - -[18] | - - -[18] | - - -[19] | - - -[10] | ↔[11] | —[*] | —[*] | —[*] | —[*] | ↔[3] | - - -[14] | - - -[21] | - - -[21] | - - -[15] | —[*] | —[*] | —[*] |
| Enami EP | ↔[4] | —[*] | ↔[2] | ↔[3] | X | - - -[5] | - - -[6] | - - -[18] | - - -[18] | - - -[19] | - - -[10] | ↔[11] | —[*] | —[*] | —[*] | —[*] | ↔[4] | - - -[14] | - - -[21] | - - -[21] | - - -[15] | —[*] | —[*] | —[*] |
| MAATE | ↔[5] | —[*] | - - -[20] | - - -[18] | - - -[5] | X | ↔[5] | —[*] | —[*] | —[*] | —[*] | - - -[17] | —[*] | —[*] | —[*] | —[*] | - - - | ↔[14] | —[*] | —[*] | —[*] | —[*] | ↔[23] | ↔[5] |
| ARCA | ↔[6] | —[*] | - - -[6] | - - -[18] | - - -[6] | ↔[5] | X | —[*] | —[*] | ↔[19] | —[*] | - - -[17] | —[*] | —[*] | —[*] | —[*] | - - - | ↔[14] | —[*] | —[*] | —[*] | —[*] | ↔[23] | ↔[6] |
| GPA | - - -[20] | ↔[1] | - - -[18] | - - -[18] | - - -[18] | —[*] | —[*] | X | ↔[7] | ↔[19] | ↔[10] | - - -[18] | —[*] | —[*] | —[*] | —[*] | - - -[18] | ↔[14] | —[*] | ↔[20] | ↔[15] | ↔ | ↔[23] | —[*] |
| Mun. Azuay | - - -[20] | ↔[1] | - - -[18] | - - -[18] | - - -[18] | —[*] | —[*] | ↔[7] | X | ↔[19] | ↔[10] | - - -[18] | —[*] | —[*] | —[*] | —[*] | - - -[18] | ↔[8] | —[*] | ↔[20] | ↔[15] | ↔[8] | ↔[23] | ↔[8] |
| Etapa | - - -[9] | —[*] | - - -[19] | - - -[19] | - - -[19] | —[*] | ↔[19] | ↔[19] | ↔[19] | X | ↔[10] | - - -[19] | —[*] | —[*] | —[*] | —[*] | - - -[19] | ↔[19] | ↔[19] | ↔[19] | ↔[19] | —[*] | ↔[19] | ↔[19] |
| Farmers | - - -[10] | —[*] | - - -[10] | - - -[10] | - - -[10] | —[*] | —[*] | ↔[10] | ↔[10] | ↔[10] | X | - - -[10] | —[*] | —[*] | —[*] | —[*] | - - -[10] | ↔[10] | —[*] | ↔[10] | ↔[10] | ↔[10] | ↔[10] | —[*] |
| **DPM** | ↔[11] | ↔[11] | ↔[11] | ↔[11] | ↔[11] | - - -[17] | - - -[17] | - - -[18] | - - -[18] | - - -[19] | - - -[10] | X | ↔[11] | ↔[11] | ↔[11] | ↔[11] | ↔[11] | - - -[14] | - - -[15] | - - -[15] | - - -[15] | —[*] | —[*] | —[*] |
| Equip. Comp. | —[*] | —[*] | —[*] | —[*] | —[*] | —[*] | —[*] | —[*] | —[*] | —[*] | —[*] | ↔[11] | X | —[*] | —[*] | —[*] | ↔[22] | —[*] | —[*] | —[*] | —[*] | —[*] | —[*] | —[*] |
| Int. Inv. | ↔[12] | —[*] | ↔[12] | —[*] | —[*] | —[*] | —[*] | —[*] | —[*] | —[*] | —[*] | ↔[11] | —[*] | X | —[*] | —[*] | —[*] | —[*] | —[*] | —[*] | —[*] | —[*] | —[*] | —[*] |
| Empl. DPM | ↔[13] | —[*] | —[*] | —[*] | —[*] | —[*] | —[*] | —[*] | —[*] | —[*] | —[*] | ↔[11] | —[*] | —[*] | X | —[*] | ↔[22] | - - -[14] | —[*] | —[*] | - - -[15] | —[*] | —[*] | —[*] |
| Truck Comp. | —[*] | ↔[1] | —[*] | —[*] | —[*] | —[*] | —[*] | —[*] | —[*] | —[*] | —[*] | ↔[11] | —[*] | —[*] | —[*] | X | ↔[22] | —[*] | —[*] | —[*] | —[*] | —[*] | —[*] | —[*] |
| MSU | ↔[22] | —[*] | ↔[2] | ↔[3] | ↔[4] | - - - | - - - | - - -[18] | - - -[18] | - - -[19] | - - -[10] | ↔[11] | ↔[22] | —[*] | ↔[22] | ↔[22] | X | - - -[14] | —[*] | —[*] | - - -[15] | —[*] | —[*] | —[*] |
| Env. NGOs | - - -[14] | —[*] | - - -[14] | - - -[14] | - - -[14] | ↔[14] | ↔[14] | ↔[14] | ↔[8] | ↔[19] | ↔[10] | - - -[14] | —[*] | —[*] | - - -[14] | —[*] | - - -[14] | X | ↔ | ↔[14] | ↔ | —[*] | ↔[23] | ↔[14] |
| Fut. Gen. | - - -[15] | —[*] | - - -[21] | - - -[21] | - - -[21] | —[*] | —[*] | —[*] | —[*] | ↔[19] | —[*] | - - -[15] | —[*] | —[*] | —[*] | —[*] | —[*] | ↔ | X | ↔[15] | ↔ | —[*] | —[*] | —[*] |
| **Cur. Inh.** | - - -[15] | —[*] | - - -[21] | - - -[21] | - - -[21] | —[*] | —[*] | ↔[20] | ↔[20] | ↔[19] | ↔[10] | - - -[15] | —[*] | —[*] | —[*] | —[*] | —[*] | ↔[14] | ↔[15] | X | ↔[15] | —[*] | —[*] | —[*] |
| GR Group | - - -[15] | —[*] | - - -[15] | - - -[15] | - - -[15] | —[*] | —[*] | ↔ | ↔[15] | ↔[19] | ↔[10] | - - -[15] | —[*] | —[*] | - - -[15] | —[*] | - - -[15] | ↔[15] | ↔[15] | ↔[15] | X | —[*] | ↔[23] | —[*] |
| Tourism | - - -[16] | —[*] | —[*] | —[*] | —[*] | —[*] | —[*] | ↔ | ↔[8] | —[*] | ↔[10] | —[*] | —[*] | —[*] | —[*] | —[*] | —[*] | —[*] | —[*] | —[*] | —[*] | X | —[*] | —[*] |
| UoC | —[*] | —[*] | —[*] | —[*] | —[*] | ↔[23] | ↔[23] | ↔[23] | ↔[23] | ↔[19] | ↔[10] | —[*] | —[*] | —[*] | —[*] | —[*] | —[*] | ↔[23] | —[*] | —[*] | ↔[23] | —[*] | X | ↔[23] |
| Obs. | —[*] | —[*] | —[*] | —[*] | —[*] | ↔[5] | ↔[6] | —[*] | ↔[8] | ↔[19] | —[*] | —[*] | —[*] | —[*] | —[*] | —[*] | —[*] | ↔[14] | —[*] | —[*] | —[*] | —[*] | ↔[23] | X |

Figure D.1: Table of stakeholder conflicts (Author’s work, 2025)

| | **Legend** |
|---|---|
| 🟦 | Public stakeholders |
| 🟧 | Private stakeholders |
| 🟩 | Civil stakeholders |
| 🟪 | Three most relevant stakeholders in conflict |
| 🟩 | Drawn lines in conflicting diagram |

Figure D.2: Table of stakeholder conflicts legend (Author’s work, 2025)

Sources used to determine conflicts:
[*] No direct connection [1] Ministerio de Infraestructura y Transporte, n.d.
[2] Ministerio del Ambiente, n.d.
[3] Agencia de Regulación y Control Minero, n.d.
[4] ENAMI EP, n.d.
[5] Ministry of the Environment and Transition, n.d.
[6] Agencia de Regulación y Control del Agua, n.d.